Charles University

Faculty of Science

Study program: Modelling of Chemical Properties on Nano- and Biostructures

M.Sc. Mengting Jin

Theoretical Investigation of the Zeolite Hydrolysis under Realistic Conditions

Ph.D. Dissertation

Supervisor: RNDr. Lukáš Grajciar, Ph.D.

Advisors: Prof. RNDr. Petr Nachtigall, Ph.D. and Christopher James Heard, Ph.D.

Prague, 2022

Univerzita Karlova

Přírodovědecká fakulta

Studijní program: Modelování chemických vlastností nano- a biostruktur

M.Sc. Mengting Jin

Teoretické studium hydrolýzy zeolitů za realistických podmínek

Disertační práce

Školitel: RNDr. Lukáš Grajciar, Ph.D.

Konzultanti: Prof. RNDr. Petr Nachtigall, Ph.D. a Christopher James Heard, Ph.D.

Praha, 2022

Declaration of Authorship

I, Mengting Jin, declare that this dissertation titled, "**Theoretical Investigation of the Zeolite Hydrolysis under Realistic Conditions**" and the work presented in it is my own. All the literature is properly cited, and I have not been yet awarded any other academic degree or diploma for this thesis or its substantial part.

Signed:
Date:

Prohlášení:

Prohlašuji, že jsem závěrečnou práci zpracoval samostatně a že jsem uvedl všechny použité informační zdroje a literaturu. Tato práce ani její podstatná část nebyla předložena k získání jiného nebo stejného akademického titulu.

V Praze,

Podpis:

Acknowledgements

My Ph.D. study is nearing the end. I have a fulfilling and unforgettable time at Charles University. Studying abroad needs to overcome many difficulties, *e.g.*, language barrier, eating habits, cultural differences *etc.*, I was lucky to have many people guide me, help me, and inspire me, they made my scientific research work and life went more smoothly. There are many people I'd like to thank.

First of all, I'd like to thank my supervisor Dr. Lukáš Grajciar, he gave patient guidance throughout the work of this dissertation. I am very grateful to his patient guidance and education. I also want to thank my advisors prof. Petr Nachtigall and Dr. Christopher James Heard. During my Ph.D study, I had countless discussion meetings with them, and they continued to give me guidance and suggestions, so that I would not be so confused when facing research topics. They knew how to state a problem clearly and serious about scientific research. The way they deal with people and things have a deep influence on me. Under the guidance of my supervisor and advisors, I learned to face problems independently, learned to discuss problems with others, learned to express ideas more concisely and clearly, *etc.* These will have a profound impact on my future life.

Thanks to all members of our research group, I have a very fulfilling life in this group, I would like to thank the seniors Dr. Andreas Erlebach, Dr. Junjie He for their guidance and help. I also want to express my gratitude to Chen Lei, Mingxiu Liu, Dianwei Hou, Shuo Li, and other younger classmates who have communicated with me about their study and life.

Thank the faculty of science at Charles University provides a platform for me to broaden my experience and mind.

Finally, I'd like to thank all my family members. Especially my husband Wenzhen Yang and my beloved daughter Lingxi Yang, I am very grateful for all they have done for me. Family is my spiritual support. I can't finish this dissertation without their support and encouragement.

Mengting Jin

In Prague

June 2022

I dedicate this dissertation to

my husband, Wenzhen Yang

my beloved daughter, Lingxi Yang

for their love and unconditional support.

Contents

List of the Abbreviations

DFT — Density Functional Theory

DFT-D — Dispersion−corrected Density Functional Theory

SBU — Secondary Building Units

D4R — Double-4-Ring

D6R — Double-6-Ring

OSDA — Organic Structure Directing Agents

IZA — International Zeolite Association

FCC — Fluid Catalytic Cracking

HLW — Hot Liquid Water

ADOR — Assembly-Disassembly-Organization-Reassembly

3D — Three-Dimensional

2D — Two-Dimensional

UC — Unit Cell

BAS — Brønsted Acid Sites

LAS — Lewis Acid Sites

Al(Td) — Tetrahedral Aluminum

Al(Oh) — Octahedral Aluminum

PXRD — Powder X-ray Diffraction

XAS — X-ray Absorption Spectroscopy

MAS NMR — Magic Angle Spinning solid-state Nuclear Magnetic Resonance

SEM — Scanning Electron Microscopy

IR — Infrared Spectroscopies

Exc[ρ] — Exchange-correlation Functional

LDA — Local Density Approximation

GGA — Generalized Gradient Approximation

MD — Molecular Dynamics

AIMD — *Ab Initio* Molecular Dynamics

UHV — Ultra-High Vacuum

BOMD — Born-Oppenheimer Molecular Dynamics

PES — Potential Energy Surface

CI-NEB — Climbing Image Nudged Elastic Band

SG — Slow Growth

TI — Thermodynamic Integration

VASP — Vienna *Ab initio* Simulation Package

PAW — Projector-Augmented-Wave

PBE — Perdrew–Burke–Ernzerhof

CV — Collective Variable

RT — Room Temperature

O_f — Oxygen atom in the framework

O_w — Oxygen atom in the water

H_w — Hydrogen atom in the water

Q^4 — Pristine tetrahedral zeolite framework

Q^3 — First step hydrolysis product, one framework T-O-T bond is broken

Q^2 — Second step hydrolysis product, two framework T-O-T bonds are broken

Q^1 — Third step hydrolysis product, three framework T-O-T bonds are broken

Q^0 — Fourth step hydrolysis product, four framework T-O-T bonds are broken

Abstract

Zeolites are one of the most widely used and one of the most industrially important materials. They are utilized in a variety of commercial applications, particularly in heterogeneous catalysis, adsorption/separations applications and as ion exchangers. Zeolites are stable when exposed to water or water vapor at ambient conditions and exhibit high thermal stability. However, zeolites can be partially or even fully hydrolyzed under certain conditions. This hydrolytic instability of zeolites can be considered both a major problem in some applications and a useful means to tune catalyst properties in the others. However, the thorough studies of the hydrolytic mechanisms under realistic conditions (high water loading, alkaline conditions, high heteroatom concentrations, *etc.*) and employing realistic models (dynamical simulation of *ab initio* accuracy) is mostly lacking.

This dissertation uses the *ab initio* calculations to systematically study the hydrolysis mechanism of zeolites under realistic conditions, including: (1) hydrolysis mechanism of germanosilicate zeolite UTL, (2) hydrolysis of siliceous zeolite CHA under alkaline conditions, and (3) identification of the nature of framework-associated Al(Oh) species in aluminosilicate zeolite CHA under wet conditions. The main results obtained are as follows:

(1) Both the water loading and the germanium content play a very important role in the disassembly process of ADORable zeolites[1-6]. Different water and Ge contents will cause the degermanation to proceed according to completely different mechanisms. The increase of Ge content can both lower the reaction barriers and can lead to more favorable reaction energies both in the low and the high water loading conditions. In particular, the clustering of germanium in the S4R units has been shown to destabilize the framework immensely. A common feature of the newly discovered mechanisms is the cooperativity either with respect to cooperation of waters in the proton shuttling or with respect to increased local flexibility and reactivity of the D4R units filled with germanium. We thus obtain general principles for the selective hydrolysis of germanosilicates, supported by full mechanistic understanding. This fundamental research helps in directing further efforts towards synthesis of new zeolites from judiciously chosen germanosilicates.

(2) The NaOH enhances the rate of zeolite hydrolysis in each step by a significant amount as compared to hydrolysis in neutral water. The water and NaOH concentration play an important role for the kinetics and thermodynamics of the zeolite hydrolysis process. We found that NaOH can act either as a reactant or as a catalyst. The former mechanism is

characterized by very low energy barriers but it leads to large NaOH consumption. In the latter mechanism, NaOH can be regenerated *in situ* by consuming an additional water molecule, allowing for desilication without consumption of NaOH and it becomes competitive under microsolvation conditions. Besides accelerating the catalytic desilication, we also discovered that the microsolvation drives spontaneous defect formation. We provide an explanation for the enhanced desilication of zeolites under mild, alkaline conditions, and evidence for the inside-out mode of zeolite hydrolysis.

(3) The structural characteristics and the details of the mechanism that leads to formation of framework-associated octahedral Al(Oh) species, *i.e.*, of the octahedral framework-associated Lewis acid site (LAS), were discovered. The framework-associated Al(Oh) was found to be thermodynamically stable and kinetically connected to Brønsted acid site (BAS) already at the room temperature. It can be formed (at least in CHA zeolite) under the following conditions: (i) At least three BAS sites must be near to allow transfer and fixation of protons around the to-be-formed octahedral aluminum. (ii) Al(Oh) species is formed from one of the Al atoms of the Al-O-Si-O-Al pair, where Al atoms are separated by a single framework silicon atom. (iii) The presence of water molecules in the channel system is required to create and stabilize the Al(Oh), and realistic dynamical description of water solvation is thus of great importance. This work resolves the question about the nature and reversibility of framework-associated Al(Oh) in CHA zeolite and brings additional evidence that the framework of acidic zeolites becomes labile under wet conditions[7].

Abstrakt

Zeolity jsou jedním z nejpoužívanějších a průmyslově nejdůležitějších materiálů. Používají se v různých komerčních aplikacích, zejména v heterogenní katalýze, adsorpčních/separačních aplikacích a jako iontoměniče. Zeolity jsou stabilní při vystavení kapalné vodě nebo vodní páře za běžných podmínek a vykazují vysokou tepelnou stabilitu. Zeolity však mohou být za určitých podmínek částečně nebo dokonce zcela hydrolyzovány. Tato hydrolytická nestabilita zeolitů může být považována v některých aplikacích za zásadní problém, zatímco v jiných aplikacích za užitečný prostředek pro optimalizaci vlastností katalyzátoru. Důkladné studie hydrolytických mechanismů za realistických podmínek (vysoké nasycení zeolitů vodou, alkalické pH, vysoké koncentrace heteroatomů, *atd.*) a za použití realistických modelů (dynamické simulace s přesností *ab initio* metod) však většinou chybí.

Tato disertační práce využívá *ab initio* výpočty k systematickému studiu mechanismu hydrolýzy zeolitů za reálných podmínek, včetně: (1) mechanismu hydrolýzy germanosilikátového zeolitu UTL, (2) hydrolýzy křemičitého zeolitu CHA za alkalických podmínek a (3) identifikace povahy oktaedrálně koordinovaného typu hliníku spojeného se zeolitickou mříží, Al(Oh), v aluminosilikátovém zeolitu CHA v přítomnosti vody v zeolitické mříži. Hlavní výsledky získané v této praci jsou následující:

(1) Jak míra nasycení zeolitcké mříže vodou, tak obsah germánia v mříži hrají velmi důležitou roli v procesu částečné hydrolýzy ADORable zeolitů. Rozdílný obsah vody a germánia způsobí, že degermánace bude probíhat zcela odlišnými mechanismy. Zvýšení obsahu germánia může nejenom snížit reakční bariéry, ale také může vést k příznivějším reakčním energiím, a to jak v podmínkách nízkého, tak i vysokého objemu vody v zeolitické mříži. Ukázalo se zejména, že shlukování germánia v jednotkách S4R nesmírně destabilizuje zeolitickou mříž. Společným rysem nově objevených mechanismů je kooperativita, buď s ohledem na kooperaci vod při protonovém transferu, nebo s ohledem na zvýšenou lokální flexibilitu a reaktivitu jednotek D4R, ve kterých je shlukováno germánium. Byli jsme tak schopni získat obecné principy pro selektivní hydrolýzu germanosilikátů, podpořené úplným mechanistickým pochopením. Tento základní výzkum pomůže nasměrovat další úsilí v syntéze nových zeolitů z pěčlivě vybraných germanosilikátů.

(2) Hydroxid sodný, NaOH, zásadně zvyšuje rychlost hydrolýzy zeolitu ve srovnání s hydrolýzou v neutrálním vodním roztoku. Ukazuje se, že koncentrace vody a NaOH v

zeolitické mříži zásadně ovlivňují kinetiku a termodynamiku procesu hydrolýzy zeolitu. Zjistili jsme také, že NaOH může působit buď jako reaktant nebo jako katalyzátor hydrolýzy. V případě role NaOH jako reaktantu se mechanismus hydrolýzy vyznačuje velmi nízkou energetickou bariérou, ale vede k velké spotřebě NaOH. V případě role NaOH jako katalyzátoru může být NaOH regenerován *in situ* spotřebováním molekuly vody, což umožňuje desilikaci, čili hydrolýzu křemíku, bez spotřeby NaOH. Navíc aktivační bariéry pro tento katalytický mechanizmus se snížují za podmínek mikrosolvatace vodou uvnitř zeolitické mříže. Kromě urychlení katalytické desilikace jsme také zjistili, že mikrosolvatace podporuje spontánní tvorbu defektů. Naše práce tak poskytuje vysvětlení zvýšené desilikace zeolitů za mírných, alkalických podmínek a předkládá důkazy o hydrolýze zeolitů, která začíná uvnitř zeolitické mříže a postupuje zevnitř zeolitu směrem k jeho povrchu.

(3) Byly objeveny strukturní charakteristiky a podrobnosti mechanismu, který vede k vytvoření oktaedrálně koordinovaného hliníku, Al(Oh), asociovaného se zeolitickou mříží, tj. k vytvoření oktaedrálního Lewisovského kyselého místa (LAS). Bylo zjištěno, že Al(Oh) asociovaný se zeolitickou mříží je termodynamicky stabilní a proces jeho tvorby z Brønstedovho kyselého místa (BAS) je kineticky povolený již při pokojové teplotě. Al(Oh) struktura může být vytvořena (alespoň v zeolitu CHA) za následujících podmínek: (i) Alespoň tři BAS místa musí být v blízké vzdálenosti, aby se umožnil přenos a fixace protonů kolem oktaedrického hliníku, který se má vytvořit. (ii) Al(Oh) struktura se tvoří z jednoho z atomů hliníku v strukturním motivu Al-O-Si-O-Al, ve kterém jsou atomy hliníku odděleny jenom jedním atomem křemíku. (iii) Pro vytvoření a stabilizaci Al(Oh) je také vyžadována přítomnost molekul vody v kanálovém systému, a proto je velmi důležitý realistický dynamický popis solvatace vody. Práce v tomto projektu tedy řeší otázku povahy a reverzibility oktaedrálně koordinovaného hliníku asociovaného se zeolitickou mříží v CHA zeolitu a přináší další důkazy, že mříž kyselých zeolitů se za přítomnosti vody v kanálovém systému stává labilní.

1. Introduction

1.1 Zeolites

Zeolites[8-10] are crystalline microporous materials. The zeolite framework is composed of corner-sharing TO_4 tetrahedra (T is typically Si or Al) forming crystals with three-dimensional network structures, possessing cavities and channels with dimensions typically below 1 nm, as shown in Figure 1.1. The general chemical formula of classical aluminosilicate zeolite is: $(M)_{x/n}$ $[(AlO_2)_x$ $(SiO_2)_y]$ $\bullet mH_2O$, M stands for metal charge-compensating cation (usually K^+、Na^+ and Ca^{2+}、Ba^{2+} *et al.*), *n* stands for metal ion valence, *x* stands for the number of Al atoms, *y* stands for number of Si atoms, and *m* represents the number of waters in zeolite channel per unit of chemical formula. The extra-framework cations are used to balance the excess negative charge of the tetrahedron framework due to aluminum substitution for silicon and they represent important acid catalytic sites (both, Brønsted and Lewis type).

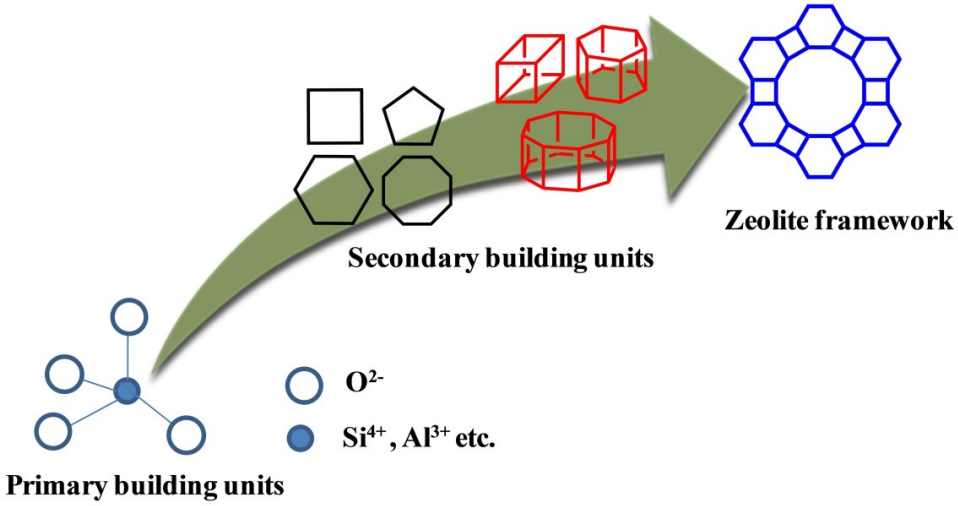

Figure 1.1: The schematic diagram of zeolite composition, from basic building unit to 3D zeolite framework. Reproduced with permission[10]. Copyright 2020, John Wiley and Sons.

There are more than 250 different zeolite frameworks synthetized as listed by International Zeolite Association (IZA)[11]. Each zeolite framework structure is named with a code consisting of three capital letters[12], these 3-letter code usually derives from the name of the zeolite or 'type material'. *e.g.*, the code FAU is the natural mineral faujasite. The 3-letter code

only describes and defines the framework type and does not determine the zeolite composition, T site distribution of heteroatoms, cell dimensions or symmetry.

The T site of TO_4 can be isomorphically substituted by other trivalent and tetravalent elements, *e.g.*, by Ge[5, 13], Ti[14-16], B[17-19], P[20-21], Sn[22-23] *etc.* The different forms and states of heteroatoms on the surface of zeolites directly affect the acidity, pore structure and catalytic performance of the zeolites. The heteroatom not only enriches the types of constituent elements of the zeolite framework, but also gives it unique acid catalysis and catalytic oxidation performance. In addition, the heteroatom can stabilize specific secondary building units (SBU) that are difficult to form in aluminosilicate zeolites. For instance, introducing Ge atoms into synthesis gels can direct the zeolite crystallization towards zeolites containing the double-4-ring (D4R) SBU units, because Ge atoms have a synergetic structure-directing functionality in cooperation with organic structure-directing agents (OSDA) and the flexibility of Ge-O-Ge/Si-O-Ge bond angles reduces the strain in the SUB, making it energetically stable to form small-rings[24]. D4R unit is thus found in almost all germanosilicates (*e.g.*, UTL, UOV, IWW, ITH).

Zeolites has been widely used as an important material in many fields due to their flexibility and adaptability[25-28], due to the diversity and tunability of their pore structure, range of constituent elements and active center types. Zeolites have shown excellent performance in many important chemical processes, particularly in heterogeneous catalysis (used in petroleum processing, production of fine chemicals, *etc.*), adsorption/separations (used in industrial and environmental separation and purification processes, field of drying, *etc.*), and ion exchange (widely used in detergent industry, waste treatment, *etc.*). For example, one of the most important application of zeolite catalysts is in fluid catalytic cracking (FCC) reaction process[29-30], converting high boiling point, high molecular weight hydrocarbons in petroleum into more valuable gasoline, light olefin gas and other products. The particularly beneficial zeolite properties are large surface areas, variable pore size distributions, crystallinity, and thermal stability; these structural properties make the zeolites not only excellent adsorbents but also effective catalysts. In addition, the ability of zeolites to reversibly ion-exchange further extends their adsorption and catalytic tunability.

1.2 Zeolite hydrolytic (in)stability

Zeolites are stable when exposed to water or water vapor and show high thermal stability under ambient conditions. However, the crystalline framework of zeolites can be partially or

even fully hydrolyzed under certain conditions such as high-water vapor pressure, high temperature, acidic or basic condition and so on. The possible modes of water-zeolite interaction are summarized in the Figure 1.2[31]. The non-reactive interaction means that water molecules are physical adsorbed in the zeolite and do not react with the framework by breaking any bonds. This non-reactive water adsorption is strongly affected by factors such as the Si/Al ratio, water partial pressure, type of heteroatom, concentration of defects *etc*. The reactive interaction of water with zeolites leads to the chemical reaction resulting in initial hydrolysis of the isolated T-O-T bridges, followed by complete removal of T species from zeolite framework which can further lead to formation of mesopores in the framework. Further massive hydrolysis can completely change the zeolite from crystalline to amorphous material. The hydrolysis path and type of the preferred demetallation (*e.g.*, desilication *vs.* dealumination) again strongly depends on the hydrolysis conditions, *e.g.*, whether the zeolite framework is steamed, or exposed to pressurized hot liquid water (HLW), what is the pH, or what heteroatom type is present in the framework.

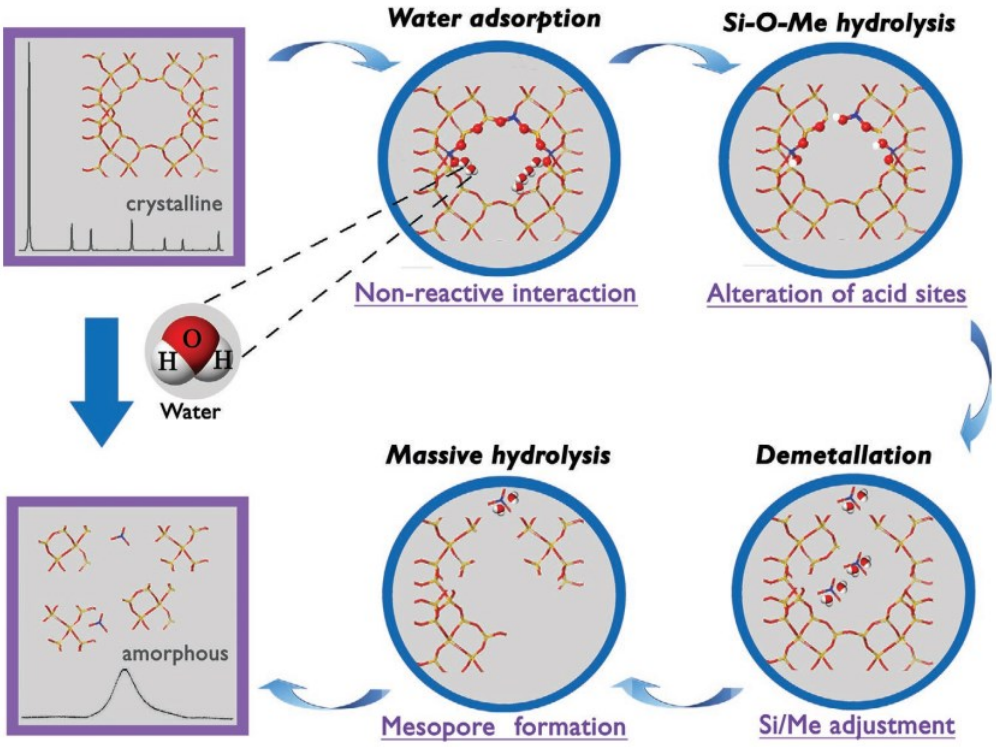

Figure 1.2: Schematic diagram of zeolite hydrolysis leading to framework degradation starting from nonreactive water adsorption up to the amorphization. Reproduced with permission [31]. Copyright 2020, John Wiley and Sons.

Zeolite hydrolysis can be considered as a major problem in some applications which may cause the crystalline structure decomposition and catalyst deactivation. Industrial processes often require harsh conditions, for instance, biomass conversion is carried out under HLW conditions[32-33]and crude oil processing (FCC) also includes steaming conditions[29-30]. Hence, controlling and understanding zeolite hydrolysis is essential to control and understand zeolite stability in the typical industrial set-up. However, in certain cases, the (partial) zeolite hydrolysis can have a positive impact such as in: i) opening new routes for preparation of new zeolite frameworks using ADOR (Assembly-Disassembly-Organization-Reassembly) strategy (see below)[1-6], or ii) enabling tuning the zeolite pore size by partial hydrolysis forming a secondary mesoporosity that can improve the diffusion limitations of microporous zeolites. In addition, understanding zeolite hydrolysis is also essential for understanding the inverse process of the zeolite synthesis. Lastly, controlled demetallation (mostly desilication or dealumination) is commonly used for fine-tuning the zeolite properties (acidity, accessibility, *etc.*) for particular catalytic and adsorption applications [26, 34-36].

The ADOR process is a very promising method for synthesis of new zeolites making the process of synthesizing new zeolites controllable and predictable. The main idea of the ADOR method is to introduce the unstable Ge-O bonds into zeolite frameworks. These Ge-O bonds can be easily hydrolyzed in the presence of water, even at ambient conditions. Thus, the germanosilicate zeolites are the most common parent materials used for ADOR, in particular those germanosilicates containing the D4R secondary building units. These D4R units are typically preferentially enriched by germanium atoms in contrast to the zeolitic layers that these D4R units connect[37]. Hence, the chemo-selective hydrolysis of these Ge-rich D4R units can generate two-dimensional (2D) layered zeolite precursors that offer fascinating possibilities for post-synthesis modifications and can be subsequently used as building blocks for the synthesis of new zeolite frameworks[1-6]. The example of germanosilicate zeolites containing D4R interlayer motifs that are particularly suitable for this method are UTL, UOV, IWW and *CTH[13]. Especially the germanium-rich UTL has been successfully utilized for the ADOR process, with D4R units undergoing hydrolysis under neutral or acidic conditions to produce stable 2D layered IPC-IP material[4-5]. Understanding the factors which control the chemo-selective hydrolysis from 3D into 2D layered zeolites is very important for the targeted syntheses of new zeolite frameworks.

The selective controlled demetallation of zeolites is necessary for a series of industrial applications, such as the formation of mesoporous and hierarchical zeolite frameworks to

enhance catalytic applications[26, 34-36]. The degree and type of demetallation (dealumination or desilication) in zeolite frameworks is affected by many factors such as Si/Al ratio, pH value or water content. At high Si/Al ratios and high water content (*e.g.*, at hot liquid water conditions) the desilication is more likely in zeolites, while the dealumination is favoured at low Si/Al ratios under steaming or acidic liquid water conditions[38]. On the other hand, the desilication is preferred over dealumination in the alkaline water solution[31]. The selective desilication of the framework reduces the Si/Al ratio and changes the properties related to the Si/Al ratio of the zeolite, such as cation exchange capacity and catalytic activity[39]. In addition, selective desilication in mild alkaline water solution can also produce regular mesopores in the framework without substantially changing the framework structure[34, 40-42]. For example, Groen *et al.*[34] analyzed the mesoporosity of alkali-treated zeolite MFI at different Si/Al ratios and they found that the optimal range of Si/Al ratio for the formation of controllable intracrystalline mesopores by desilication is 25-50, while lower Si/Al ratios impede the silicon etching, whereas too high Si/Al ratios result in uncontrolled framework decomposition and loss of crystallinity.

Dealumination post-treatment is a method of adjusting the aluminum concentration and the relative concentrations of different types of aluminum-based reactive centers (mostly characterized as either Lewis or Brønsted acid sites) in aluminosilicate zeolites. The representative technological process for dealumination is steaming (*i.e.*, exposing zeolites to water steam at high temperatures), which is a common method for modifying the acidic properties, stability, and textural features of zeolites, and is widely used in the production process of industrial aluminosilicate zeolites catalysts[31, 43-44]. The state of aluminum in the zeolites strongly affects its performance in many important catalytic processes, hence, the character of aluminum species created during the dealumination process has been extensively studied both experimentally and theoretically[45-52]. Dealumination creates a manifold of Lewis acid sites (LAS) that are associated with the zeolitic catalycic activity[48, 53-54]. Although the details of Brønsted acid sites (BAS) in zeolites are well established, the details of LAS, that are expected to involve flexible aluminum coordinations between the tetrahedrally coordinated aluminum Al(Td) and octahedrally coordinated aluminum Al(Oh), are not comprehensively understood at present[43]. Experimentally, steaming treatment of H-BEA[49] and H-MOR[46] have confirmed that Al(Oh) species can be formed at laboratory temperature, with NMR chemical shifts for Al(Td) and Al(Oh) being found at 50-60 and 0 ppm in ^{27}Al MAS NMR, respectively. It is assumed that there are two types of Al(Oh) species: the extra-

framework one and the framework-associated one, and the latter type can reversibly switch its coordination between Al(Td) and Al(Oh) under certain conditions. For example, van Bokhoven *et al.*[49] found that Al(Oh) in zeolite Beta can be quantitatively converted into Al(Td) when the temperature is higher than 395 K. Although both Al(Td) and Al(Oh) species are generally confirmed by experimental spectroscopic fingerprints, their structures and inter-conversion pathways at the atomic level are still unclear.

1.3 Hydrolysis mechanisms

The hydrolysis mechanism of zeolite has attracted a lot of detailed experimental and computational investigations in recent decades[31]. The experimental aspects studied the zeolite stability under aqueous or steaming conditions by many experimental techniques, in particular, powder X-ray diffraction (PXRD), X-ray absorption spectroscopy (XAS), atomic absorption spectroscopy, magic angle spinning solid-state nuclear magnetic resonance (MAS NMR), infrared spectroscopies (IR), scanning electron microscopy (SEM), and gravimetric and volumetric analysis. For instance, Ravenelle *et al.*[55] investigated the hydrothermal stability of zeolites Y and ZSM-5 with different Si/Al ratios in hot liquid water (150 and 200 °C) using different experimental techniques to detect structural changes. They found that the zeolite hydrolysis is strongly dependent on the framework type. Zeolite Y has been shown to be hydrolytically rather instable with instability increasing with increasing Si/Al ratio. It was amorphized when the Si/Al ratio was greater than 14 at 200 °C, with the Si-O-Si siloxane bonds rather than Al-O-Si bonds being predominantly hydrolyzed. In contrast, ZSM-5 zeolite remained stable under the same conditions. Later, Agostini *et al.*[56] investigated dealumination of NH_4-Y zeolite by *in situ* XAS and PXRD. They found that water starts to re-adsorb at about 500 K and that the dealumination process takes place predominately only after the water re-adsorbtion during the cooling and that only a small fraction (<10%) dealumination is taking place during the heating.

Zeolite hydrolysis mechanisms have been intensively studied computationally, especially the mechanism of desilication and dealumination[7, 31, 54, 57-63]. Most studies focused on low water concentration conditions, at which typically only a single water molecule reacts with the framework in each hydrolysis step. The typical hydrolysis process is the one in which a single T site is removed from the framework with four T-O-T bonds broken forming a silanol nest and an extra-framework species, *e.g.*, $Si(OH)_4$ or $Al(OH)_3 \bullet H_2O$. For instance, Malola *et al.*[59] performed density functional calculations to investigate the detailed reaction paths for zeolite

desilication and dealumination mechanism by the sequential addition of single water molecule at each step of the reaction (see Figure 1.3a). They found that dealumination is the least activated of the two, but both dealumination and desilication showed unfeasibly high barriers (*e.g.*, for the $Q^4 \rightarrow Q^3$ step the barrier were 260 kJ mol^{-1} for dealumination and 300 kJ mol^{-1} for desilication), due to the choice of mechanism, which involved formation of a highly unstable vicinal disilanol intermediate. Silaghi *et al.*[60] discovered a new more feasible mechanism (see Figure 1.3b) for the first step of dealumination and calculated the activation energy to be in the range of 76-125 kJ mol^{-1} depending on T site and the zeolite in question. The following work of Silaghi *et al.*[64] confirmed similar activation energies for further steps of the stepwise low-water dealumination process for multiple zeolites and multiple T sites. The most activated part of these steps is an *equatorial* step in which the water binds to the T atom, dissociates with the hydrogen atom from the water (H_w) being transferred to the framework oxygen (O_f), and then the *equatorial* T-O bond is broken (see Figure 1.3b). *Equatorial* mechanism has been proposed earlier for silica surfaces[65], *i.e.*, in the context of desilication, in computational studies using cluster models. The most relevant in the current context were the studies of Pelmenschikov *et al.*[58, 63] investigating the single water molecule attacks on the Si-O-Si bonds. The hydrolysis barrier for the first step, *i.e.*, for the $Q^4Si \rightarrow Q^3Si$ transformation, is 205 kJ mol^{-1} and it ends up with the formation of an unstable Q^3Si product with two neighboring silanols in an orientation favoring reverse reaction. The subsequent hydrolysis steps required lower barriers than the first hydrolysis step (down to 75 kJ mol^{-1} for $Q^1Si \rightarrow Q^0Si$ step), and it was related to the decrease in local framework rigidity decreases. In summary, under neutral conditions, the zeolite hydrolysis under low-water conditions is expected to proceed via the *equatorial* mechanism[58, 63-70].

There have been only few investigations which consider the role of water cooperativity on the mechanism of zeolite hydrolysis[7, 61-62]. Using silica cluster models Cypryk and Apeloig[66] showed that a new mechanism of the Si-O-Si bond hydrolysis is possible, with lower barriers and more stable products when several water molecules are involved in the process. Recently, Nielsen *et al.*[62] investigated the dealumination at steaming conditions in periodic zeolite models considering up to three water molecules taking part in the Al-O-Si bond hydrolysis, showing that the water cooperativity is able to modestly decrease the activation barriers by up to 20 kJ mol^{-1}. Taking it a step further in our group, Heard *et al.*[7] employed a fully solvated CHA model to study the first step of desilication with biased ab initio molecular dynamics at ambient conditions (300 K) and discovered a new favorable desilication mechanism, the *axial*

mechanism (see Figure 1.3c). In the *axial* mechanism the proton from the water attacking the silicon atom is shuttled via Grotthuss-type mechanism through a water chain (including 4-5 water molecules) to the *axial* framework oxygen, breaking the Si-O-Si bond and inverting the SiO_3OH tetrahedron. The free energy activation barrier for the breaking of the first Si-O-Si bond is as low as 65 kJ mol^{-1}, which indicates that the aluminosilicate zeolites are labile even at ambient conditions. Therefore, under high water loading conditions, water cooperativity can introduce new favorable hydrolysis mechanisms and considering the role of water cooperativity is essential for understanding the zeolite hydrolysis process.

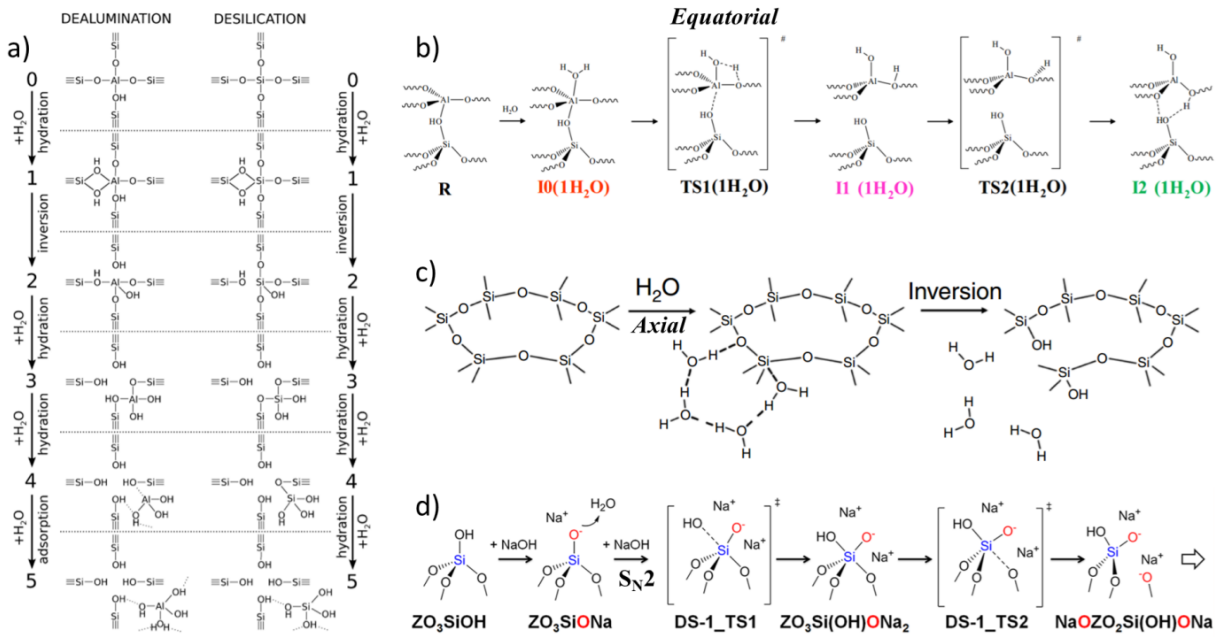

Figure 1.3: Summary of the hydrolysis mechanisms reported in the literature. a) The schematic diagrams for dealumination (left) and for desilication (right) in zeolite Y by formation of vicinal disilanol intermediates. Reproduced with permission[59]. Copyright 2012, John Wiley and Sons. b) The reaction scheme of an Al−O(H) bond breaking in MFI initiated by the water adsorption on Al. Reproduced with permission[64]. Copyright 2016, Elsevier. c) The *axial* mechanism for fast room temperature partial zeolite hydrolysis in H-CHA under high-water conditions. Adapted with permission[7]. Copyright 2019, Springer Nature. d) The schematic illustrations of reaction paths of the desilication process in alkaline conditions via the S_N2 mechanism. Reproduced with permission[71]. Copyright 2015, American Chemical Society.

While the zeolite hydrolysis mechanisms at neutral conditions are being currently extensively investigated, the hydrolysis mechanisms under alkaline conditions are still poorly understood at present. At alkaline conditions, the existence of OH^- generating species (such as NaOH) can reduce the reaction barrier and enhances the hydrolysis of silicates[40-42, 69]. However, there are very few studies that consider the role of NaOH in the hydrolysis process. The sodium ion has relatively large volume and has a strong affinity for water molecules. The first hydration shell of Na cation is consisting of approximately 5 water molecules[72], which corresponds to 5 waters/cage in small-pore zeolite CHA in the high water loading conditions (water density is about 1 g cm^{-3})[7]. In addition, the position of the cation in framework will directly affect the properties of the zeolite, such as ion exchange and catalytic performance. For the zeolite with D6R, the Na cation tends to occupy the face of the six-membered ring site under the anhydrous condition[73-74]. Hence, the presence of Na cations is likely to have an effect on hydrolysis reaction mechanism, either directly or indirectly through its role as a water adsorption center, and the presence of Na cation on quartz surfaces has been shown to stabilize activated Si complexes[65]. Some works have explored the relationship between pH and desilication rate[58, 63, 65, 69, 71, 75], however, most calculations used the silica cluster model and did not consider the effect of explicit solvent and explicit base molecules (only OH^- attack). Such models are helpful for understanding possible reaction routes[75], however, the ignorance of the solvent, explicit base molecules and cluster confinement effects makes the accuracy of those models questionable. For NaOH desilication reactions, only a few studies have explicitly evaluated the presence of the cation[65, 71]. Tamada *et al.*[65] used a cluster model to investigate the NaOH-catalyzed desilication on the surface of quartz, and found that the presence of sodium ions can stabilize activated Si complexes. However, the sodium ions did not participate in the hydrolysis reaction and it was not examined whether NaOH could directly split the siloxane bonds. The direct NaOH attack on Si-O-Si bond at the surface of zeolite ZSM-5 was explored by Zhai *et al.*[71]. Their mechanism is stepwise deprotonation of silanol groups by S_N2 attack by OH^- anion, causing the scission of Si-O-Si bond into adjacent Si-OH and $Si\text{-}ONa^+$ fragments (see Figure 1.3d). This mechanism is characterized by very low reaction barriers, but it ignores the influence of solvent and assumes large NaOH consumption, which is a reactant rather than a catalyst. All previous investigations also focused on hydrolysis mechanism starting at the zeolite surfaces, however, previous research shows that selective desilication hydrolysis occurs also at zeolite interior, particularly at the internal silanol defects[76]. Overall, the role of bases at the atomistic level, in accelerating the desilication of zeolites is still quite unclear at present.

Vast majority of previous studies focused on atomistic scale understanding of the hydrolysis process in aluminosilicate zeolites. However, only a few studies have investigated the reactive interaction of water in other heteroatom-substituted zeolites, such as Sn- and Ti-substituted zeolites[77-80]. For Ge-substituted zeolites, for which the degermanation mechanism is a key step to predicting the behavior of ADORable zeolites under hydrolytic conditions, the hydrolysis mechanism has not been studied computationally at all so far. Some calculations have analyzed the distribution of germanium atoms in BEC and UTL zeolites and they found that Ge preferential occupies the T-sites in D4R[37, 81-83]. Furthermore, density functional theory (DFT) calculations predict that Ge atoms prefer to form clusters compared to the separated configuration in D4R unit[37, 82], but the synergistic effect of Ge clusters on its hydrolytic stability is still unclear. In addition, those few investigations are limited by various factors such their focus on low-water conditions, neglect of temperature effects, and the static nature of those calculations, which miss the dynamical effects that are expected to be important as shown for hydrolysis of aluminosilicate zeolites (see above). Hence, the research on the hydrolysis mechanisms of other heteroatom-substituted zeolites than aluminosilicates is still far from being complete at present.

1.4 The significance, aim and content of this study

Nowadays, the development of petrochemical industry is facing the huge challenge of resource shortage. The use of new processes, new technologies, new materials, and the pursuit of energy savings and consumption reduction in petrochemical processes have become an inevitable trend in petrochemical development. At the same time, the development of new processes for preparing petrochemical products from coal, natural gas, and biomass to solve the problem of resource shortage has been a research hotspot in recent years. In addition, cleaner production, environmental protection, and greenhouse gas emission reduction and conversion are also research focal point. By addressing these new demands, zeolite catalysts are faced with many problems and challenges, such as how to further improve the performance and efficiency of the catalyst, whether the design and synthesis of the zeolite can be controlled, how to further reduce the cost of the synthesis, and how can be zeolites applied in new fields. Given the fundamental importance of hydrolysis processes in zeolite catalyst upgrading, understanding zeolites hydrolysis mechanism is of great significance in terms of catalysis and zeolite science.

Many intriguing experimental techniques are used to study the structure, stability and catalytic activity of zeolites. However, predominantly only the macroscopic properties of the (catalytical) reactions in zeolites can be obtained in experiments. The formation mechanism of the catalyst itself, the specific distribution of acid centers, the structure and energy characteristics of the transition states in the catalytic reaction and other microscopic information cannot be easily obtained from experiments, so theoretical calculation methods must be used. Quantum chemical calculations can analyze the structure of the catalyst at the atomic level, describe the adsorption, diffusion, reaction and desorption process of the reactants during the catalytic reaction. This microscopic information can be compared with the experimental observables to obtain a deeper and more comprehensive understanding of the entire reaction process, which in turn can assist in designing of improved catalysts in the actual chemical production.

The aim of this study is to design a simulation that would have a high overlap with the experimental set-up and investigate systems of high complexity under realistic conditions. Using biased *ab initio* molecular dynamics (AIMD) one can obtain accurate free energy pathways from reactants to products under realistic conditions. We intend to systematically study zeolite hydrolysis mechanism under realistic conditions, with an explicit consideration of temperature, solvation, and pH effects. Various hydrolysis mechanisms under different reaction conditions were analyzed. The main research content of this study includes:

(1) We focus on charting the disassembly pathways of germanosilicate UTL and uncovering the role of water and germanium content on hydrolysis at the atomic scale. The non-reactive water physisorption and the reactive water chemisorption on the zeolite framework are investigated. The mechanisms of the hydrolysis step are examined sequentially for different germanium concentration in both the low-water conditions (single water in the unit cell) and the high-water conditions (zeolite pores filled with water at the density ~ 1 g cm^{-3}). Through systematic calculations and analysis, we identify the modes of interaction between water molecules and the UTL framework under different conditions, clarify the role of water molecules and Ge concentration in the hydrolysis process, and identify the specific hydrolysis mechanisms with their corresponding reaction energies along the energetically favorable reaction routes.

(2) We are concerned about the atomistic understanding of mechanism of selective desilication of zeolites under alkaline conditions. We investigate the hydrolysis mechanism in

the interior pores of the zeolite under neutral and alkaline conditions. Starting from the pristine silicious zeolite CHA model, we considered several different hydrolysis mechanisms and classified them according to the different roles the water and NaOH can take on in the mechanisms such as them being reactants, spectators or catalysts. For all mechanisms, we not only consider low-water conditions but explore the influence of the increased water loading, *i.e.*, the hydrolysis taking place under microsolvation conditions. We analyze the role of water molecules and NaOH in the hydrolysis process, understand the cooperative mechanisms at play, and define the likely reaction routes under different reaction conditions.

(3) We focus on determination of the nature of up-to-now obscure framework-associated octahedrally coordinated aluminum Al(Oh) in CHA zeolite. The computational investigation is carried out on a CHA model that as closely as possible matches the experimental conditions including high water concentration (Si/Al = 3 with six water molecules per unit cell). The structural properties and formation path at ambient conditions of framework-associated Al(Oh) is described in detail. The factors influencing the formation and stability of framework-associated Al(Oh) are determined first and their role is evaluated. These factors include Si/Al ratio (proxy to the Brønsted acid sites (BAS) concentration), distance between framework Al atoms, and water concentration.

2. Methods and models

2.1 Methods

2.1.1 Density functional theory (DFT)

DFT is a method of *ab initio* calculations. The basic idea of *ab initio* calculations is to solve the Schrödinger equation by numerical calculations, to obtain the properties of the molecular or periodic systems. This method can reasonably calculate almost all the ground state properties of the molecular or periodic systems using only a few physical constants as an input (such as the speed of light, the mass and charge of electrons and nuclei, Planck's constant, *etc.*) and this calculation method does not need to rely on any experimental parameters or on any system-specific parametrizations. DFT, in its Kohn-Sham formulation (see below), has been successfully used to describe the behavior of atoms, molecules, surfaces, crystals systems and their interactions[84-85]. It can provide sufficiently high computational accuracy at manageable computation cost (typically scaling as $O(N^3)$ with the system size) and is able to routinely treat systems with high hundreds of atoms. The theoretical foundations of DFT are based on the Hohenberg–Kohn theorems which state that all observable properties of a ground state system are determined by the electron density

$$\rho(\vec{r}) = N \int \dots \int \left|\Psi(\vec{X}_1, \vec{X}_2, \dots, \vec{X}_N)\right|^2 ds_1 d\vec{X}_2 \dots d\vec{X}_N \quad (2.1)$$

and access to the true N electrons wave function $\Psi(\vec{X}_1, \vec{X}_2, \dots, \vec{X}_N)$ is not necessary. The electron density is easier to handle both conceptually and in the practical applications.

Hohenberg - Kohn Theorems

Two Hohenberg - Kohn theorems give the theoretical basis for using electron density as the basic variable to determine the physical observables of the multi-electron systems[86] :

H-K theorem 1: For any electronic system in an external potential, $V_{ext}(\vec{r})$ is a unique functional of ρ_0. It means that there is a unique mapping between the ground state density $\rho_0(\vec{r})$ and the ground state energy E_0.

$$E_0(\rho_0) = \int \rho_0(\vec{r}) V_{ext} d\vec{r} + F_{HK}[\rho_0] \quad (2.2)$$

$F_{HK}[\rho_0]$ is Hohenberg-Kohn functional, it is the sum of the kinetic energy and the electron-electron repulsion operator.

H-K theorem 2: The energy functional $\mathrm{E}[\tilde{\rho}]$ is for any valid trail density always larger than the one for the ground state density. The $\mathrm{E}[\tilde{\rho}]$ will give the lowest energy of the system only if the $\tilde{\rho}$ is a true ground state density.

$$\mathrm{E}[\tilde{\rho}] \geq E_0[\rho_0] \tag{2.3}$$

H-K theorems guarantee that the total ground state energy of any multi-electron system can be uniquely determined by the charge density and, having access to the exact H-K functional, they provide us with a variational expression to obtain true ground state density. However, the exact form of $F_{HK}[\rho_0]$ is unknown and hence such variational expression is not of practical importance.

Kohn-Sham theory

The main idea of the Kohn-Sham theory is to introduce a non-interacting reference system that has the same ground state density as the interacting system, splitting the kinetic energy functional into interacting and non-interacting part. The non-interacting part can be evaluated accurately using orbitals, and it constitutes the major part of the kinetic energy. The interaction between electrons is described by an effective (local) external potential (*i.e.*, assuming non-interacting reference system representability), with majority of terms (with respect to the size of their contribution to total potential/energy) having known forms, and the complicated interactions of the unknown exact form all placed in the exchange-correlation functional $\mathrm{E}_{XC}[\rho]$:

$$\mathrm{E}_{DFT}[\rho] = T_S[\rho] + E_{ne}[\rho] + J[\rho] + E_{XC}[\rho] \tag{2.4}$$

$$\mathrm{E}_{XC}[\rho] = (T[\rho] - T_S[\rho]) + (E_{ee}[\rho] - J[\rho]), \tag{2.5}$$

where $T_S[\rho]$ is the kinetic energy of non-interacting reference system, $E_{ne}[\rho]$ is the electron-nucleus interaction energy, $J[\rho]$ is the classical Coulomb repulsion, with $\mathrm{E}_{XC}[\rho]$ containing the residual part of kinetic energy, electron exchange and electron correlation. $T[\rho]$ is the kinetic energy of interacting system, and $E_{ee}[\rho]$ is the electron-electron interaction energy.

Applying variational principle to Kohn-Sham functional along with constrain on the orthonormality of the Kohn-Sham orbitals leads to one-electron Kohn-Sham equations which need to be solved in a self-consistent iterative way. The general procedure can be expressed as shown in Figure 2.1: First, one obtains a trial charge density, from which the initial Hamiltonian can be constructed. Second, one solves the Kohn-Sham equations obtaining the

Kohn-Sham orbitals from which an updated electron density is calculated. This process is then iterated until convergence. The converged electron density (and orbitals) can be then used to calculate the energy and other properties (*e.g.*, force) of the system.

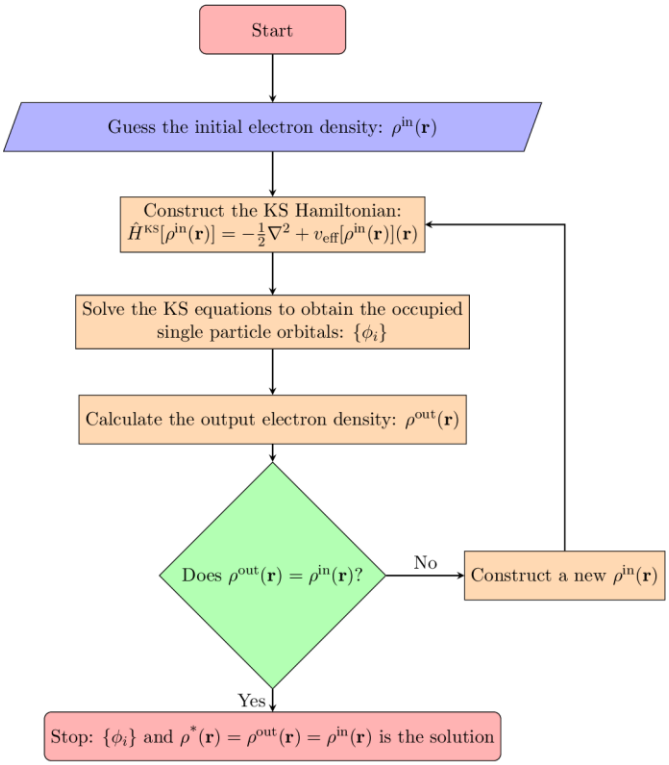

Fugure 2.1: The scheme of the Kohn-Sham self-consistent iterations[87].

Exchange-correlation functional $E_{XC}[\rho]$

The exact form of the $E_{XC}[\rho]$ is unknown in general. Therefore, approximating the form of the $E_{XC}[\rho]$ has become a very important factor restricting the development of DFT. Many approximate expressions of $E_{XC}[\rho]$ have been proposed (local density approximation, generalized gradient approximaiton, meta-GGA functionals, hybrid funtionals, *etc.*) which enable DFT to reach accuracy similar or better than that of Hartree-Fock method at the comparable cost[85, 88]. The most computationally efficient approximations are the Local Density Approximation (LDA)[89-91] and Generalized Gradient Approximation (GGA)[92-94], with the latter being the most popular approximation within the DFT framework.

Under the LDA approximation, the $E_{XC}[\rho]$ can be expressed in the following form:

$$E_{XC}^{LDA}[\rho] = \int \rho(\vec{r})\varepsilon_{XC}\big(\rho(\vec{r})\big)d\vec{r} \ , \tag{2.6}$$

where $\rho(\vec{r})$ is the electronic density and $\varepsilon_{XC}\big(\rho(\vec{r})\big)$ is the exchange-correlation energy per particle of a uniform electron gas of density $\rho(\vec{r})$.

The core idea of LDA is that we can divide a multi-electron system into an infinite number of volumetric microelements dV and assume that exchange correlation energy of each volumetric microelement is the same as if the microelement was a part of the uniform electron gas with the density $\rho(\vec{r})$ at a given point $\vec{r}$. The expressions for the $\varepsilon_{XC}(\rho)$ for the uniform electron gas are known analytically for exchange term or can be very accurately obtained from interpolation of numerical results for correlation term. LDA was found, somehow surprisingly, to provide good accuracy not only when the electron density changes slowly with the spatial coordinates, *e.g.*, for metals, but work at least qualitatively also for molecular systems, which was related to the LDA exchange-correlation holes satisfying most of exact constraints (such as sum rules)[84].

The early proposal of LDA was an important step in DFT. However, in typical applications, the local electron density will change with spatial coordinates. In order to improve over the shortcomings of LDA, later approximations considered the gradient of the electron density $\nabla\rho(\vec{r})$ to affect the exchange correlation term. Including the nonuniform electron density in the expression of the exchange correlation functional, GGA expression is as follows:

$$E_{XC}^{GGA}[\rho(\vec{r})] = \int \rho(\vec{r})\varepsilon_{XC}\big(\rho(\vec{r})\big), |\nabla\rho(\vec{r})|d\vec{r} \tag{2.7}$$

In general, GGA improves over LDA across the board at a cost of negligible increase in computational time and is still an approximation of choice for majority of applications in the material science field. All calculations in this dissertation are performed using exchange correlation functional at the GGA level of approximation.

2.1.2 Semi-empirical dispersion-corrected DFT (DFT-D)

Most quantum mechanical electronic structure calculations are based on DFT. DFT has achieved great success in many respects. Nevertheless, there are some challenges such as the correct description of the dispersion forces (part of intermolecular interactions)[95-96]. The leading term of dispersion interactions (for non-overlapping densities) is given by the (C_6/R^6) dependence on the atomic distance, where the C_6 is the pair-specific dispersion coefficient, which determines the strength of the interaction. However, standard DFT approximations

(such as LDA or GGA) does not have a correct attractive long-range dispersion R^{-6} limiting behavior, hence, most standard DFT functionals provide a purely repulsive interaction between rare gas atoms.

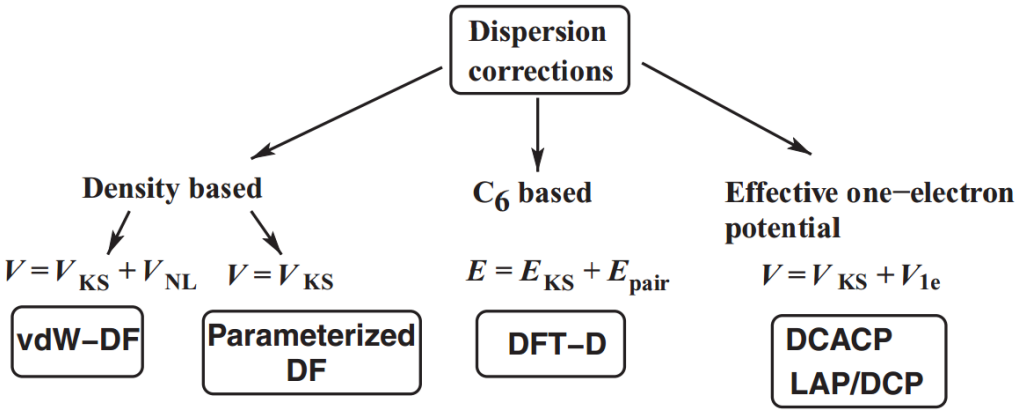

Figure 2.2: Summary of the dispersion corrections methods in DFT. Reproduced with permission[97]. Copyright 2011, John Wiley and Sons.

Many different dispersion correction methods[97-99] have been proposed, which can be roughly grouped into four classes as shown in Figure 2.2. Among them, the most popular and computationally efficient is the (semi)empirical DFT-D group of methods proposed by Grimme *et al.*[97, 100-101], which accounts for dispersion interaction by adding terms of a general form:

$$E_{disp}^{DFT-D} = -\frac{1}{2}\sum_{A\neq B}\sum_{n=6,8,10,\ldots} S_n \frac{C_n^{AB}}{R_{AB}^n} f_{damp}(R_{AB}) \qquad (2.8)$$

Where C_n^{AB} denoted the nth-order (n= 6, 8, 10, …) dispersion coefficient for the atom pair AB, R_{AB} represents the distance between AB atoms, and S_n are the scaling factors.

The important ingredient in all DFT-D methods is the damping function f_{damp}. The damping function is used to adjust the behavior of dispersion correction in the short- and mid-range distance to avoid double-counting problem as standard exchange correlation functional can account for part of this short- and mid-range dispersion. All calculations in this work used dispersion correction method termed D3[100], with Becke-Johnson damping[101] (DFT-D3(BJ)).

2.1.3 *Ab initio* molecular dynamics (AIMD)

Most of the so-called *static* (*ab initio)* calculations explore a very small subset of mostly critical points (minima, transition states, *etc.*) of the system's potential energy surface (PES) which can be expected to be sufficient for simple systems (*e.g.*, crystals of hard matter, simple catalytic reaction, *etc.*) in ultra-high vacuum (UHV) conditions. However, for complex systems under realistic conditions, such as zeolites in interaction with reactive liquid at elevated temperatures investigated herein, much broader sampling of the PES, ideally with a correct Boltzmann weight (*i.e.*, sampling of the free energy surface) is necessary[102]. Molecular dynamics (MD) simulations can achieve exactly that, describing the equilibrium structures of a system of interest at various temperatures and even being able to track the transformation processes, if either the MD is run for long enough time or if it is biased towards the transformation (see Section 2.1.5 below). Starting from the initial configuration, the MD numerically propagates the system in time (using finite time step) according to the Newton's equations of motion:

$$-\frac{dV}{d\vec{r}} = m\frac{d^2\vec{r}}{dt^2} \tag{2.9}$$

Where V is the potential energy at position $\vec{r}$, the vector $\vec{r}$ contains the coordinates for all the particles, the t is time.

The interaction between atoms (and the force between atoms) can be calculated by different methods. Our AIMD method of choice is the Born-Oppenheimer MD (BOMD), in which the nuclei are treated classically (*i.e.*, using equation 2.9) and the interaction between the atoms are treated quantum mechanically, using DFT method in our case[85]. This means that at each time step one need to convergent the Kohn-Sham wave function and calculate the corresponding forces on atoms. These forces then determine the acceleration of the atom and allow the coordinates and velocities of the atom to pass to the next time step. Repeating this process many times will produce a series of configuration snapshots, which describe the trajectory of the system in phase space. The AIMD simulation is a good method to study the zeolite framework and its interaction with adsorbed molecules at complex conditions. The AIMD can also be used to study the time-dependent dynamic properties of the system, such as diffusion coefficients, reaction/transformation kinetics, *etc.* In recent years, this method has become one of the most advanced and important methods of computational simulations, however, it is still quite costly and hence the typical AIMD runs nowadays are limited to tens

or low hundreds of picoseconds.

2.1.4 Climbing image nudged elastic band method (CI-NEB)

The nudge elastic band (NEB) method is one of the chain-of-states search methods for finding transition states[103-104]. The transition state structure refers to the highest point (saddle point) of energy on the reaction path on the potential energy surface (PES), which connects the structure of the reactant and the product through the minimum energy path (if it is a multi-step reaction, besides reactants and products it also includes intermediates). This method inserts a series of structures between the reactant and the product. A total of *P*-1 points (structures) is inserted, the reactant number is 0, and the product number is *P*, keeping the 0 and *P* points stationary, and the other points are affected by the force from the PES and the springs force along the band connecting neighboring points. Following the constrained optimization maintaining the equal spacing between the points, the points at the end of the optimization describe the minimum energy path on the given PES.

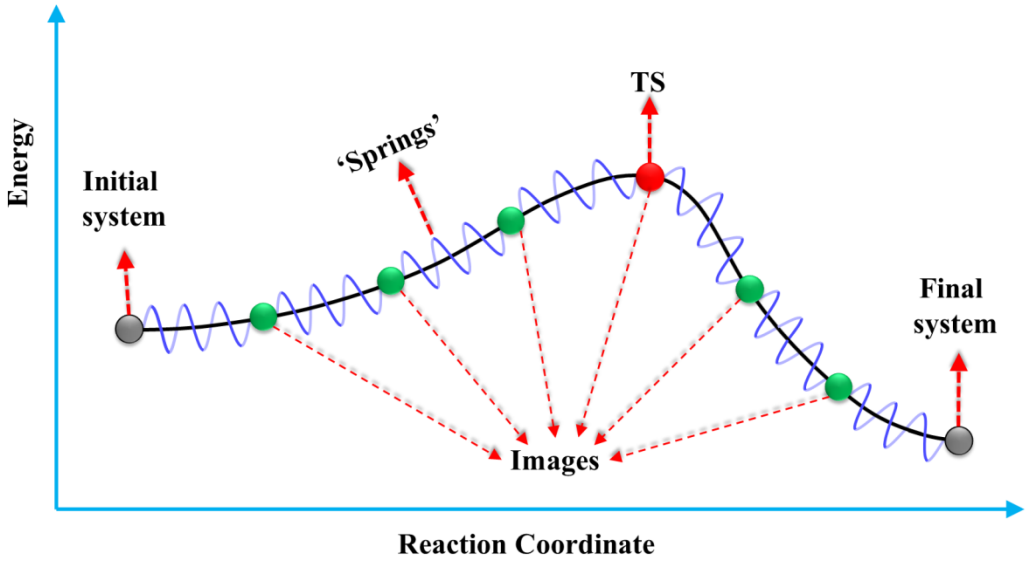

Figure 2.3: The schematic diagram of CI-NEB method to calculate the transition states.

The CI-NEB[105-106] is an improved method with small modification to the original NEB method. As shown in Figure 2.3. The key difference between CI-NEB and NEB is the definition of the force on the point with the highest energy, *i.e.*, on the tentative transition state: in CI-NEB, this point will not be subjected to the spring force of the adjacent point to avoid the position being pulled away from the transition state, and the true potential energy

component along the tangent is reversed. This method requires only a few points between the initial and final states to accurately locate the transition state. It is one of the most efficient and popular methods to locate the transition states.

2.1.5 Slow growth and thermodynamic integration methods (SG and TI)

On the time scales accessible to the AIMD, the chemical reactions are considered rare events. Hence, the MD typically needs to be biased along a low-dimensional representation of a chemical reaction/transformation in an atomic structure space, *i.e.*, along the reaction coordinate or also known as collective variable (CV), to accelerate sampling of these improbable events. Slow growth (SG)[85, 107] and thermodynamic integration (TI)[108] methods allow us among other things, to extract free energy profiles from these biased MD runs. In the SG the transformation between two systems A and B is broken up into a series of smaller intermediate steps using a coupling parameter λ, *i.e.*, the scaled CV equivalent, with λ taking on values from 0 to 1. The energy of the system can be written as a general function of λ:

$$\mathrm{E}(\lambda) = \lambda E_B + (1 - \lambda) E_A \tag{2.10}$$

The free-energy difference between two systems A and B can be calculated by assuming that at every simulation step the Hamiltonian is infinitesimally perturbed in λ:

$$\langle \mathrm{A} \rangle_B - \langle \mathrm{A} \rangle_A = \lim_{d\lambda \to 0} \sum_{\lambda=0}^{1} (E_{\lambda + d\lambda} - E_\lambda) \tag{2.11}$$

One may imagine this change to be realized during a single simulation by continuously changing λ slightly in each time step ($d\lambda \to 0$), making the energy difference in any given interval arbitrarily close to zero. For the proper convergence, this method requires that the increase of λ is slow enough to ensure that the system essentially remains at equilibrium at all times. However, in this thesis, the SG calculations only provides us with the initial trial free-energy pathways (typically providing upper bounds to free energy barriers and reaction energies due to rather fast and thus non-equilibrium nature of the pulling force) and the initial trial structures connecting reactants to products. These are later refined using the TI method.

In the TI method, the reaction coordinate is again approximated by a parameter λ, *i.e.*, the CV. The free-energy difference between two systems A and B can be calculated by an ensemble average of free-energy gradient at a constrained value of λ and integration over λ, as shown below:

$$\langle A \rangle_B - \langle A \rangle_A = \int_0^1 \langle \frac{\partial F}{\partial \lambda} \rangle \, d\lambda \approx \sum_{\lambda=0}^{1} \langle \frac{\partial F}{\partial \lambda} \rangle_\lambda \triangle \lambda \quad (2.12)$$

The free-energy gradient with respect to λ is evaluated at fixed values of λ, and the integral may be approximated by a discrete sum. This process is defined as the thermodynamic integration method[108]. The choice of proper collective variable(s) which reasonably approximates the reaction coordinate is a crucial point in all biased MD methods and represents itself an active field of research[109-110].

2.1.6 Calculations details

For all calculations within this work, we used plane-wave density functional theory (DFT) implementation within the *Vienna Ab initio Simulation Package* (VASP 5.4 code)[111-114]. The projector-augmented-wave (PAW) method is used to describe the core electrons, and the Perdew–Burke–Ernzerhof (PBE) exchange correlation functional[92] (a GGA type) is employed throughout. To capture the dispersion interactions, which are known to be important in zeolites[115-116], the (semi)empirical dispersion correction termed DFT-D3[100-101] with Becke-Johnson damping is added. The plane wave cutoff energy is 400 eV and only gamma point k-point sampling is used in all calculations. We fully relax positions of all the atoms in the studied systems until the force on each atom is less than 0.01 eV $Å^{-1}$, and the corresponding energy convergence standard is 10^{-6} eV per unit cell. Atomic charges were estimated via the crystal orbital Hamiltonian population method as implemented within the LOBSTER code.[117] The *ab initio* molecular dynamics (AIMD) simulations were always run in the canonical (NVT) ensemble with a time step of 0.75 fs with hydrogen atoms mass-reweighted to tritium to enable longer time steps. The target temperature used for the nGe-UTL model (see section 2.2.1) is 370 K, which corresponds to the most common hydrolysis temperature during the experiment. The target temperature used for the CHA model is 300 K. The temperature value is controlled by the Nosé-Hoover thermostat[118].

The constrained MD simulations combined with TI[108] are applied to determine the Helmholtz free energy barriers and reaction energies. The appropriate collective variables (CVs) are selected based on assumed reaction mechanisms and are typically formed by a combination of bond distances describing formation and breaking of the chemical bonds during the transformation process (see examples in Figure 2.4.). For the nGe-UTL model (see section 3.1) the CVs used for various mechanisms are described in Figure 2.4 (bonds taking part in CV are highlighted in red and CVs' formulas added below the reaction schemes). Initial

configurations for the biased MD runs were extracted both from the equilibrated AIMD simulations for reactants/products and the approximate slow growth (SG) simulations along the reaction profile defined by the CV. Then the TI simulations were employed to generate Helmholtz free energy gradients at a set of 15 to 35 configurations, which were selected along the SG trajectory fixing the value of the CV at each configuration. A total of (at least) 10 000 steps in TI calculations was performed for each configuration with timestep 0.75 fs, and the average value of free energy gradients were obtained from the last (at least) 7000 steps. The final free energy profile was obtained through integration of the free energy gradient along the reaction path from reactant to product.

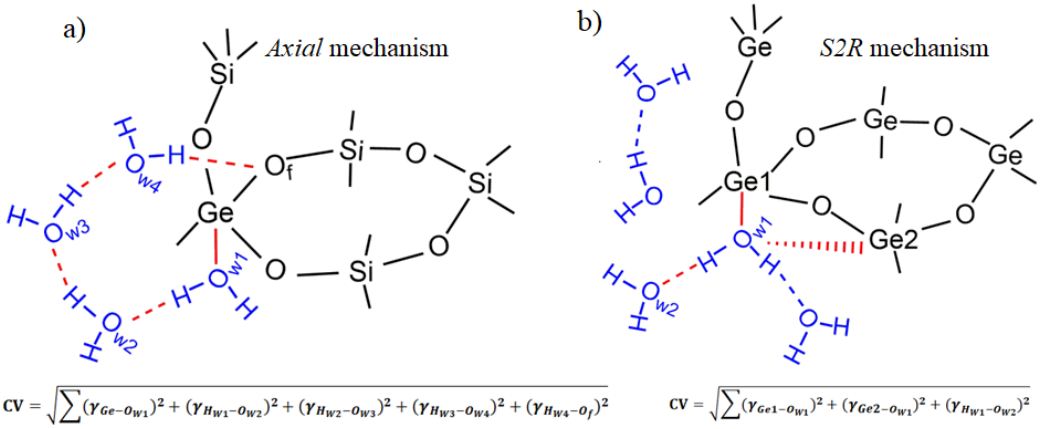

Figure 2.4: Examples of the CVs employed to study different hydrolysis mechanisms. a) Ge–O_f cleavage within the *axial* mechanism. b) Ge–O_f cleavage within the *S2R* mechanism.

For the CHA model (see section 3.3) the coordination number between Al atom and the oxygens of water (O_w) was used as a CV:

$$CN = \sum_{i=1}^{6} \frac{1-(d_i/c_i)^9}{1-(d_i/c_i)^{14}} \qquad (2.13)$$

where d_i is the distance of Al atom and the O_w oxygens and all c_i coefficients were set to 2.3 Å (*i.e.*, an approximate cut-off value for the Al-O_w bond). The TI simulations were employed to generate Helmholtz free energy gradients at a grid of at least 45 (macro)states covering the transformation from reactant (BAS(4)) to product (LAS(6)) via two intermediate states. To improve TI convergence, the initial configuration of each (macro)state was constructed by using the last configuration from the TI calculation at a neighboring grid point combined with a very short SG simulation (approx. 100 steps with a step size of ±0.0005). The average value

of free energy gradients was calculated from at least 30 ps long TI calculations for each macro(state) using all the data points for ensemble averaging.

For all static calculations, barriers were calculated by the CI-NEB method[105-106]. The energetics of reaction steps are described by reaction energy (E_r) and reaction barrier (activation energy E_a). We make a distinction between intrinsic and effective barrier (E_a^{int} and E_a^{eff}). The intrinsic barrier E_a^{int} refers to the energy barrier in an elementary reaction step that connects an initial state local minimum and a final state local minimum via a single transition state. The effective barrier E_a^{eff} is the overall relative height between the highest energy transition state and the reactant state along the multiple step reaction. These quantities are defined using the following equations:

$$E_r = E_{FS} - E_{IS} \tag{2.14}$$

$$E_a^{int} = E_{TS} - E_{IS} \tag{2.15}$$

$$E_a^{eff} = E_{TS*} - E_{IS} \tag{2.16}$$

Where the E_{IS} is the total energy of the initial state, the E_{FS} is the total energy of the final state, and the E_{TS} is the total energy of the transition state in target reaction step. E_{TS*} is the highest energy transition state along the multiple step pathways from reactants to products.

The water adsorption energies in zeolites were calculated via the following equation:

$$E_{ads} = E_{zeo-nH_2O} - E_{zeo} - n * E_{H_2O} \tag{2.17}$$

Where E_{zeo-nH_2O} is the total energy of water adsorbed in zeolites (UTL, CHA), E_{zeo} is the total energy of the zeolite cell without water, E_{H_2O} is the energy for a single isolated water molecule in the gas phase, and *n* is the number of adsorbed water molecules.

The energy cost of removing one water molecule from the Al(Oh) species is calculated as follows:

$$E_{rem} = E_{Al(Oh)\_(n-1)H_2O} + E_{H_2O} - E_{Al(Oh)\_nH_2O} \tag{2.18}$$

Where $E_{Al(Oh)\_nH_2O}$ are the total energies of the Al(Oh) species with different amount of water in its vicinity and E_{H_2O} is the energy for a single isolated water molecule in the gas phase.

2.2 Models

2.2.1 Zeolite UTL

The zeolite UTL model was obtained initially from the IZA database[11]. The UTL unit cell parameters were fully optimized using the purely siliceous framework and were subsequently fixed during all later calculations. The UTL models used in this work can be in general expressed using formula $Si_{38-n}Ge_nO_{76}$ (n = 0, 1, 2, 3, 4, 8), termed as nGe-UTL models. The UTL models contains a total of 114 framework atoms with the following unit cell parameters *a=16.29 Å, b=14.04 Å, c=12.44 Å, α=90.00°, β=103.80°, γ=64.46°*. UTL has 12 symmetry inequivalent T atoms, however, we focused our studies only on subset of representative sites (following the IZA database notation, some T sites are depicted in Figure 2.5a). In the low-water loading UTL model, only one water molecule is added to the nGe-UTL unit cell. In high-water loading model, following the IZA database value for the accessible volume fraction of 21.88% and assuming water density ~1 g cm^{-3} in the pores, 18 water molecules are added to the UTL channels. The initial structure of high-water loading system is obtained using the gromacs *solvate* module[119], which overlaps the zeolite unit cell with the cubic box containing equilibrated bulk water molecules. The Figures 2.5b and 2.5c show representative structures of 8Ge-UTL model (all eight silicon atoms in the D4R are substituted by germanium atoms) with low- and high-water loading, respectively.

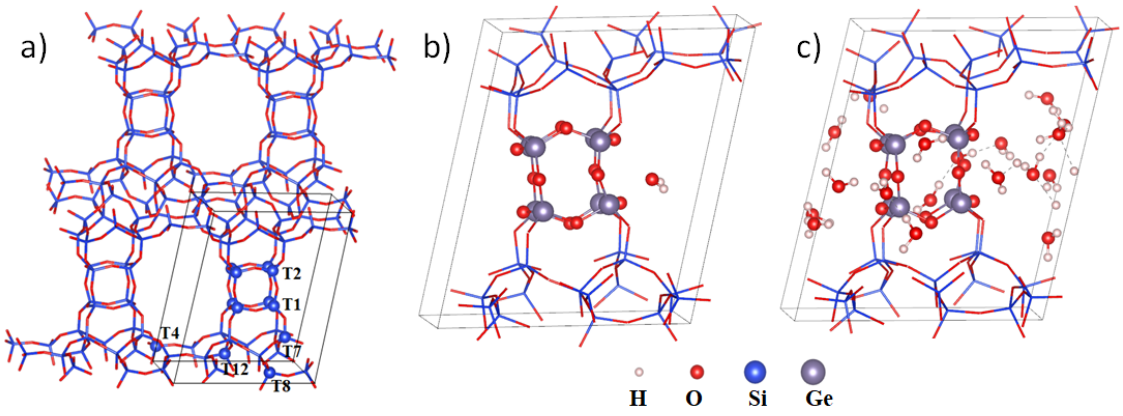

Figure 2.5: a) The purely siliceous UTL structure and six representative T sites used in the study. b) The structure of 8Ge-UTL model with one water added. c) The structure of 8Ge-UTL model at high-water loading.

2.2.2 Zeolite CHA

The silicious chabazite (CHA) model was obtained from the IZA database[11], and the cell parameters were subsequently re-optimized using the aluminosilicate model of CHA (Si/Al=11) with water molecules present in the framework[7]. CHA contains only one type of T site and each T site is connected to four inequivalent oxygen atoms (O1, O2, O3, O4 as marked in the Figure 2.6). Each oxygen atom is a part of three rings, O1 is a part of a 6-ring and two 4-rings, O2 is a part of one 4-ring and two 8-rings, O3 is a part of 4-ring, 6-ring and 8-ring, and O4 is a part of an 8-ring and two 4-rings. Standard unit cell used in Section 3.2 is a supercell containing 36 T sites, as shown in Figure 2.6a. The final lattice parameters are: *a=13.76 Å, b=13.81 Å, c=14.30 Å, α=90.05°, β=89.88°, γ=119.79°*. The desilication process (Section 3.2) was studied sequentially, *i.e.*, the T site was removed completely from the framework with four T-O-T bonds broken one at a time forming a silanol nest and an extra-framework species. The hydrolysis mechanism was studied under varying water (from 1-15 per unit cell) and NaOH (from 1-4 per unit cell) concentrations. The initial structure of high water loading (15H_2O per unit cell) was also obtained via the gromacs *solvate* module[119] (see section 2.2.1 above for details).

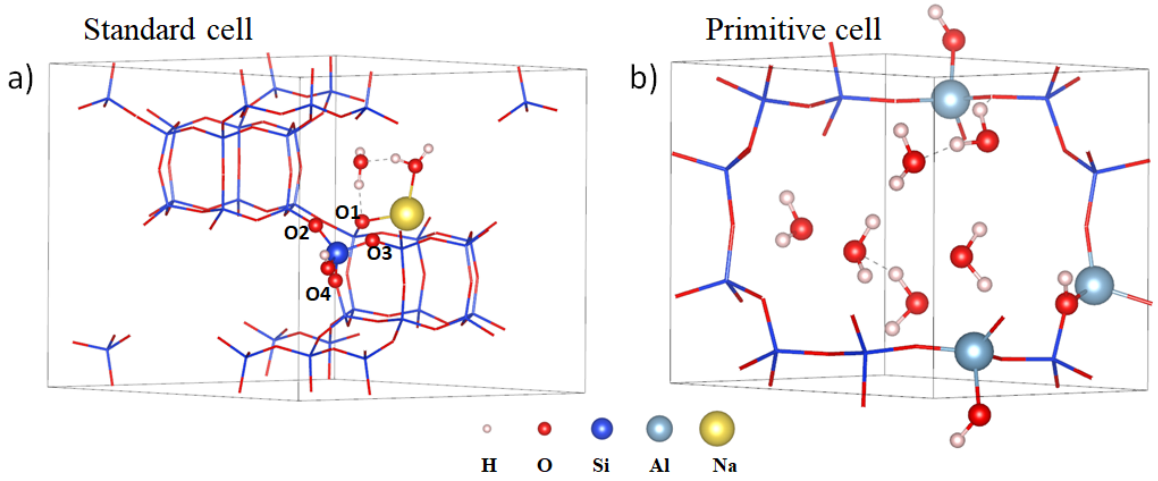

Figure 2.6: a) The standard unit cell of CHA with one NaOH and two water molecules. b) The primitive cell of CHA with Si/Al=3 containing six water molecules.

The model of CHA zeolite used in section 3.3 is the CHA primitive cell, which contains 12 T sites. The re-optimized unit cell parameters are: *a=b=c=9.286 Å, α=β=γ=96.015°*.

Calculations were performed with Si/Al ratios of 11 and 3. Figure 2.6b depicts a representative CHA structure with a Si/Al ratio of 3 containing six water molecules. Note, that there must be an Al-O-Si-O-Al pair in D6R due to topology reasons at Si/Al=3. For Si/Al=3 we tested all possible proton sites and lowest energy configuration was chosen. We considered two different water loadings: 6 and 3 water molecules in the unit cell. The $6H_2O$/UC loading is in perfect agreement with the amount of water determined gravimetrically in the experiment at ambient temperature for CHA sample with Si/Al=3[120].

3. Results

3.1 Hydrolysis mechanism of germanosilicate zeolite UTL[121]

3.1.1 Low water and low Ge conditions

The low Ge model corresponds to a UTL unit cell with one silicon atom substituted by a germanium atom, named 1Ge-UTL. The low water condition means that there is only one water molecule in the UTL channel system. Three types of T sites are investigated: the T sites located in D4R (T1 and T2), T site adjacent to D4R (T7) and T sites located in the UTL layer (T4, T8 and T12), as shown in Figure 2.5a. The adsorption energy of one water molecule in 1Ge-UTL models is summarized in the Table 3.1. We have defined two types of water adsorption complexes. The first type is the *O-down* complexes, in which the water forms close Ge-O_w contacts with the minimum O_w-Ge distance in range of 2.34-2.83 Å. The second type is the *H-down* complexes, in which the water rather forms close contact with framework oxygens (O_f-H_w), with the minimum H_w-O_f distance in range of 2.04-2.52 Å. In general, the *H-down* complexes are less stable than *O-down* complexes by 5-10 kJ mol^{-1}. The average water adsorption energy in 1Ge-UTL models is approximately only -28±6 kJ mol^{-1}, which is consistent with the previously reported work for water adsorbing on Ge-BEA[122]. Interestingly, the water adsorption energy of 1Ge-UTL is not much improved compared with the pristine purely siliceous UTL (-19 kJ mol^{-1}), which indicates that the isolated germanium does not have much affinity towards the water molecules. Therefore, we can conclude that pristine UTL with low concentration of germanium (Si/Ge >37) is almost as hydrophobic as the purely siliceous framework.

Table 3.1: The adsorption energy (E_{ads} see section 2.1.6 equation 2.17) of one water molecule on 1Ge-UTL models (Ge sitting at different T sites) and purely siliceous UTL.

T sites	*O-down*		*H-down*	
	1Ge	All Si	1Ge	All Si
T1	-25	--	-20	-19
T2	-30	--	-20	-18
T7	-24	--	-17	-23
T8	-22	--	-28	-34
T4	-38	--	-29	-31
T12	--	--	-22	-28

Although the pristine germanosilicate UTL appears hydrophobic, the scission of the Ge-O-Si bond can cause the formation hydrophilic groups such as silanols and germanols groups. We thus comprehensively investigated the hydrolysis of Ge-O bond in the 1Ge-UTL model. The hydrolysis of Ge-O bonds in low Ge conditions is initiated via an *equatorial* mechanism reported previously[63, 66-68, 70, 123], see Figure 3.1a, with the reaction barriers of at least 65 kJ mol^{-1} and rather unstable products (endothermic reactions with reaction energies above 33 kJ mol^{-1}). We considered only three representative T sites (T1, T4, and T7). The hydrolysis of multiple symmetrically inequivalent Ge-O bonds for each T site were considered (see Figure 3.1b-d). The *equatorial* mechanism starts with the approach of a water molecule to the Ge-O bond. The water oxygen (O_w) atom interacts weakly with the Ge atom, with a local minimum on the potential energy surface corresponding to adsorption (see previous section). A four center transition state is reached, in which a bond is formed between O_w and Ge, and a second bond is formed between water hydrogen (H_w) and the framework oxygen (O_f) adjacent to Ge. These new bonds are formed as the intramolecular water O-H bond and the framework Ge-O bonds are weakened. The reaction is completed to form an unstable Q^3Ge product, comprising of adjacent germanol and silanol groups. The germanol and silanol groups are well aligned to undergo the reverse dehydroxylation mechanism, which heals the framework and releases a water molecule[58, 63]. This facile dehydroxylation has been previously proposed to explain the slow kinetics of zeolite desilication. In addition, formation of similarly unstable (Er ~ 60 kJ mol^{-1}) *equatorial* Q^3Ge products was reported also for low-germanium Ge-BEC models[77].

The instability of the *equatorial* products lead us to consider alternative hydrolytic products and we found a stable Q^3Ge product (E_r = 2-14 kJ mol^{-1}), the *axial* product, from which the further hydrolysis may proceed. The *axial* Q^3Ge products are formed upon inversion of the Ge(-OH)(-OSi)$_3$ tetrahedron at germanium atom accompanied by transfer of (Ge)-OH group to *axial* position with respect to initially adjacent silanol group (see Figure 3.1a). Similar inversion mechanisms were reported earlier for tin-containing zeolites[78-79]. The inversion is not always favorable, in particular for the T sites located in the UTL layer, since for some of the symmetrically inequivalent Ge-O bonds (T1-(O1,O2), T4-(O15,O18,O19), T7-(O1,O19), the inversion ends up in germanol group being in large steric repulsion with the framework (see Figure 3.1b-d). In case of favorable inversion steps (T1-(O3,O4), T7-(O14,O21), the inversion is associated with the activation barrier of approx. 35-45 kJ mol^{-1}, making the overall effective barrier for breaking the first Ge-O bond in UTL as high as 100-120 kJ mol^{-1}. We denote this whole two-step process as an *equatorial-inversion* mechanism. The most

favorable low-energy hydrolysis path is the path for the scission of the Ge(T1)-O3 bond located in D4R with the effective energy barrier of 106 kJ mol^{-1} and the reaction energy of only 2 kJ mol^{-1}.

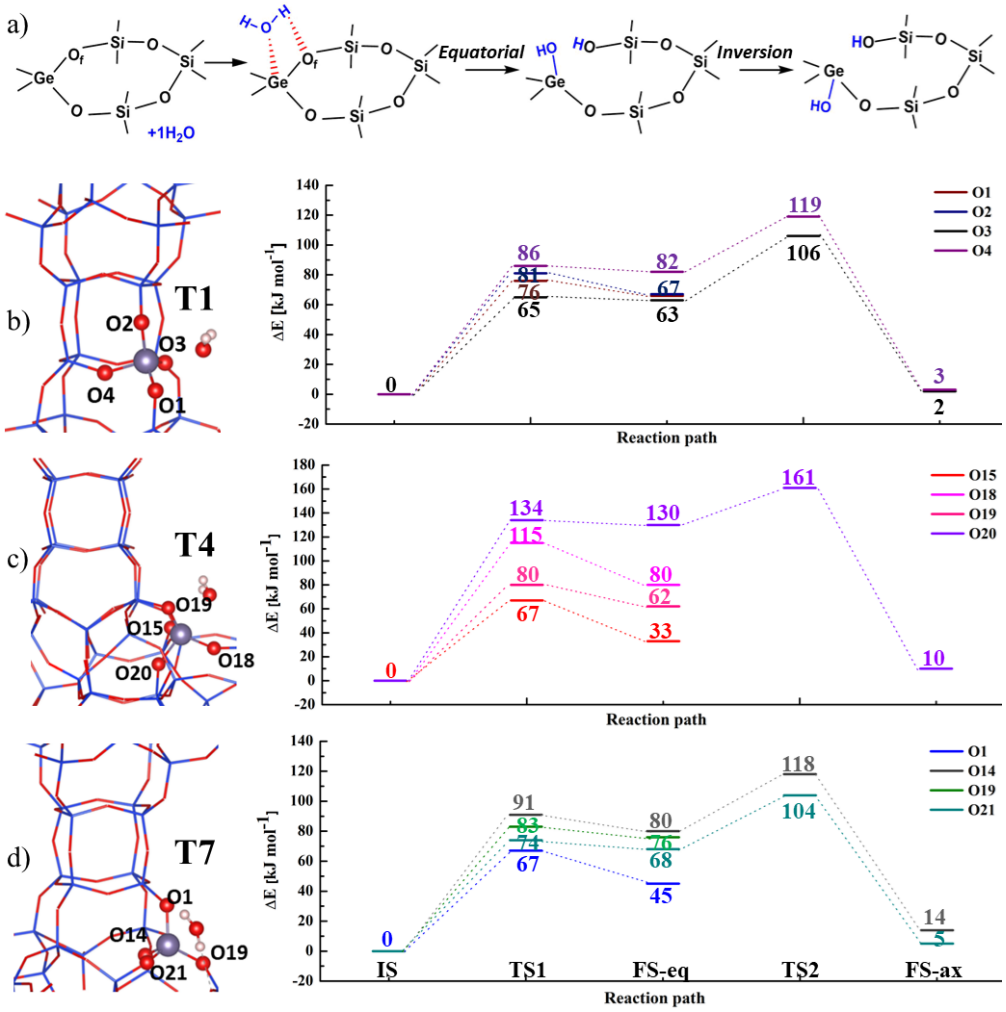

Figure 3.1: a) The schematic diagram of *equatorial-inversion* mechanism. b)-d) The potential energy profiles for the first Ge-O bond scission (the $Q^4 \rightarrow Q^3$ hydrolysis step) with Ge atoms located at T1, T4 and T7 sites, respectively.

Starting from most favorable Q^3 hydrolysis product, *i.e.*, with the Ge(T1)-O3 bond broken, we calculated the further hydrolysis steps employing *equatorial* mechanism until the full removal of an $Ge(OH)_4$ group from the framework. The results are shown in the Figure 3.2. Each step of the hydrolysis reaction is accompanied by the adsorption of an additional water molecule, with the water molecule splitting and breaking one Ge-O bond at each step. The reaction energy for $Q^3 \rightarrow Q^2$ step is 10 kJ mol^{-1}, for $Q^2 \rightarrow Q^1$ step it is -3 kJ mol^{-1} and for $Q^1 \rightarrow Q^0$ step it

is 24 kJ mol^{-1}. The reaction energies for these later hydrolysis steps are much more favorable than for the first $Q^4 \rightarrow Q^3$ step and thus do not necessitate the inversion step to stabilize the products. The products of later steps (Q^2, Q^1, Q^0) apparently benefit from larger flexibility of the partially hydrolyzed Ge center, being able to rotate away from the alignment optimal for the reverse dehydroxylation. The reaction barriers for the subsequent steps are 74 kJ mol^{-1}, 84 kJ mol^{-1} and 83 kJ mol^{-1}, respectively, and they are all lower than the reaction barriers of the $Q^4 \rightarrow Q^3$ step, indicating that the first step hydrolysis is the rate-limiting step.

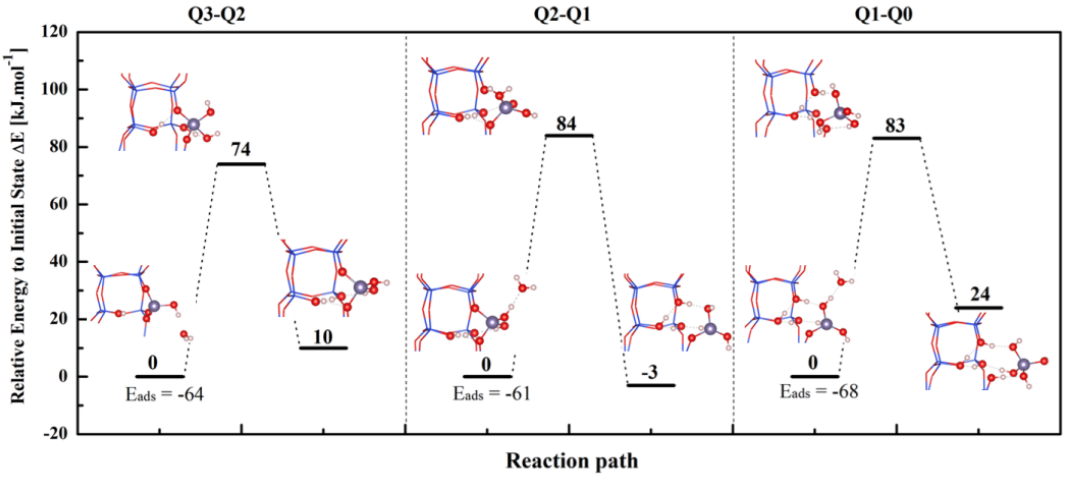

Figure 3.2: The reaction profile for the further hydrolysis steps following the *equatorial* mechanism from Q^3Ge to Q^0Ge. The most stable structures with adsorbed water molecule at each step are considered as the initial states and their energy is set to 0 kJ mol^{-1}.

The silanol and germanol groups formed after the first step hydrolysis step greatly improve the hydrophilicity of the 1Ge-UTL models. Water molecule is able to form a strong hydrogen bond with the germanol group of the hydrolytic intermediates, with water oxygen (O_w) acting as hydrogen bond acceptor and the germanol oxygen (O-Ge) as a hydrogen bond donor, *i.e.*, the Ge-OH•••O_w-H_2 motif is formed. Hence, the water adsorption energies at the hydrolytic intermediates (see Figure 3.2) in the UTL channel are -64 kJ mol^{-1} for the Q^3Ge product, -61 kJ mol^{-1} for Q^2Ge product and -68 kJ mol^{-1} for Q^1Ge product. Such stabilization is comparable to the stabilization of a water molecule in liquid water at room temperature[124-125] (approximately 60-70 kJ mol^{-1} since water molecule in liquid can form about 3.5 hydrogen bonds, each about 20 kJ mol^{-1} strong) or only slightly lower than the stabilization of water on Brønsted acid sites in zeolites[126] (approximately 80 kJ mol^{-1}). Since the water adsorption

energy in pristine 1Ge-UTL models (see Table 3.1 above) is approximately 30 kJ mol^{-1}, this means that the affinity of water molecules to UTL has increased by more than twice after partial hydrolysis.

3.1.2 Low water and high Ge conditions

We have also investigated the role of increased concentration of germanium in the UTL framework on the water adsorption and reactivity. These models are denoted as nGe-UTL (n = 2, 3, 4, 8) and the corresponding most stable single water adsorption configuration are depicted in Figure 3.3. We focused on increasing germanium content in D4R unit only, which means that only germanium substitution in T1 and T2 sites is considered. The focus on germanium substitution in D4R is in line with previous studies which report that Ge atoms in UTL tend to occupy primarily the D4R unit[37, 81-83].

Compared to 1Ge-UTL models, the water adsorption energies increase only once more than two (adjacent) germanium atoms are present in the D4R unit. The increase in stabilization (over the most stable 1Ge-UTL T2 site with 30 kJ mol^{-1}) is consistent but rather mild (in range of 2-6 kJ mol^{-1}). Enhanced stabilization can be tracked to changes in the structure of water adsorption complex. Namely, starting from 3Ge-UTL model, water is able to interact with both germaniums forming a D4R edge, inducing formation of two penta-coordinated germanium centers by occupying one of the vertices of the trigonal bipyramid (see Figures 3.3d-f). Admittingly, the perturbation of the initial tetrahedral arrangement of Ge centers towards trigonal bipyramid is rather mild (the two O_w-Ge close contacts are approx. 2.47-2.99 and 3.09-3.78 Å, respectively) but the tendency of water to insert in-between two Ge atoms is quite clear. The fact that we do not observe similar behavior for 2Ge-UTL model seems to be related to increased flexibility of D4R unit at higher Ge content. In particular, we relate it to sharper Ge-O-Ge angles (in range of 125-135°) in comparison to Ge-O-Si angles (135-150°) in D4R[127-128], which allow for facile formation of (two) adjacent trigonal bipyramids (see Figure 3.3d-f). Despite a rather minor additional stabilization of water brought about by increased Ge content, one can distinguish intriguing non-trivial changes in structure of water adsorption complexes in UTL models with high Ge content, that can have pronounced effects not only for water physisorption but also for the reactive water interaction with Ge-UTL.

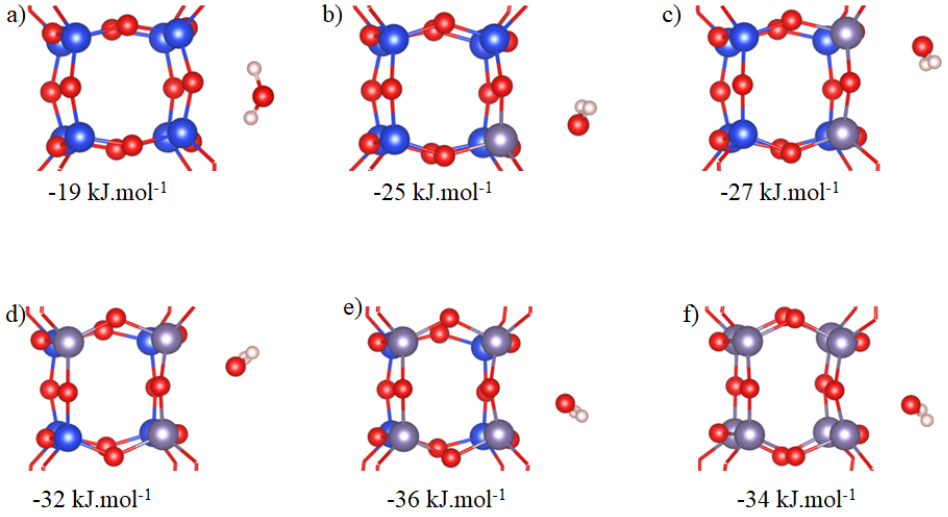

Figure 3.3: The representative water molecule adsorption complex structures with different degree of germanium substitution in D4R. a) The pristine purely siliceous UTL, b)-f) the nGe-UTL (n =1, 2, 3, 4 and 8) models.

In order to consider the affinity of water molecules to the germanium Lewis sites more realistically, we also considered the influence of temperature using *ab initio* molecular dynamics (AIMD) simulations on all nGe-UTL (n = 0, 1, 2, 3, 4, 8) models. All calculations were performed for approximately 20 ps with the temperature set to 370 K. The trajectory of water molecules indicates that water molecule can move freely in the 12/14R channels, however, it does preferentially occupy the adsorption 'pockets' above the purely siliceous 5- and 8-rings at the bottom of the channels (see Figure 3.4a). Evaluation of the mean internal energy U for these adsorption 'pockets' indicates that the water molecule is more stable in the 12R than in the 14R by ~10 kJ mol^{-1} (see Figure 3.4b for a representative 8Ge-UTL model). The germanium adsorption sites observed in static calculations (see above) are visited during the AIMD simulations, but only very briefly, with the minimum distance between water molecules and germanium atom staying most of the time above 3 Å (see Figure 3.4c), this is significantly more than for the static *O-down* water complexes on germanium Lewis sites discussed in the previous section, for which the O_w-Ge distance is in a range of 2.34-2.83 Å. Hence, at low water loading conditions, the water affinity for germanium Lewis sites decreases with the increasing temperature up to a point that germanium Lewis sites become dynamically unstable at 370 K.

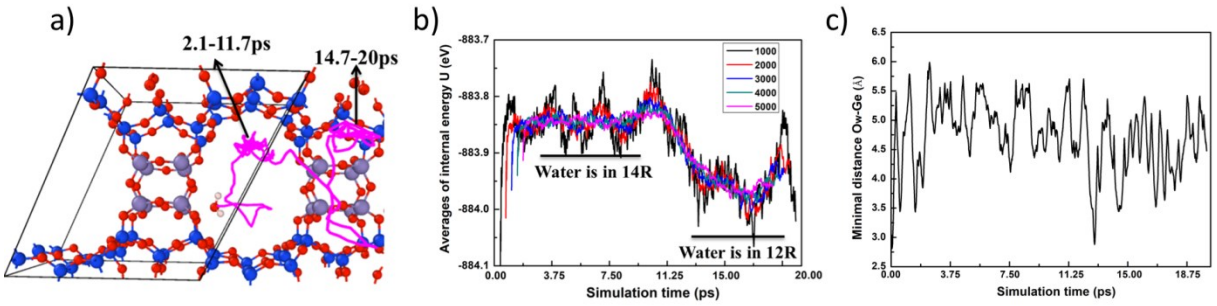

Figure 3.4: a) The trajectory lines (pink lines) of a single water molecule adsorbed in 8Ge-UTL model during the AIMD simulation. b) The averages of the internal energy during the equilibrium AIMD run on the same model. c) The minimal distance between O in the water molecule and Ge atoms during AIMD simulation on the same model.

In high Ge conditions, the hydrolysis of UTL can commence via another more competitive mechanism, the *geminal* mechanism (see Figure 3.5a). The *geminal* mechanism starts with water adsorbing in-between two Ge atoms in D4R edge (see also Figure 3.3f). In the transition state, the incoming water deposits one of its hydrogens (H_w) to the framework oxygen (O_f) of the Ge-O_f-Ge unit, with the remaining OH group attaching to one of the Ge atoms in the Ge-O_f-Ge unit. The reaction is finalized by distortion of the D4R unit that allows OH group from water to bridge to the second germanium in the Ge-O_f-Ge unit. The final *geminal* product contains the Ge-(O_fH_w)(O_wH_w)-Ge motif, in which both Ge centers are five-coordinated with all Ge-O bonds being mildly elongated (1.93-1.99Å in the *geminal* motif and 1.77-1.85 Å for other remaining Ge-O bonds).The *geminal* mechanism has an activation barrier of 70 kJ mol^{-1} and reaction energy of 29 kJ mol^{-1}, which is significant improvement over the (best) competing *equatorial* route at the T1 site (E_r = 60 kJ mol^{-1} and E_a = 86 kJ mol^{-1} for *equatorial* step only and E_a = 82 kJ mol^{-1} for *equatorial* step followed by *inversion* – see Figure 3.5b). Similar *geminal* mechanisms were reported earlier for (alumino)silicate zeolites by Malola *et al.*[59], although much higher reaction barriers were observed when either *geminal* disilanols or *geminal* aluminol and silanol pair were formed. From the *geminal* product the hydrolysis can proceed further via the standard *equatorial* mechanism. We exemplify this by investigating the hydrolysis of the Ge-O bond on the Ge center hosting the Ge-(O_fH_w)(O_wH_w)-Ge motif. This hydrolysis is now very exothermic (E_r = -49 kJ mol^{-1}) with the product reminiscent of the *axial* Q^3Ge product in low Ge case (see section 3.1.1). The product keeps the *geminal* digermanol motif and is apparently stabilized by the internal germanol-germanol hydrogen

bond (see Figure 3.5c). Hence, increasing germanium content is apparently capable of significantly improving the probability of germanosilicate UTL hydrolysis to commence even at low water concentration conditions. However, the activation barriers are still sizable (and initial reactions are quite endothermic) and thus one should not expect a particularly fast hydrolysis taking place under such conditions.

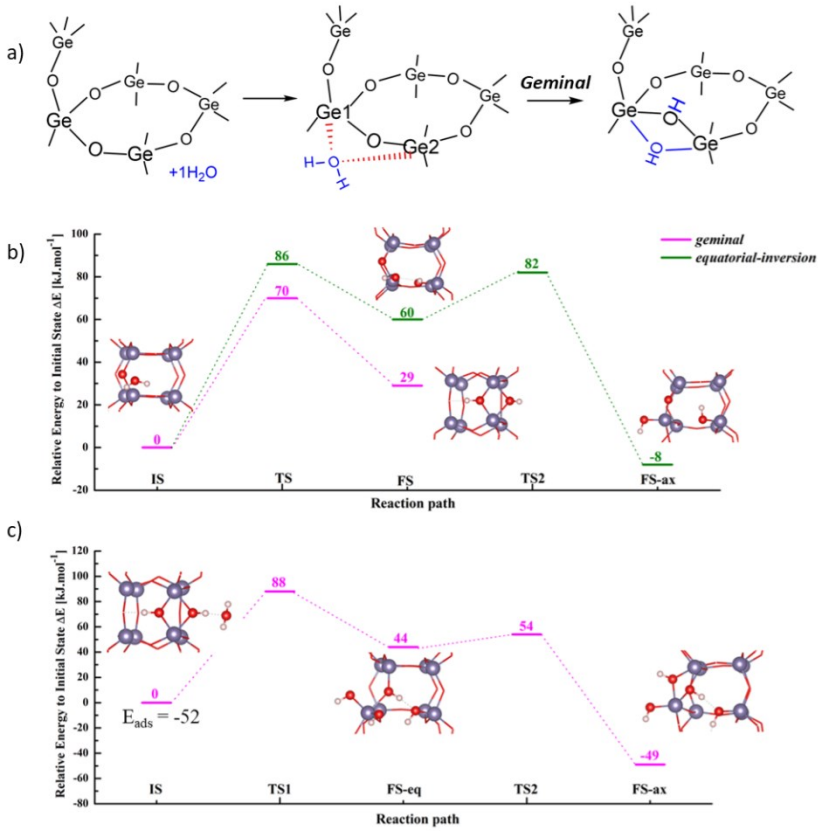

Figure 3.5: a) The schematic diagram of the *geminal* mechanism. b) The potential energy profile for the initial hydrolysis step in the 8Ge-UTL model via the *geminal* mechanism (pink line) and *equatorial-inversion* mechanism (green line). c) The potential energy profile for the further hydrolysis steps after the formation of the *geminal* product.

3.1.3 High water and low Ge conditions

Using the AIMD simulations complemented with the methods of biased dynamics (slow growth and thermodynamic integration), we first investigated the hydrolysis mechanism of 1Ge-UTL models at high water loading, which means that there are 18 waters in the UTL unit cell. In this low Ge conditions, we focused on the model with germanium substituted in D4R

unit (at T1 site). First, we performed 40 ps equilibrium AIMD simulation. During this AIMD run, a water molecule binds to germanium atom to form a five-coordinated Ge center, as shown in Figure 3.6a., with the O_w-Ge bond being much shorter (as low as 1.9 Å) than observed even for the most stable *O-down* complexes in the static low water concentration case (see Section 3.1.1 above), for which the O_w-Ge bond is at least 2.3 Å long. The Ge center becomes five-coordinated with five almost equivalent Ge-O bonds (approximately in the range of 1.80 Å to 1.96 Å). However, the five-coordinated Ge center is not stable throughout the whole trajectory with water desorbing from germanium after few ps. Nevertheless, water molecules stay rather close to Ge site (minimal O_w-Ge distance is approx. 3.9 Å) and attempts to adsorb on it intermittently (see Figure 3.6b). In general, increasing water molecules content seems to improve the affinity of water molecules to the germanium Lewis sites and the five-coordinated Ge centers can be formed at least intermittently.

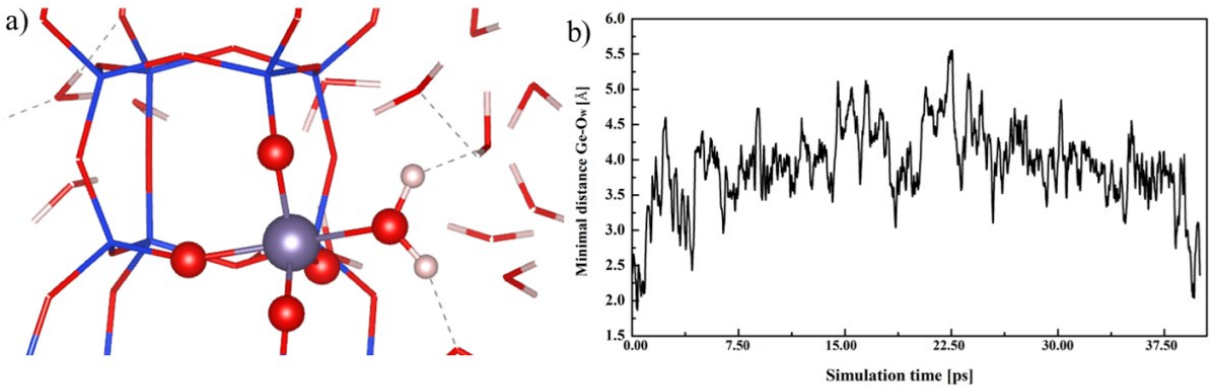

Figure 3.6: a) Snapshot from the AIMD simulation of the 1Ge-UTL model filled with water depicting water molecule adsorbing on the Ge atom inducing formation of the five-coordinated Ge center. b) The minimal distance between all oxygen atoms from the water solvent and germanium atom during the AIMD simulation of the same model.

The five-coordinated Ge centers turned out to be intermediates in a novel low-barrier Ge-O hydrolysis mechanism that leads directly to formation of stable *axial* Q^3 products (see Figure 3.7a). The free energy barrier, $\Delta A^{\neq}$, for the reaction mechanism, denoted as *axial*, is as low as 37 kJ mol^{-1} and it is calculated through thermodynamic integration of constrained AIMD simulations. The mechanism starts with the water adsorption on the Ge atom and formation of the five-coordinated Ge center. Next, a proton is detached from the adsorbing water and shuttled via a chain of solvent water molecules between this interacting water and the adjacent

framework oxygen in an *axial* position. The proton shuttled via the Grotthuss mechanism helps breaking the Ge-O bond, which is followed by inversion of the $Ge(O)_3OH$ tetrahedron, and the mechanism finishes with the formation of silanol and germanol groups that are in *anti*-positions to each other, *i.e.*, the *axial* Q^3 product. The *axial* Q^3 product is similarly to the low water loading case, only by 11 kJ mol^{-1} less stable than the reactants (see Figure 3.7b). Basically, the same mechanism has been observed previously by some of us for Si-O-Si hydrolysis in purely silicious CHA model[7], hinting at a more general nature of such mechanism, that could be expected to take place at higher water loadings also for other heteroatoms such as tin or titanium. The *axial* reaction mechanism has been studied only for hydrolysis at O3 framework oxygen atom, however, we expect similar mechanism and similarly low barriers to take place also for O4 oxygen. For O1 and O2 oxygens, due to the framework topology, we do not expect *axial* mechanism to apply due to steric constraints of the reaction products with the germanol group ending up either inside the D4R unit or in the *t-non* composite building unit, respectively.

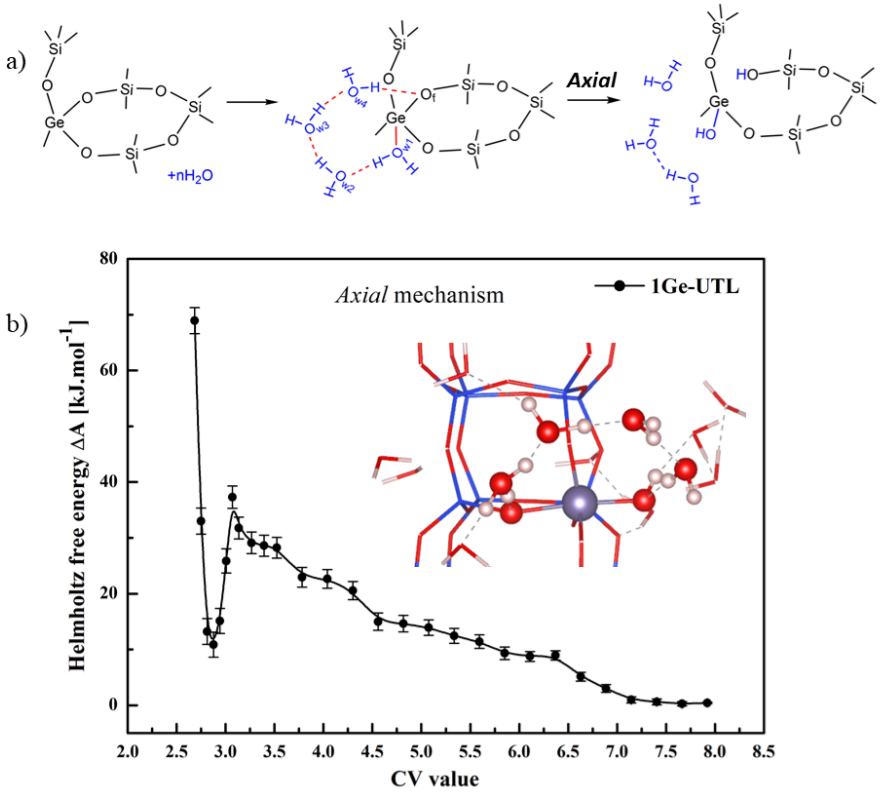

Figure 3.7: a) The scheme of the *axial* mechanism. b) The reaction profiles for the initial Ge-O bond hydrolysis via the *axial* mechanism at high water loading. The structure close to transition state depicting the proton-shuffling water chain is also inserted in the figure.

To shed light on the seemingly larger lability of framework oxygen in *axial* position to incoming water in comparison to oxygens in *equatorial* positions, we carried out multiple analyses of the five-coordinated Ge center, namely the bond-length analysis, Mulliken population analysis, electrostatic potential map evaluation and evaluation of the projected density of states (see Figure 3.8 and Table 3.2). These analyses clearly show that framework oxygen in *axial* position O_{ax} should be more reactive than *equatorial* oxygen O_{eq} as exemplified by: i) O_{ax} being more nucleophilic than *equatorial* O_{eq}, ii) the Ge-O_{ax} being on average longer than Ge-O_{eq}, and iii) that the top of the valence band is occupied primarily by electron density at O_{ax}. In summary, increasing water loading in UTL channels opens a new hydrolysis path, the *axial* mechanism, that significantly decreases (by two thirds) the activation barrier for the first Ge-O hydrolysis step compared to the low water loading case.

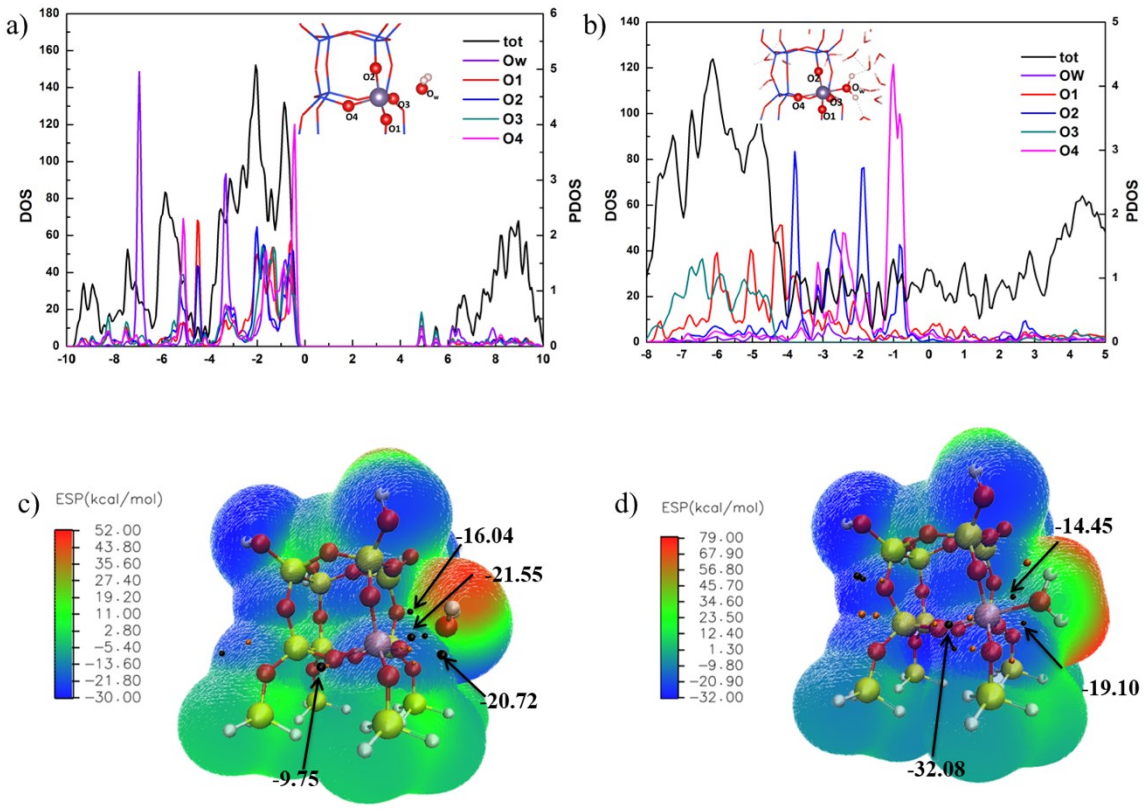

Figure 3.8: a) and c) The partial density of states and electrostatic potential map for water-adsorption complex in the 1Ge-UTL model with a single H_2O/UC (a static DFT-optimized structure). b) and d) The partial density of states and electrostatic potential map for the water-adsorption complex in the 1Ge-UTL model with 18 H_2O/UC (a snapshot from the AIMD simulation).

Table 3.2: Mulliken charges and Ge-O bond lengths for water-adsorption complexes in the 1Ge-UTL model (see Figure 3.8a-b for notation).

	DFT-optimized structure	**A snapshot from AIMD with 5-coordinated Ge center**
Mulliken charge [eV]		
Ow	-0.94	-0.87
O1	-1.07	-1.04
O2	-1.07	-1.07
O3	-1.08	-1.04
O4	-1.09	-1.07
Ge-O bond length [Å]		
Ge-Ow	2.440	1.956
Ge-O1	1.776	1.835
Ge-O2	1.780	1.770
Ge-O3	1.785	1.803
Ge-O4	1.803	1.902

3.1.4 High water and high Ge conditions

In the high Ge content conditions, we again considered nGe-UTL (n = 2, 3, 4, 8) models with germanium concentrated in the D4R unit. Initially, we performed at least 20 ps equilibrium AIMD simulation for all high Ge models at high water loading. For 2Ge-UTL and 3Ge-UTL models, the affinity of water molecules for germanium atoms is improved and water molecule can spontaneously adsorb on germanium atom after a few ps of AIMD simulation. This leads to formation of the five-coordinated Ge centers as described above. Once this five-coordination Ge structure is formed, it survives throughout the whole subsequent AIMD run (more than 15 ps) as illustrated in the Figures 3.9a and 3.9c, that trace the Ge-O_w distances for 2Ge- and 3Ge-UTL models. In addition, the adsorbed water molecule will intermittently deprotonate during the AIMD run, forming short-lived Ge-OH group and H_3O^+ complex

nearby, *i.e.*, another precursor of *axial* mechanism described above is formed (see Figures 3.9 b and d).

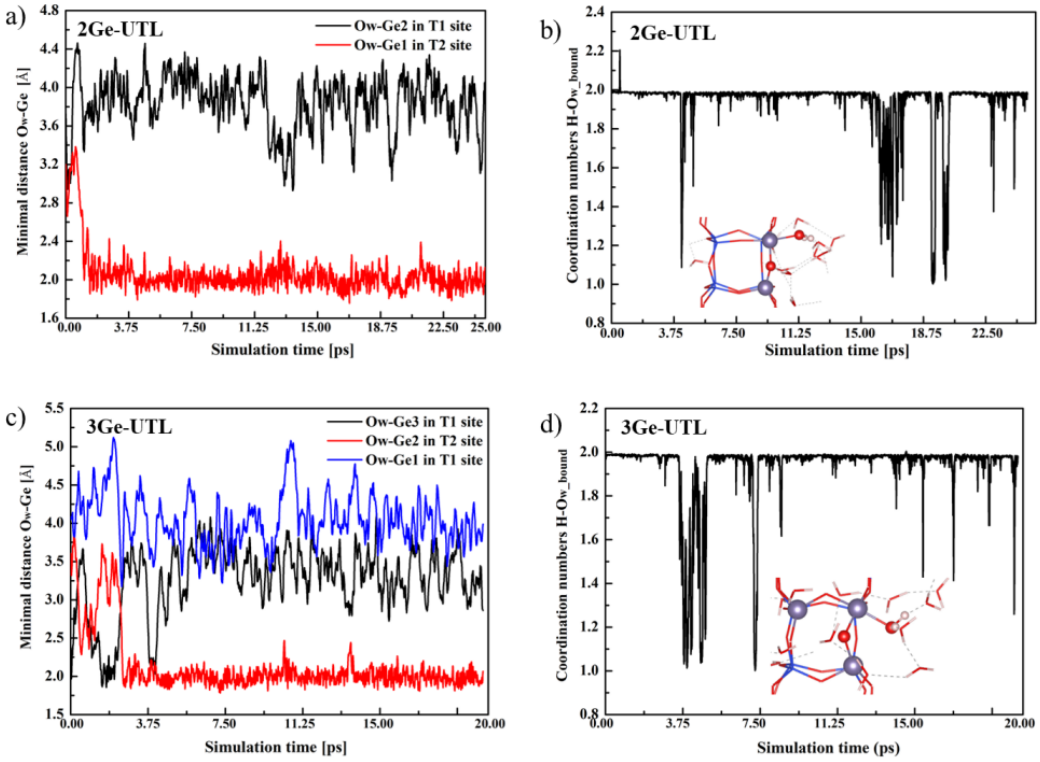

Figure 3.9: a) and c) The minimum distance time evolution between the all oxygen atoms in the water solvent and all the Ge atoms during the equilibrium AIMD simulations for 2Ge-UTL and 3Ge-UTL, respectively. b) and d) The coordination number of the oxygen atom from adsorbed water molecule with all hydrogen atoms in the unit cell for 2Ge-UTL and 3Ge-UTL, respectively. The representative structures of the five-coordinated Ge centers are also inserted into the figures.

For 4Ge-UTL and 8Ge-UTL models, the D4R unit's reactivity increases dramatically following a *geminal*-like mechanism[59, 121], termed *S2R* mechanism (see Figure 3.12) since it involves formation of Ge-$(O)_2$-Ge species (see Section 3.1.2). For the 4Ge- and 8Ge-UTL models, almost immediately after the AIMD start, the water inserts itself into the Ge-O_f-Ge unit (see Figure 3.10a and c), it loses a proton and pushes the framework oxygen O_f (of Ge-O_f-Ge unit) inside the D4R unit. After few ps, the newly formed Ge-$(O_f)(O_wH_w)$-Ge unit gets deprotonated further forming the Ge-$(O_f)(O_w)$-Ge unit, with both protons from the incipient water now solvated in the channel, significantly acidifying the solution nearby. However, one

of the protons tends to intermittently reattach to Ge-(O_f)(O_w)-Ge unit. Interestingly, the framework oxygen O_f inside the D4R is not firmly attached to the incipient Ge-(O_f)(O_w)-Ge unit but is mobile and can hop between the Ge-O-Ge units in the D4R (see Figure 3.10d which, *e.g.*, shows the *S2R* product being composed of Ge2-(O_{inside})(O_w)-Ge3 unit during the first 1-12 ps of AIMD, and shifting to Ge7-(O_{inside})(O_w)-Ge8 *S2R*-like product at 35-40 ps of the AIMD). Such migration is more frequent in the 8Ge-UTL model compared to the 4Ge-UTL model (compare Figures 3.10b and 3.10d). Presence of such species occupying the inside of the D4R unit is reminiscent of well-known case of F^- anions observed in D4R units after the zeolite synthesis in hydrofluoric acid[129-131].

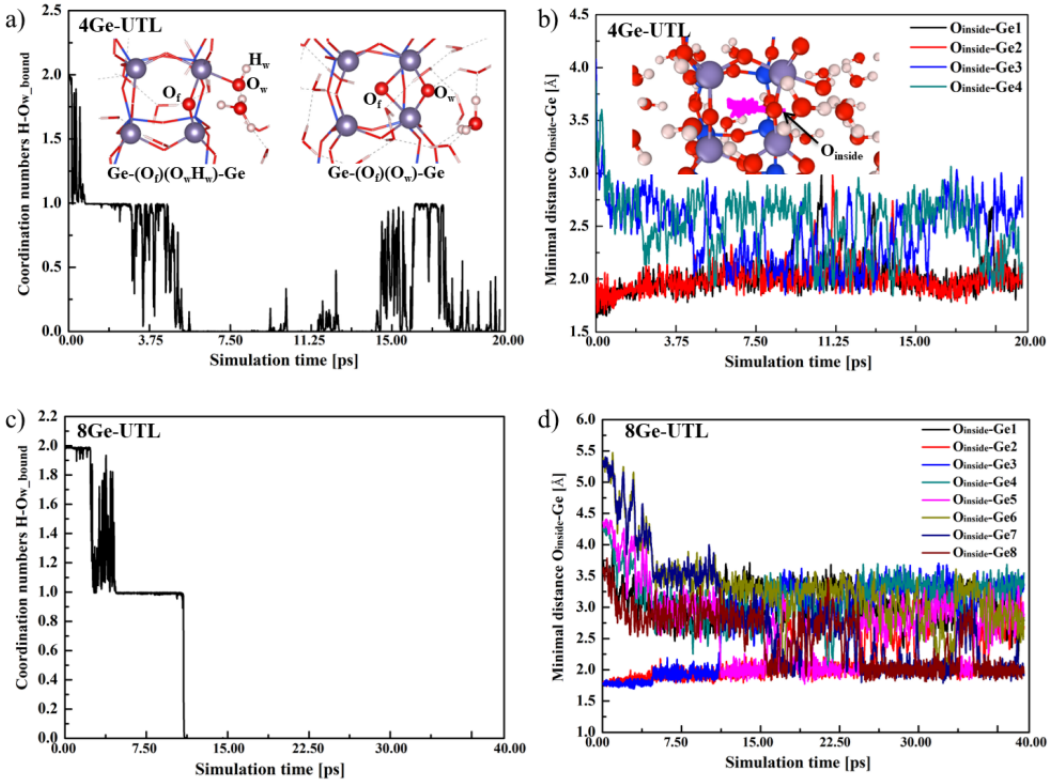

Figure 3.10: a) and c) The coordination number of the oxygen atom from the adsorbed water molecule with all hydrogen atoms in the unit cell for 4Ge-UTL and 8Ge-UTL models, respectively. For 4Ge-UTL model, the representative structures depicting deprotonation steps are shown in the inset. b) and d) The minimal distance between oxygen atoms inside the D4R unit and all Ge atoms in D4R unit for 4Ge-UTL and 8Ge-UTL, respectively. The structure inserted in b) shows the trajectory line (in pink) of the O_{inside} during the AIMD simulation.

Lastly, we also considered alternative distribution of germaniums in 4Ge-UTL model (Figure 3.11), putting all germaniums in the S4R ring parallel with the layer rather than in the S4R ring perpendicular to the layer, with motivation being that the hydrolysis of S4R ring parallel to the layer is expected to allow layer delamination1. We observed that these two 4Ge-UTL models behave qualitatively the same and hence the orientation of the germanium-filled S4R ring in D4R unit is not expected to play a big role in hydrolytic reactivity.

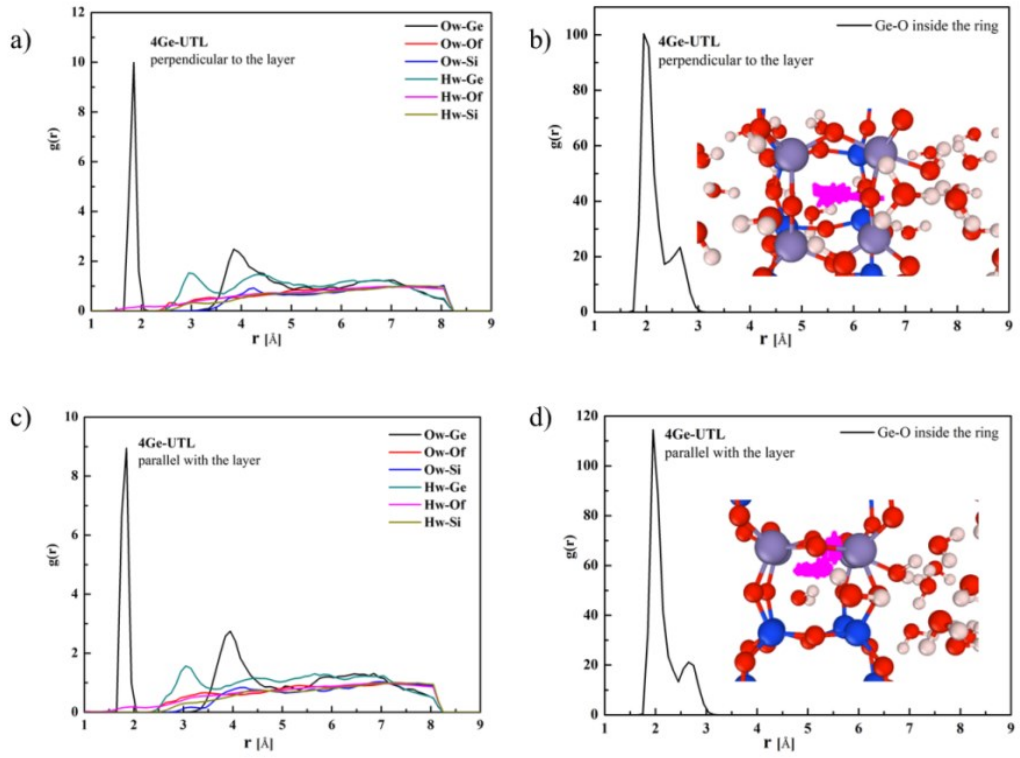

Figure 3.11: The partial radial distribution functions for the water-filled 4Ge-UTL models with different orientation of the Ge-filled S4Rs. a) and b) the results for S4R occupied by Ge being perpendicular to the layer, c) and d) are the results for S4R occupied by Ge being parallel with the layer. The structures inserted in b) and d) show the trajectory lines (in pink) of the O_{inside} during the AIMD simulation.

To quantitatively understand the energetical preference for the *S2R* mechanism in the high Ge conditions, we calculated the free energy profiles of *S2R* reaction for all high Ge models through thermodynamic integration of constrained ab initio molecular dynamics simulations. All free energy barriers and local minimum values are summarized in the Figure 3.12b. The results show that the reaction barriers are lower than 15 kJ mol^{-1} for all models, and that the

energy barrier decreases further as the Ge content increases. The main difference between lower (2Ge- and 3Ge-UTL) and higher Ge (4Ge- and 8Ge-UTL) models is in a stability of the *S2R* products; reactions are very exergonic for models with high Ge content (ΔA_{rxn} < -30 kJ mol^{-1}), while almost free energy neutral for models with low Ge content (ΔA_{rxn} = 0 ± 10 kJ mol^{-1}). Hence, with enough germanium in the D4R unit, the *S2R* step is able to provide a lot of excess energy to the system (between 30-50 kJ mol^{-1}), which could be used for further reactive transformations, such as hydrolysis of Ge-O bonds, *e.g.*, using *axial* and *equatorial* mechanisms discussed above (see Sections 3.1.1-2). All this indicates that with enough germanium clustered in S4Rs, one should expect the UTL framework to become much less hydrolytically stable, with the water solution inside the zeolite channels becoming extremely acidic (with two protons solvated in 17 waters, *i.e.*, pH ~ -1). This phenomenon may help explain that the use of strong acid in Ge-rich zeolites can remove germanium without destroying the crystalline structure[132].

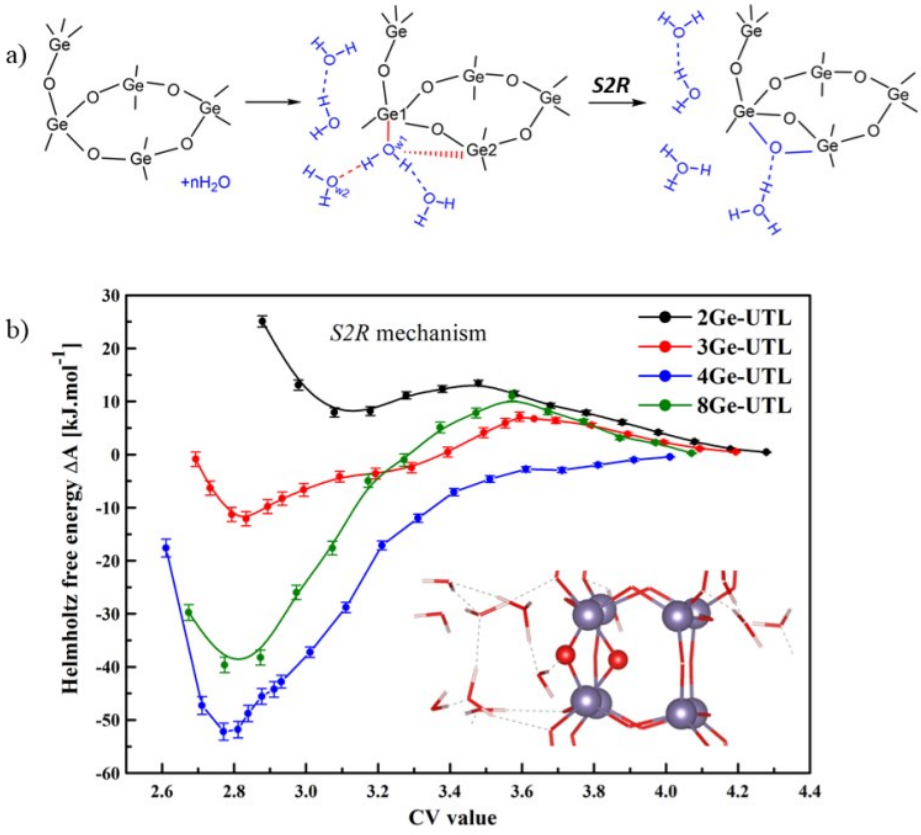

Figure 3.12: a) The scheme of the *S2R* mechanism. b) The free energy profiles for the *S2R* mechanism in the multiple nGe-UTL models (n = 2, 3, 4, 8) at high water loading conditions. The representative structure of the *S2R* product for the 8Ge-UTL model is showed in the inset.

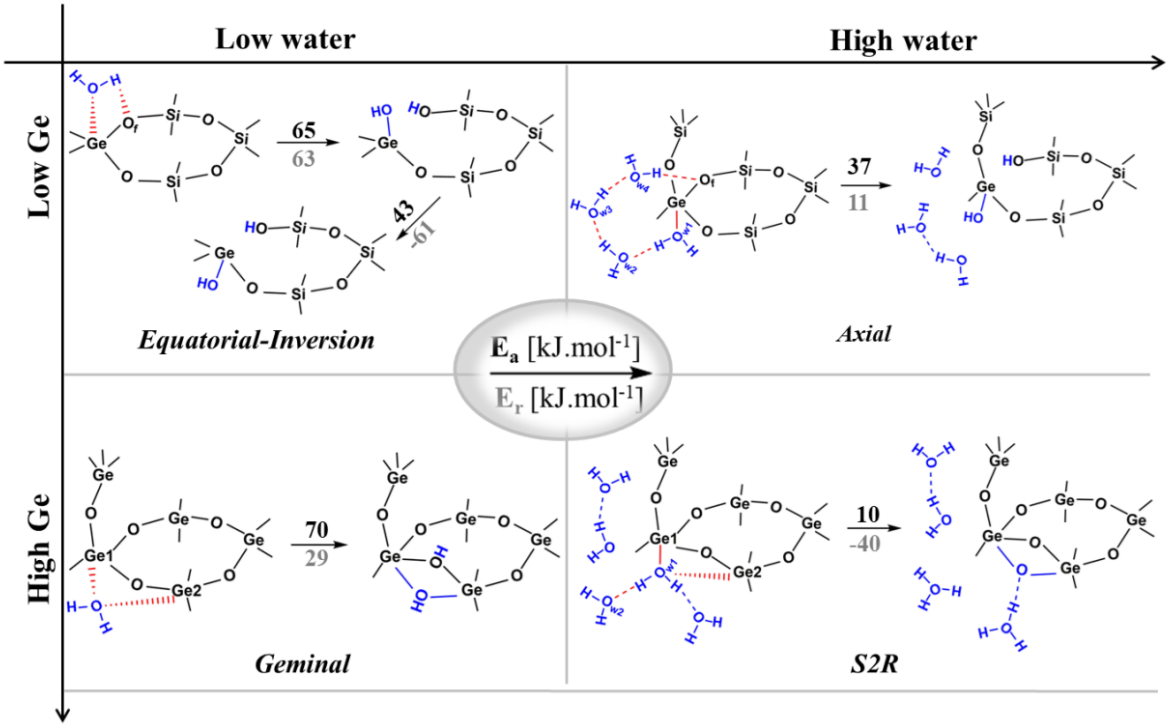

Figure 3.13: The summary diagram for all the hydrolysis mechanisms discussed in this section as a function of water loading and germanium content. The representative reaction barriers and reaction energies corresponding to each mechanism are marked above and below the arrows, respectively.

3.1.5 Summary

We studied the hydrolysis process for Ge-substituted zeolite UTL (Ge-UTL) with different Si/Ge ratios and water loading. Different water and germanium content will cause the hydrolysis of the Ge-O bond to proceed according to completely different mechanisms. The Figure 3.13 summarizes the discovered mechanisms corresponding to different reaction conditions. Both in low- and high-water loading conditions, increasing the concentration of germanium atoms can reduce the barrier of Ge-O bond scission. In the low Ge model with sufficient water molecules, the energetically favorable *axial* mechanism proceeds via Grotthuss-type proton shuttling, and a stable *axial* product can be formed with a very low barrier. In the high Ge models, germanium clustering opens a new extremely favorable (in terms of very low reaction barriers and large exergonicity of the reactions) *S2R* reaction pathway, that can energize further decomposition of the germanosilicates as observed in the experiments[1-6]. Lastly, we identified the existence of a critical germanium content at about 3-4

Ge/UC (clustered in D4R unit) that abruptly changes the hydrolysis dynamics and which we relate to the increased favorability of the *S2R* mechanism at and beyond this critical germanium content.

3.2 Hydrolysis of siliceous zeolite CHA under alkaline conditions[133]

3.2.1 Non-catalytic hydrolysis with pure water

We investigated first the siloxane (Si-O-Si) bond hydrolysis of purely silicious CHA zeolite under neutral conditions with minimal water content (one water per CHA unit cell) assuming it proceeds via the previously discussed *equatorial(-inversion)* mechanism[66-67, 69-70] (see section 3.1.1 for more details on the mechanism). Within this section, we denote it as the *M1* mechanism (Figure 3.14a). We calculated the complete desilication pathway of a Si site starting from the pristine CHA framework with the results summarized in the Figure 3.14b. We considered scission of all four inequivalent Si-O bonds, however in Figure 3.14b, only the most favorable desilication pathway is depicted. We reiterate (see also section 2.1.1) that water molecule adsorbs weakly in the pristine purely siliceous CHA with the water adsorption energy reaching only -28 kJ mol^{-1} with the minimal distance between O_w-Si being as much as 3.41 Å. The reaction barrier of the initial $Q^4 \rightarrow Q^3$ hydrolysis step via *equatorial* mechanism is 147 kJ mol^{-1}, and the *equatorial* product is unstable with high reaction energy 145 kJ mol^{-1}. Then the *inversion* step occurs, with an intrinsic barrier 53 kJ mol^{-1} can forming the more stable *axial* disilanol product. The first step of hydrolysis following the *equatorial-inversion* mechanism is thus endothermic (E_r = 29 kJ mol^{-1}) with the effective barrier of 198 kJ mol^{-1}, which is consistent with the high stability of the high silica zeolite under neutral conditions.

We then considered the further hydrolysis process assuming *equatorial* mechanism in each step until the full removal of an $Si(OH)_4$ group from the framework, *i.e.*, going from Q^3Si to Q^0Si. Each step of the hydrolysis is accompanied by the adsorption of an additional water molecule with the water molecule splitting and breaking one of the remaining Si-O bonds in each step. Note, that the Si-OH groups formed by partial hydrolysis significantly increase the hydrophilicity of the CHA framework as documented by the approx. twofold increase (E_{ads} in the range between -54 and -67 kJ mol^{-1}) in water adsorption energies for partially hydrolyzed CHA (Figure 3.14b) compared to pristine CHA. The reaction barriers for the $Q^3 \rightarrow Q^2$, $Q^2 \rightarrow Q^1$ and $Q^1 \rightarrow Q^0$ hydrolysis steps are 152 kJ mol^{-1}, 132 kJ mol^{-1} and 110 kJ mol^{-1} (Figure 3.14b), respectively. The barriers for further steps are thus all lower than the reaction barriers of the $Q^4 \rightarrow Q^3$ step, indicating that the first step hydrolysis is the rate-limiting step.

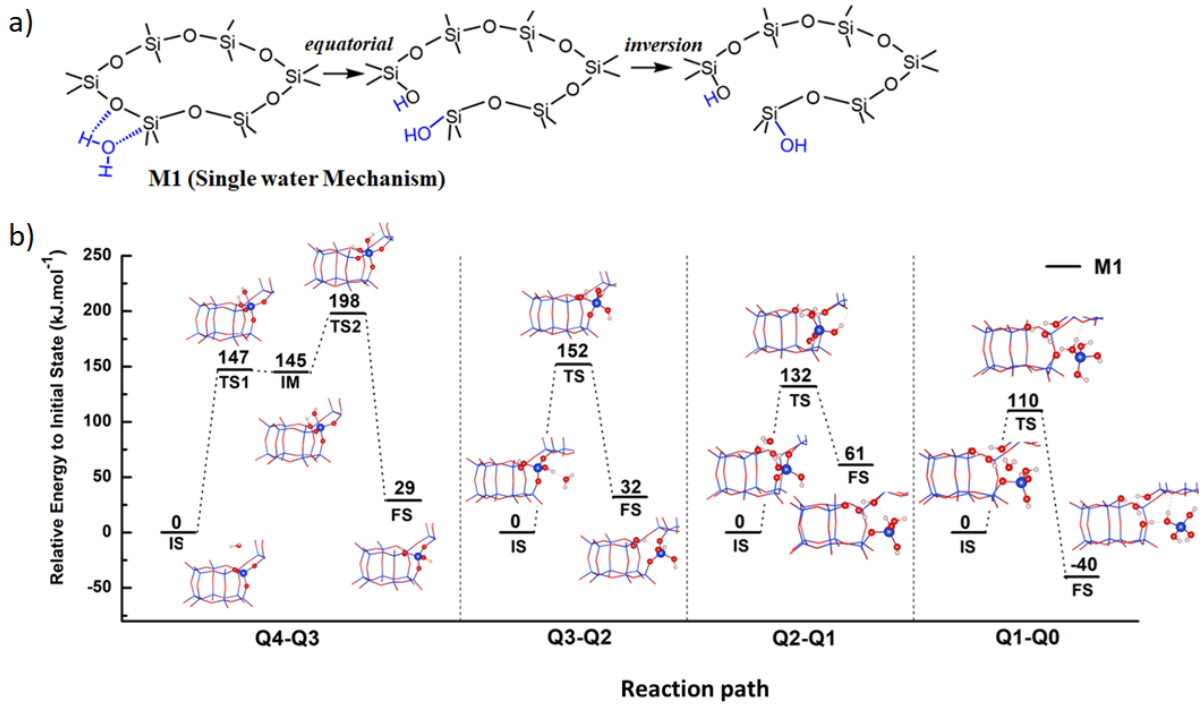

Figure 3.14: a) The scheme of the *equatorial(-inversion)* (*M1*) mechanism. b) The reaction profile for the complete hydrolysis process from Q^4Si to Q^0Si. The energy of the most stable structure with the adsorbed water at each step is taken as the initial state with its energy set to 0 kJ mol^{-1}.

The final hydrolysis product includes silanol nest and an external-framework $Si(OH)_4$ complex as shown in Figure 3.15a. Out of interest, we have examined different silanol nest arrangements after removal of an external-framework $Si(OH)_4$ complex, and found that the most stable configuration of a silanol nest is the ideal four-membered hydroxyl ring in which each silanol group acts both as a hydrogen bond donor and acceptor (Figure 3.15b) with hydrogen bond length varying from 1.56 Å to 1.78 Å. Previous studies have shown that the optimal hydroxyl nest arrangement for zeolite SOD is a three-membered hydroxyl ring and one dangling Si-OH group[134]. We also considered such a conformation in CHA but found it not to represent a local minimum in CHA. Rather, a three-membered ring conformation was located (Figure 3.15c) in which the fourth hydroxyl donates a hydrogen bond to the three-ring, but this structure is less stable than the four-ring configuration by 21 kJ mol^{-1}.

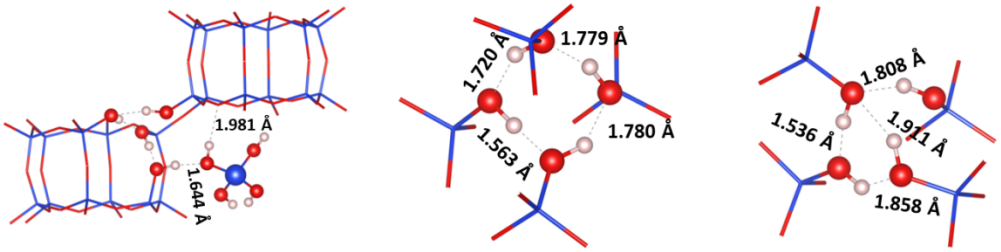

Figure 3.15: a) The silanol nest product with the extra-framework $Si(OH)_4$ bound to it. b) The most stable empty silanol nest configuration with four-membered hydroxyl ring. c) The alternative empty silanol nest configuration with three-membered hydroxyl ring.

3.2.2 Non-catalytic hydrolysis with NaOH

In the next step, we investigated the siloxane bond scission under purely alkaline conditions, NaOH acting as a reagent directly breaking the Si-O-Si bond. The strong NaOH interaction with CHA can lead to two distinct initial states with NaOH being either dissociated or non-dissociated. The hydrolysis mechanism that initiates from the non-dissociated NaOH is termed as *M2* and the mechanism that initiates from the dissociated NaOH is termed *M2** (see Figure 3.16).

The non-dissociated NaOH is strongly chemisorbed on the framework (adsorption energy as high as -202 kJ mol^{-1}) with the Na atom occupying the face of the 6-membered ring and coordinating with several oxygen atoms in the 6-ring, while the -OH group being bound to the Si atom. The Mulliken charge analysis shows that the -OH group donated about 0.3 electrons to the Si atom. In addition, the interaction with the framework stretches the Na-OH bond length from 1.99 Å (in vacuum) to 2.23 Å, and the framework Si-O bond *axial* to the newly formed Si-OH bond is also stretched from 1.63 Å (in pristine CHA) to 1.73 Å. The *M2* mechanism (Figure 3.16b) start with Na-OH bond scission followed by the -OH group driven inversion of the Si tetrahedron generating a Q^3 inverted silanol group and a Q^3 silanolate anion, which is bound to the Na cation. The activation barrier for this reaction is 59 kJ mol^{-1} and the reaction energy is 27 kJ mol^{-1}. Hence, the first step of the *M2* hydrolysis pathway leads directly to rather stable *axial* Q^3Si product without a need for intermediate *inversion*

step as in the pure water (*M1*) case and the reaction barrier is significantly lower than for the *M1* case.

For the *M2** mechanism, the initial state is the CHA framework with the dissociated NaOH bound to it (see Figure 3.16b). The -OH anion is bound to the Si atom in the *axial* position to the Na cation, which is being coordinated to oxygens in the 6-ring. The dissociated state is higher in energy than the nondissociated state, by 26 kJ mol^{-1}. However, it is found to activate the $Q^4 \rightarrow Q^3$ siloxane scission, resulting in the same product as the nondissociative route, with an intrinsic barrier lower by 11 kJ mol^{-1} (see Figure 3.16a).

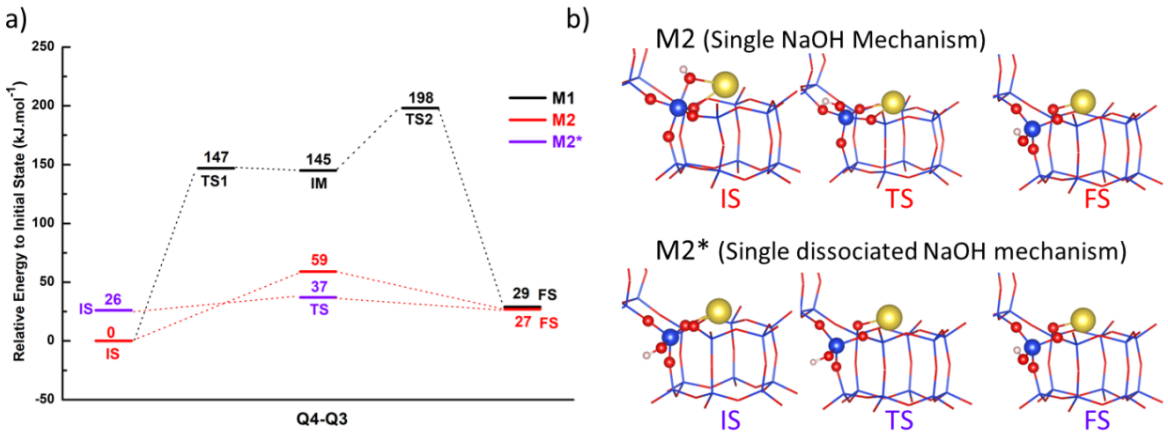

Figure 3.16: a) The reaction profile for the initial $Q^4 \rightarrow Q^3$ hydrolysis step via *M1*, *M2* and *M2** mechanisms. b) The structures illustrating the *M2* and *M2** mechanisms.

The subsequent *M2* reaction steps ($Q^3 \rightarrow Q^0$) follow the similar mechanism as the first step with an additional NaOH added in each step, with the results for this process being summarized in Figure 3.17. The intrinsic barrier for the $Q^3 \rightarrow Q^2$, $Q^2 \rightarrow Q^1$, and $Q^1 \rightarrow Q^0$ steps (33, 57, and 14 kJ mol^{-1}) are similar or lower than for the first step and significantly lower than for the *M1* mechanism in pure water. Also, all the subsequent steps are extremely exothermic. These results (low barriers and large exothermicity) are in agreement with the previous work[71] for $Q^3 \rightarrow Q^0$ desilication in purely alkaline conditions for MFI surface model. However, the *M2* mechanism consumes large quantities of NaOH as it takes four NaOH to remove one Si atom from the framework, and it results in a formation of bulky Si vacancy defect site with many sodium silanolate groups in close proximity (see Q^0 structure on the right of Figure 3.17b).

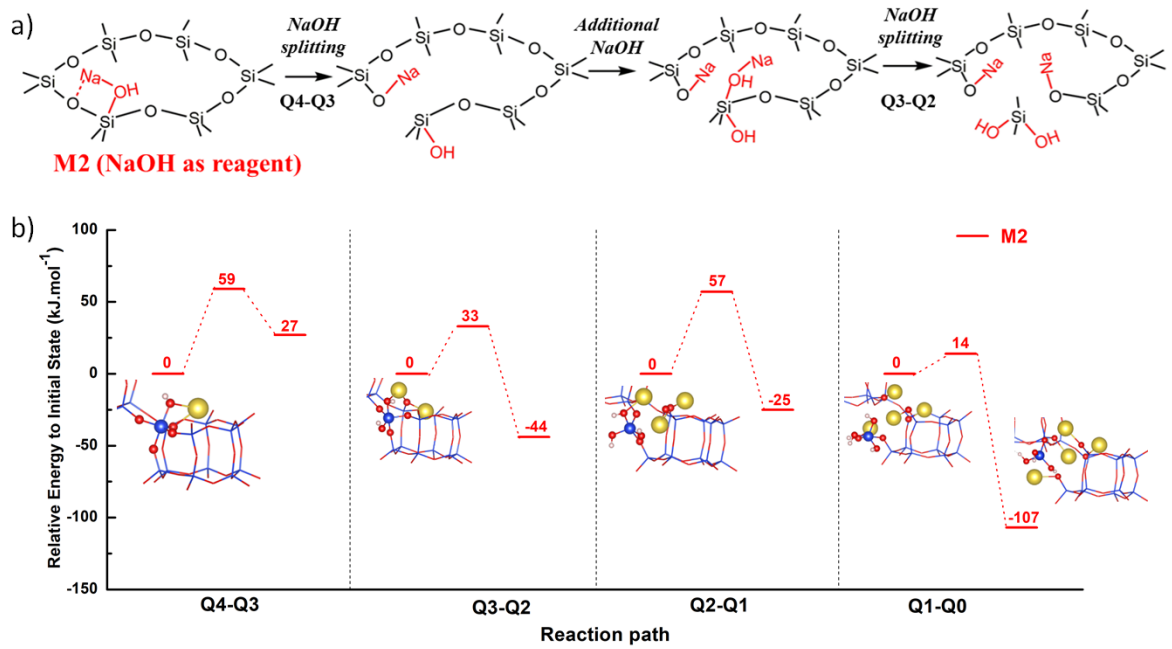

Figure 3.17: a) The scheme of the *M2* mechanism. b) The reaction profile for the complete desilication following the *M2* mechanism from Q^4Si to Q^0Si.

We also considered an alternative hydrolysis mechanism in which Na cation acts as spectator after the first $Q^4 \rightarrow Q^3$ *M2* step (Figure 3.18). Such a mechanism does not change the intrinsic reaction steps involved, but introduces spectator ions which may affect the energetics of the reaction. We test this mechanism starting from the more favourable product of the $Q^4 \rightarrow Q^3$ step that is reached via direct reaction by NaOH (*M2* mechanism). An additional water molecule is introduced, which binds preferentially to the Na cation. Framework hydrolysis is found to occur in two stages. First, a relatively facile migration of the water molecule occurs, from the Na ion to the Q^3 $Si(OSi)_3(OH)$ site, with an intrinsic barrier of 54 kJ mol^{-1}. This is followed by the water splitting *equatorial* mechanism, leading to the Q^2Si product. The *equatorial* step has a high intrinsic barrier of 183 kJ mol^{-1}, which is similar to the activation energy of water splitting in the absence of NaOH (*M1* mechanism). The effective barrier from water adsorption to the Q^2Si product is 218 kJ mol^{-1}. Hence, the *equatorial* mechanism is not helped by the presence of a nearby sodium cation. Sodium merely provides a stable adsorption site for additional water, which introduces an additional migration barrier prior to hydrolysis. Therefore, alternating water and NaOH driven steps do not benefit from any synergy and are limited by the high barriers for *equatorial* water splitting, as is the case for mechanism *M1*.

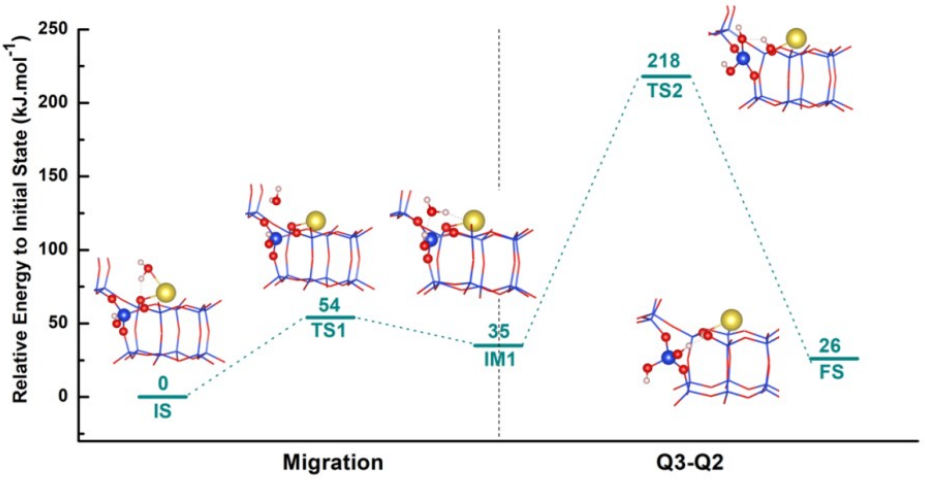

Figure 3.18: The reaction profile for the $Q^3 \rightarrow Q^2$ hydrolysis step via "Na as spectator" mechanism, the corresponding structures are inserted into the figure.

Effect of microsolvation conditions

The presence of additional water molecules in the vicinity of the reactive centre is possible, given that under experimental conditions water is both the carrier of NaOH and is in excess[135-136]. However, the hydrophobicity of the zeolite interior suggests a saturation water density of far less than 1 g cm^{-3}. We model this situation via introduction of excess water molecules as a microsolvating environment in the pore. This water can affect the dissociation equilibrium of reactive NaOH, the stabilisation of hydrolysis intermediates, provide new collective hydrolysis mechanisms, or modify the propensity of Na cations towards clustering around defects. Therefore, we consider the implications on the energetics and mechanisms of hydrolysis upon inclusion of small amounts of excess water and modelled it using AIMD simulation accompanied by a subset of static calculations.

In reaction *M2*, we observed that non-dissociated NaOH is energetically preferred to dissociated NaOH (see Figure 3.16). To investigate the role of water loading on the NaOH dissociation equilibrium, molecular dynamics simulations were performed with varying degrees of microsolvation, corresponding to no water, one water molecule per unit cell and full water loading (corresponding to a water density of 1 g cm^{-3}). The results are summarized in Figure 3.19. In the absence of water, the simulations agree closely with static DFT calculations. Non-dissociated NaOH is 25 kJ mol^{-1} more stable than dissociated NaOH, and

the product of the hydrolysis reaction is endothermic by 21 kJ mol^{-1}. The inclusion of one water molecule slightly stabilises the dissociated initial state and the product state (+17 and +16 kJ mol^{-1}, respectively). This is due to the adsorption of water to the sodium atom, which weakens the Na-OH bond, and helps to satisfy the coordination of Na^{+} after hydrolysis. At high water loading, the energetics are dramatically shifted. The dissociated NaOH is preferred by 14 kJ mol^{-1}, and the hydrolysis reaction becomes exothermic (see Figure 3.19). Hence, microsolvation of NaOH allows for spontaneous access to the optimal hydrolysis mechanism, while simultaneously increasing the equilibrium constant of the forward reaction.

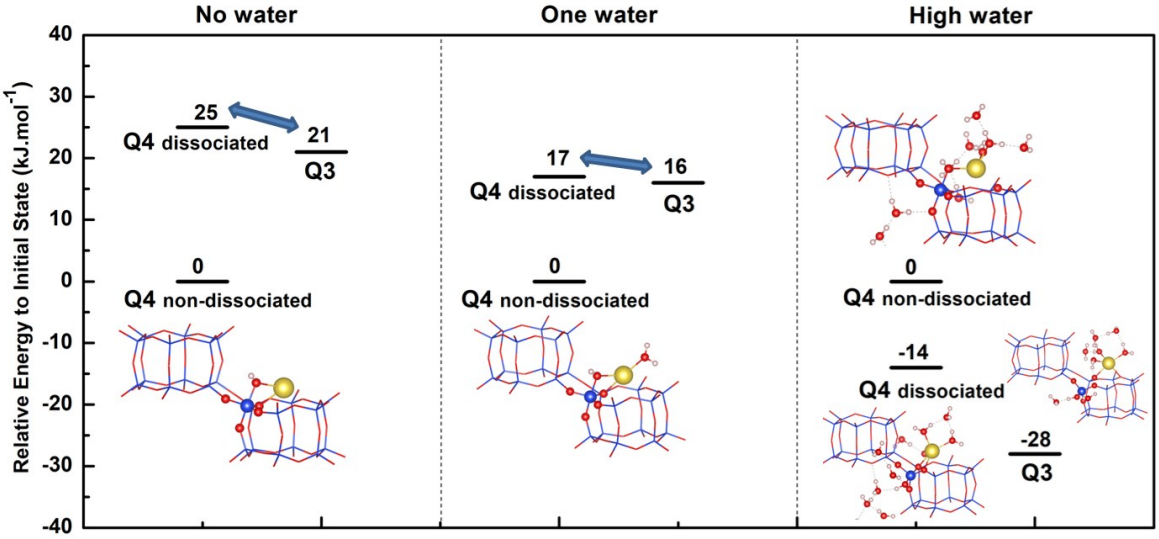

Figure 3.19: The water loading effect on the relative stability of dissociated and non-dissociated NaOH and Q^3Si product.

After the first hydrolysis step, the zeolite contains new water condensation sites: either two silanol hydroxyl groups, or a hydroxyl and a sodium silanolate. In order to determine the stabilisation afforded by water adsorption, we considered the binding of microsolvating water to the most favourable Q^3Si product as a function of water loading, from one to five molecules per defect. In all cases, inclusion of water molecules stabilises the products of hydrolysis, with respect to unincorporated water molecules (Table 3.3). This adsorption is stronger than that of water to the pristine zeolite (-28 kJ mol^{-1}), which is indicative of the increased hydrophilicity of the defective framework. It is notable that while increasing the water content decreases the binding energy per water molecule, it is a slow function of water

loading. This implies that several water molecules will adsorb to the Q^3 defect, provided sufficient molecules are present nearby and diffusion limitations are overcome.

Upon generation of hydrolysis defects, the increased hydrophilicity of the zeolite pore allows for a wide range of possible water cluster configurations. We observe that water preferentially adsorbs at the sodium silanolate, rather than the silanol, for all water loadings considered (Table 3.3). For the locally optimal configurations, a structural trend emerges. The most stable configuration for a given water loading always includes an interaction between O_w and Na, and an interaction between H_w and O_f at the silanolate. For n=1, the water molecule adopts a strained configuration which achieves both bonds, leading to a four-ring local minimum (Figure 3.20b). For n=2 and n=3, separate water molecules can bind to Na and to OSi. These molecules are connected by hydrogen bonds. For n=4, the additional water molecule binds O-down to Na. In this configuration, Na interacts with three O_f atoms and two O_w atoms, in a distorted trigonal prismatic configuration, and therefore the first interaction shell of Na^+ is complete. For n=5, the addition water does not interact with the sodium ion directly but contributes to the hydrogen bonding network between Na and the silanolate O_f. Hence, under microsolvation conditions, the silanol group will be exposed and the sodium maximally solvated.

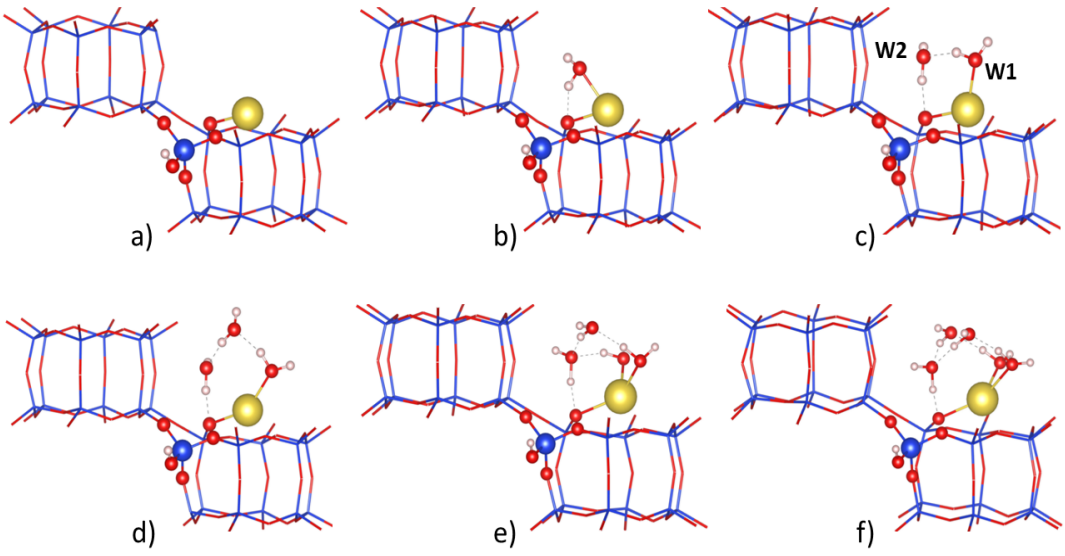

Figure 3.20: The optimal water adsorption configurations on the Q^3Si product with different amounts of water molecules n(H_2O) ($0 \leq n < 6$).

Table 3.3: Energetics of preferred water adsorption configurations at Q^3 $Si(OSi)_3OH$ and $Si(OSi)_3ONa$. E_{ads} (see section 2.1.6 equation 2.17) is given with respect to the Q^3Si structure and single H_2O gas phase molecule.

n(H_2O)	Number of H_2O at ONa:OH sites	E_{ads}/H_2O (kJ mol^{-1})
1	**1:0**	**-83**
	0:1	-54
2	**2:0**	**-65**
	1:1	-57
	0:2	-41
3	**3:0**	**-50**
	2:1	-44
	1:2	-39
	0:3	-35
4	**4:0**	**-38**
	3:1	-37
	0:4	-29
5	**5:0**	**-34**
	4:1	-31
	0:5	-24

These findings from static calculations are corroborated by AIMD simulations. First, water molecules are observed to organise around the Na^+ cation to form distinct solvation shells which are stable over the timescale of the AIMD simulation (20 ps). The configuration which is maintained throughout the simulation is one in which Na^+ forms two bonds to framework oxygen atoms, and approximately three bonds to water oxygen atoms (Figure 3.21b). Second, the interaction between Na^+ and the oxygen atom of the framework Q^3 silanolate (O_f) is stable, even in the presence of water molecules. The Na-O_f distance oscillates around an average value of 2.33 Å, without dissociation and solvation over the course of the simulation (Figure 3.21a).

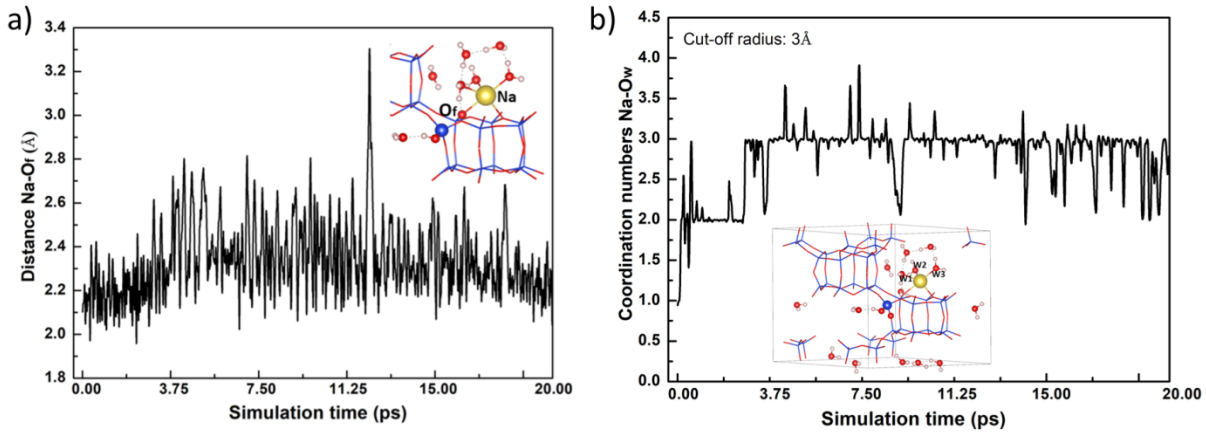

Figure 3.21: a) Distance trace for the Na-O_f bond over the AIMD simulation. b) The coordination number between Na^+ and 15 water oxygen atoms during the AIMD simulation, employing a cut-off distance of 3 Å for Na-O_w bonding, the snapshot structure at t = 7.5 ps of the Q^3 product state is inserted into b).

After the first NaOH-driven hydrolysis step, the possibility to introduce an additional NaOH molecule allows for two competitive processes to occur. The second NaOH molecule may bind to the defect, driving the second hydrolysis step via the *M2* reaction. Alternatively, it can bind to another region of the framework, causing another instance of the first hydrolysis step at another site, forming a new Q^3Si defect. Under anhydrous conditions, we observe that the clustering of NaOH at a single defect is preferred energetically by 19 kJ mol^{-1} (see Figures 3.22a-b). Hence, we should expect that desilication will be focused on a single defective site under alkaline anhydrous conditions. However, we found that the interaction between water molecules and the Na^+ cations is strong (see Table 3.3). To investigate the effect of solvation on the clustering propensity of NaOH, we simulated the two configurations under full water loading conditions via AIMD. Under such conditions, the energetic preference is reversed with respect to anhydrous conditions, with the isolated Q^3Si defects with a single NaOH each being 26 kJ mol^{-1} more stable than the clustered NaOH configuration at a single Q^3Si defect (see Figures 3.22c-d). This result implies that increasing water loading hinders subsequent steps of the *M2* mechanism at a Q^3Si defect, which involve a large degree of Na cation clustering (see Figure 3.17b).

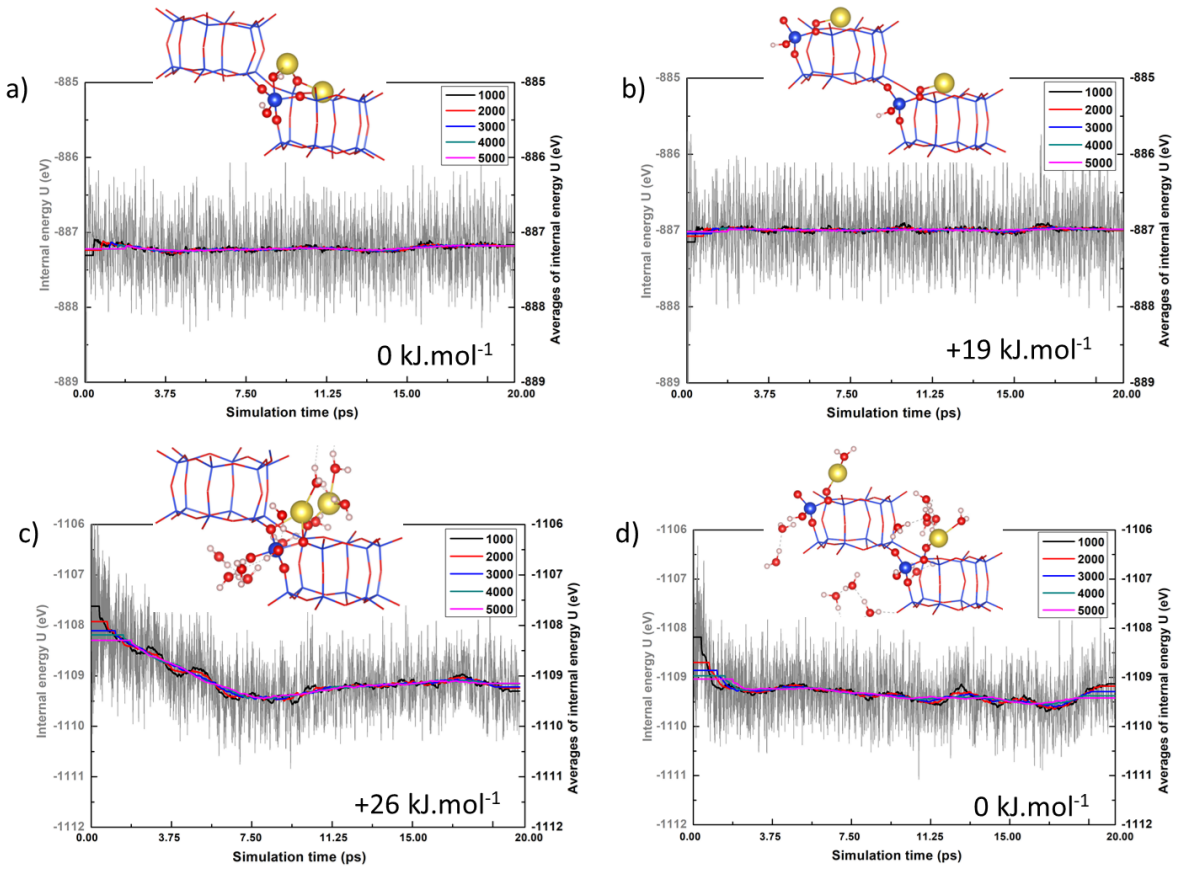

Figure 3.22: The AIMD energy trajectories with relative running averages for the structures of Q^3Si product with an additional NaOH, the breath of the sampling bins was varied from 1000 to 5000 snapshots per data point. a) and b) The clustered and non-clustered configurations in absence of water, respectively. c) and d) the clustered and non-clustered configurations under high water loading conditions, respectively.

3.2.3 Catalytic hydrolysis with minimal water

Instead of excessive consumption of NaOH via *M2* mechanism, NaOH may be instead regenerated by water after reacting with the framework, thereby catalytically driving hydrolysis. We term this mechanism the *M3* mechanism (see Figure 3.23a). In the *M3* mechanism, NaOH acts as a catalyst via direct hydrolysis of siloxane bonds, with regeneration of NaOH *in situ*, which is achieved by the decomposition of an additional water molecule. This mechanism avoids the need for consumption of multiple NaOH molecules. The regeneration of NaOH begins at the product of the NaOH-driven first step ($Q^4 \rightarrow Q^3$ step). A water molecule binds to the sodium ion, which is the most stable site for the water molecule (see Table 3.3 and Figure 3.20b). Then, a water splitting step transfers H_w to O_f, substituting

thus-formed NaOH for a hydroxyl (silanol) group ("IM1" system in Figure 3.23b). The NaOH molecule then migrates to the Q^3Si atom, binding O-down to form a penta-coordinated Si which is activated for hydrolysis (("IM2" in Figure 3.23b)). This regeneration step has an effective barrier of 104 kJ mol^{-1} under conditions of minimal water loading and is therefore feasible under moderate heating and low solvation conditions (Figure 3.23b). Further hydrolysis from Q^3Si to Q^2Si proceeds via a small intrinsic barrier (25 kJ mol^{-1}). A siloxane bond is broken and the Na-OH molecule dissociates, forming a Q^2 $Si(OSi)_2(OH)_2$ species and a Q^3 sodium silanolate species. In the *M3* mechanism, hydrolysis is enhanced with respect to *M1*, both by utilising the preferable NaOH-driven Q4→Q3 step and by the lower effective barrier for the Q3→Q2 step. It also avoids the requirement of high concentrations of incorporated NaOH molecules in the zeolite pores, that are inherent in mechanism *M2* (*M2**).

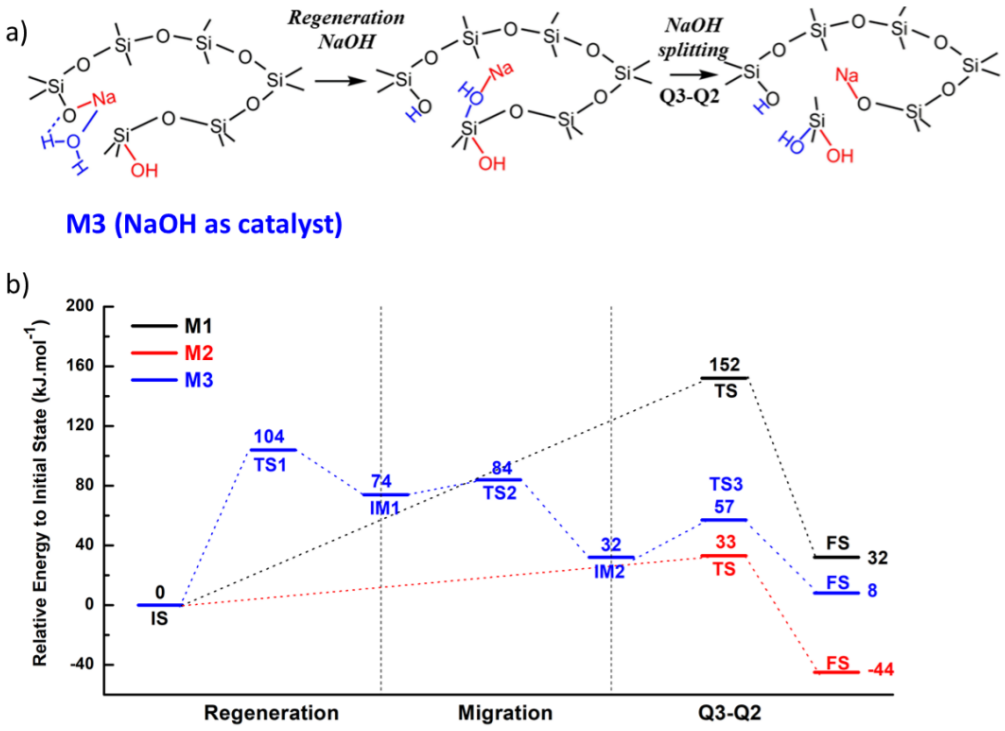

Figure 3.23: a) The scheme of the *M3* mechanism under minimal water conditions. b) The reaction profiles for the Q^3→Q^2 hydrolysis step via *M1*(black line), *M2* (red line), and *M3* (blue line) mechanisms, respectively.

Later steps along the *M3* pathway are similar and require one additional water molecule per step, which binds to Na, followed by catalyst regeneration, NaOH migration, formation of the

penta-coordinated silicon, and finally Si–O–Si scission (see Figure 3.24). The effective barriers for $Q^2 \rightarrow Q^1$ and $Q^1 \rightarrow Q^0$ steps are 94 and 110 kJ mol^{-1}, respectively. At each stage, the NaOH regeneration step has higher barrier than the Si-O bond scission step.

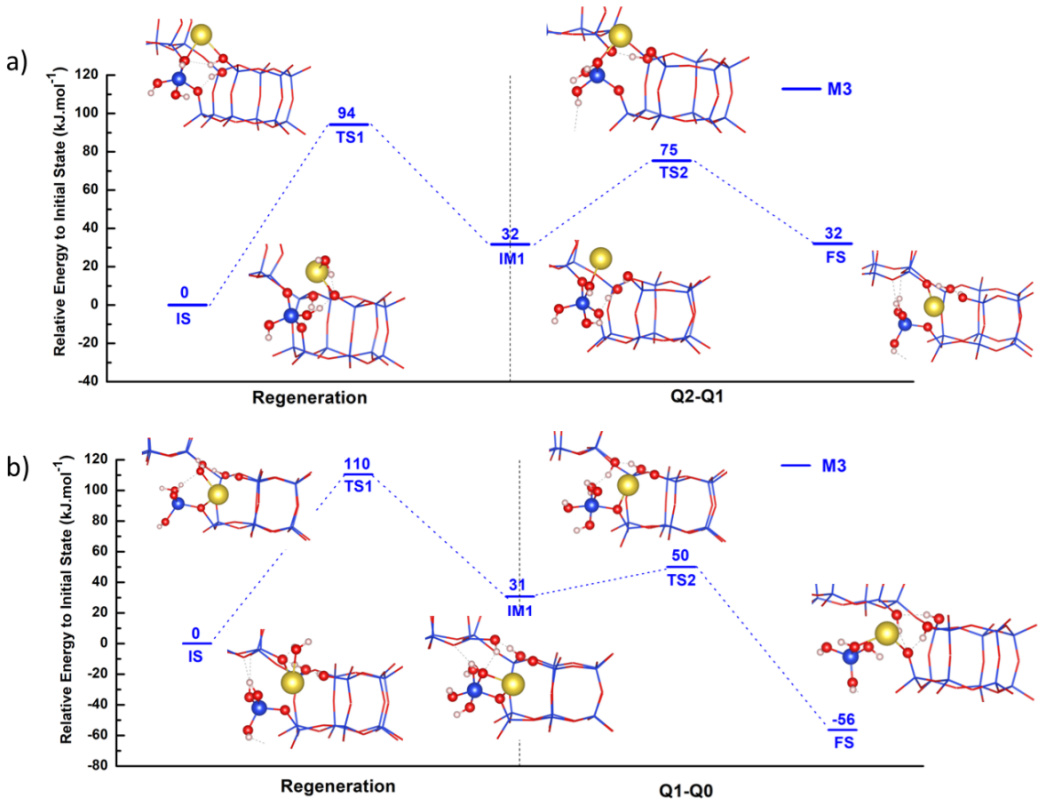

Figure 3.24: The reaction profile for the subsequent hydrolysis steps via *M3* mechanism under minimal water conditions: a) $Q^2 \rightarrow Q^1$, and b) $Q^1 \rightarrow Q^0$. The representative structures are inserted into the figure.

3.2.4 Catalytic hydrolysis with microsolvation

To test the role of microsolvating water in the catalytic mechanism (*M3*), we considered the effect of additional water on the regeneration and hydrolysis step between Q^3Si and Q^2Si. We added two water molecules to the reactive centre after the first hydrolysis step, rather than the single water molecule necessary to regenerate NaOH. The optimal initial structure is shown in Figure 3.20c, in which the first water molecule (W1) binds to Na via O_w, and the second molecule (W2) forms a hydrogen bonding complex in which it is a hydrogen acceptor from W1 and a hydrogen donor to the framework silanolate oxygen atom (O_f). The $Q^3 \rightarrow Q^2$

hydrolysis reaction proceeds via three elementary steps, denoted "water migration", "water splitting" and "siloxane scission" (see Figure 3.25).

In the water migration step, W2 replaces W1 as the proton donor to O_f, forming a strained structure similar to that found in Figure 3.20b under single water conditions. W1 migrates across the face of the 6-ring and rotates, becoming a hydrogen donor to O_w of W2. This step has a barrier of 35 kJ mol^{-1}. The water splitting step involves a concerted mechanism in which W1 splits, replacing Na with hydrogen on the silanolate group, which is equivalent to the catalyst regeneration step in *M3* under minimal water conditions. Concurrently, W2 transfers a proton to W1, which recovers the H_2O adsorbed to Na, and converts W2 into a hydroxyl group, which binds to Q^3Si. The product of this step is a penta-coordinated Q^3Si moiety, a silanol group and Na-OH_2, which is located near the siloxane bond that is to be broken. The intrinsic barrier is 64 kJ mol^{-1}, which is significantly lower than the analogous single water barrier (104 kJ mol^{-1} – see Figure 3.23) and is a result of the cooperative effect of the additional water molecule. The final step is the scission of a framework siloxane bond to form the Q^2Si product and a sodium silanolate group, with a barrier of 36 kJ mol^{-1}. This step does not benefit from any cooperative mechanism and therefore has similar barrier than the analogous single water step (25 kJ mol^{-1}).

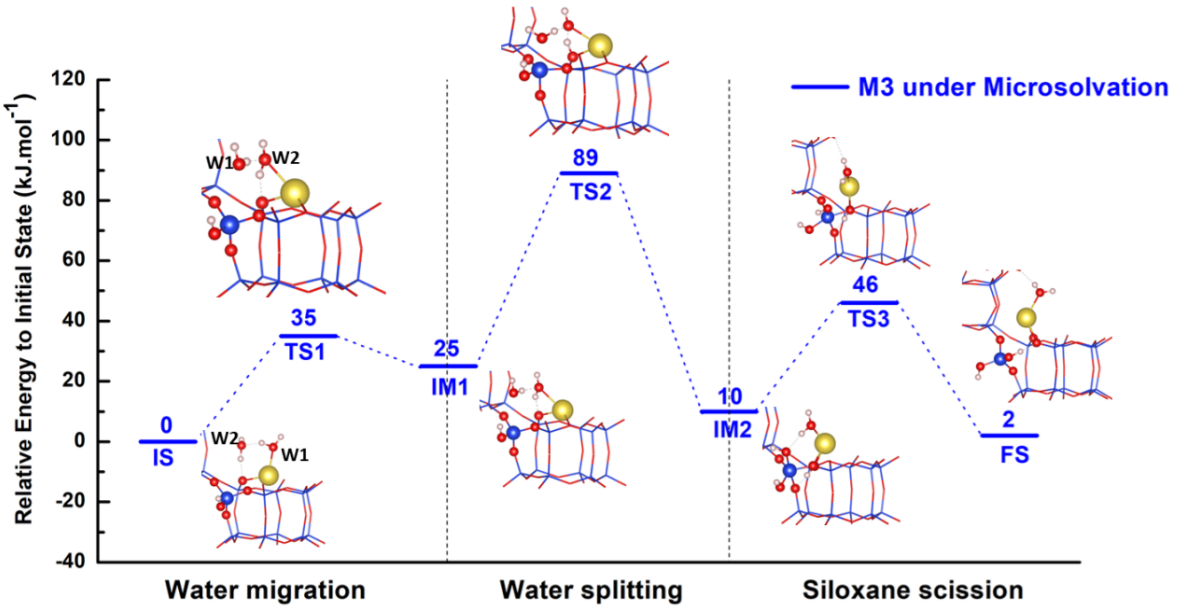

Figure 3.25: The reaction profile for the $Q^3 \rightarrow Q^2$ step via the *M3* mechanism under microsolvation conditions.

Subsequent steps, according to the *M3* mechanism under microsolvation showed similar trends (see Figure 3.26). The mechanism for each step involves water migration, water splitting, and siloxane scission and, for each step, it proceeds with significantly lower barriers than the minimal water *M3* mechanism. For $Q^2 \rightarrow Q^1$ step, the highest intrinsic barrier for catalyst regeneration is 65 kJ mol^{-1}, and it is 66 kJ mol^{-1} for the $Q^1 \rightarrow Q^0$ step. These highest barriers are for the water splitting step, which is also the most highly activated elementary step in the minimal water *M3* mechanism. This is also the elementary step that is enhanced most by the presence of additional water molecules in the reactive center.

We conclude that the inclusion of additional water provides the necessary environment to reduce the highest intrinsic barriers in NaOH-catalysed hydrolysis (*M3* mechanism), which belongs to catalyst regeneration steps. This is achieved through the establishment of a flexible hydrogen bonding environment which facilitates hydrogen transfer. The catalytic *M3* mechanism thus becomes even more competitive with the non-catalytic *M2* route under microsolvation conditions that is expected to be impeded by microsolvation (see Figure 3.22).

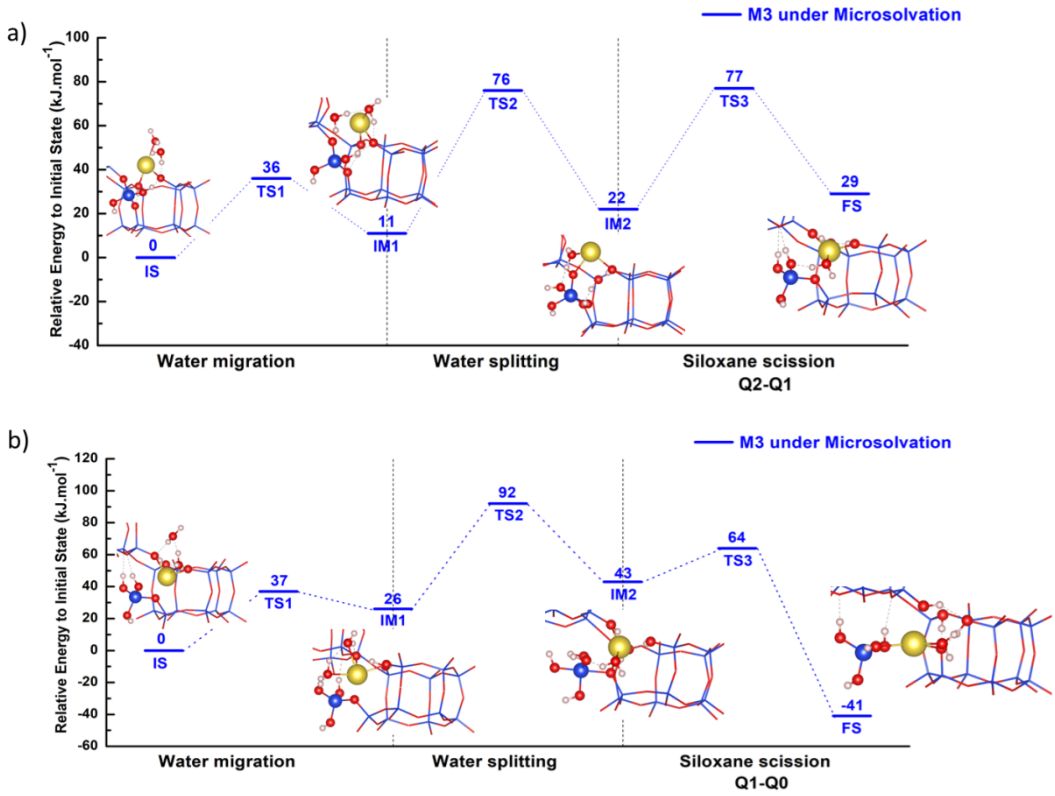

Figure 3.26: The reaction profile for the subsequent hydrolysis steps via *M3* mechanism under microsolvation conditions: a) $Q^2 \rightarrow Q^1$ and, b) $Q^1 \rightarrow Q^0$ steps, respectively.

3.2.5 Summary

The hydrolysis mechanisms of silicious zeolite CHA under neutral/alkaline conditions with various degrees of water loading have been systematically investigated. We found that the water and NaOH concentration play an important role for the kinetics and thermodynamics of the zeolite hydrolysis process. The NaOH greatly increases the rate of zeolite hydrolysis relative to neutral water, and we discovered that NaOH may not only act as a reactant but also as a catalyst. Both *M2* (“NaOH as a reactant") and *M3* (“NaOH as a catalyst") mechanisms are determined to be feasible under mild conditions, and which one is preferred in practice depends on the concentration of water and NaOH in the zeolite pores. The microsolvating water in the zeolite pores pores facilitates the first hydrolysis step of pristine silicious zeolite and decreases the barriers for NaOH regeneration by the hitherto unseen cooperative mechanisms.

3.3 Nature of framework-associated Al(Oh) under wet conditions

3.3.1 Structures and the formation path

The conversion of the regular framework tetrahedrally-coordinated Al(Td) species into framework-associated octahedrally-coordinated Al(Oh) species was investigated. The model of CHA zeolite with Si/Al=3 and six water molecules present in the cavity was adopted. The detailed reaction process shown in Figure 3.27a with the corresponding structures depicted in Figure 3.27b. The Al(Td)→Al(Oh) transformation consists of three steps, with each of the four minima on the free-energy surface has its distinct aluminum environment (see Figure 3.27b). The initial CHA structure, in which all Al atoms are four-coordinated to O_f in the tetrahedral environment, is used as reference state. This reference is labeled BAS(4). The transformation starts with the formation of the Lewis acid site LAS(4), which is nearly isoenergetic with BAS(4), overcoming a moderate barrier of $\Delta A \approx 40$ kJ mol^{-1}. The LAS(4) is formed together with the silanol on adjacent framework Si and the Al atom remains in a tetrahedral environment coordinated to three O_f atoms and one O_w atom. In a subsequent step, a penta-coordinated LAS(5) structure is formed when the second water molecule attaches to Al and the two previously solvated protons bind to two of the three remaining Al-O_f-Si bridges. The free energy barrier for this step is around 39 kJ mol^{-1} and the LAS(5) structure is slightly less stable than LAS(4) (by 11 kJ mol^{-1}). Finally, the transformation to octahedral aluminum, denoted also as LAS(6), is accomplished by accepting an additional water molecule into the first coordination shell of the Al atom. This process has a low free energy barrier (15 kJ mol^{-1}), and it is an exergonic process with the reaction energy of about -30 kJ mol^{-1}. All in all, there are four stable intermediate structures, as shown in Figure 3.27b, which are separated by modest free-energy barriers, which are less than 40 kJ mol^{-1} high each. This means that fast transitions between them are allowed even at the room temperature (RT). The octahedral LAS(6), which has a slightly lower free energy than the other intermediates, is thermodynamically the most stable configuration.

The Al in the framework-associated Al(Oh) is coordinated to three O_f and to three O_w in the *fac*-Al$(O_f)_3(H_2O)_3$ arrangement (see Figure 3.28a). Thus, the octahedral aluminum is formally a Lewis acid site – it coordinates three water molecules – and it is denoted as LAS(6). Such framework-associated Al(Oh) is formed from one of the aluminum atoms constituting the Al-O-Si-O-Al pair: one of the Al-O-Si bonds in the six-ring is hydrolyzed, thus forming a silanol (Figure 3.28b). None of the three original Brønsted protons in the CHA cavity is solvated

upon the formation of Al(Oh): two of them are firmly attached to O_f atoms of Al(Oh) and the third one is consumed in the silanol formation (vide infra). Thus, the Al(Td) → Al(Oh) conversion is associated with the loss of Brønsted acidity (three Brønsted protons are consumed).

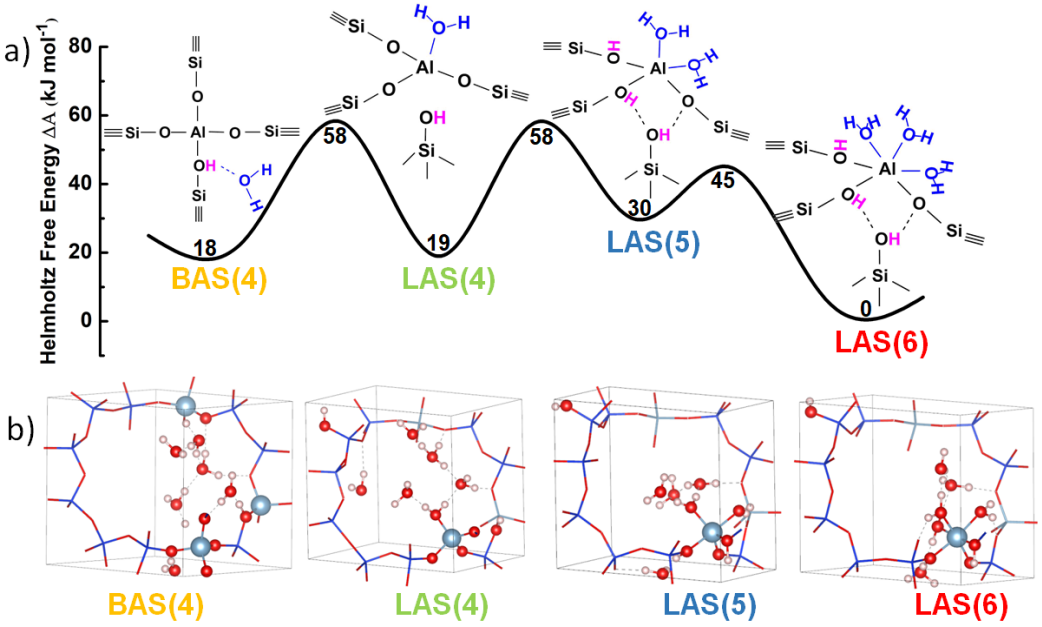

Figure 3.27: Structural and thermodynamic characteristics of tetrahedral and octahedral aluminum in CHA zeolite with Si/Al=3. a) Schematic free energy profile connecting Brønsted acid site (BAS) with Lewis acid sites LAS(n), where n denotes the number of oxygen atoms in the first coordination shell of the aluminum. b) The structure of the four stable intermediates.

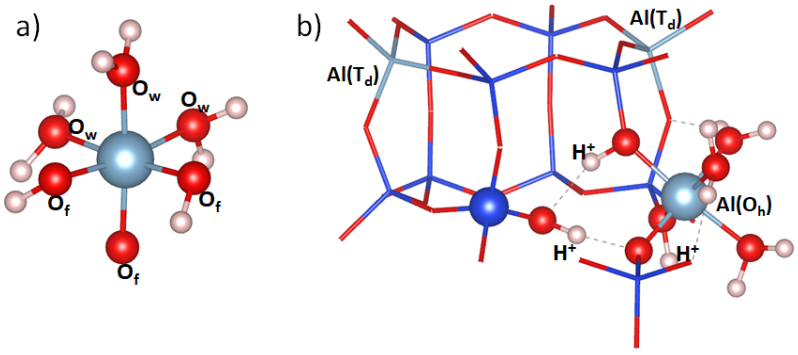

Figure 3.28: a) The cluster showing octahedral arrangement of the central Al atom in LAS(6) species. b) LAS(6) structure formed in the D6R in CHA zeolite, with positions of all three Brønsted protons also shown.

Table 3.4: Charge distribution analysis of LAS(6) performed with four different models: Bader, (Loewdin), [Mulliken] and <crystal-orbital-overlap-population>.

Group/molecule	**6 water/unit cell** 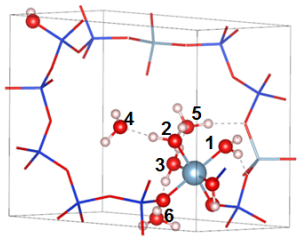	**3 water/unit cell** 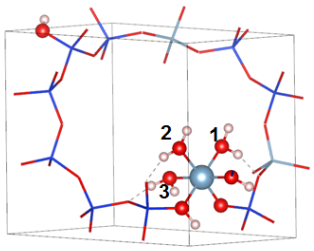
Al1(T_d)	**-0.72**(-0.44)[-0.54]<-0.77>	**-0.73**(-0.53)[-0.44]<-0.75>
Al2(O_h)	**1.45**(1.25)[1.08]<1.32>	**1.51**(1.28)[1.42]<1.37>
Al3(T_d)	**-0.72**(-0.45)[-0.54]<-0.78>	**-0.71**(-0.53)[-0.44]<-0.77>
water no. 1	**-0.04**(0.05)[0.13]	**-0.04**(0.13)[0.03]
water no. 2	**-0.02**(0.06)[0.15]	**-0.02**(0.14)[0.05]
water no. 3	**-0.04**(-0.04)[0.05]	**0.00**(0.15)[0.06]
water no. 4	**0.03**(0.08)[0.10]	
water no. 5	**0.02**(0.08)[0.09]	
water no. 6	**0.04**(0.08)[0.08]	

The framework-associated octahedral aluminum, LAS(6) structure is formed in the CHA unit containing three BAS(4) sites initially. Only two (former) BAS(4) sites remain upon the LAS(6) formation and there are no charge compensating protons on either of two (former) BAS(4) sites, since protons are located on the LAS(6) structure. It is therefore expected that there are positive and negative charges localized on LAS(6) and (former) BAS(4) sites. To quantify this charge separation we analyzed the charge distribution for two different water loadings: 6 and 3 water molecules in UC. Since the partial charges are model-dependent quantities we have used four different models: Bader, Löwdin, Mulliken, and crystal-orbital-overlap-population charge analysis[117]. Charges on octahedral and tetrahedral Al are calculated as a sum (q_{Al}+ q_H+ ½ q_O) assuming that the half of the charge on oxygen atoms bound to Al belongs to the AlO_x unit. Results are summarized in Table 3.4. The presence of two H^+ on octahedral $AlO_{6/2}$ unit results in large positive charge on the unit that is neutralized by negative charge equally distributed between two (former) BAS(4) sites (-0.72 with Bader's

model). The charges on individual atoms (including O and H) are rather insensitive to its environment. Only small charges were found for water molecules.

3.3.2 Conditions for the existence of the framework-associated Al(Oh)

Both experimental evidence (investigation of samples with different Si/Al)[46] and the computational studies suggest that a critical local concentration of framework aluminum (and Brønsted sites) is required in order to form octahedral Al(Oh) species. The role of Si/Al, BAS site concentration, distance between framework Al atoms (all somewhat correlated) and the role of degree of hydration was thus investigated next.

Si/Al ratio: Experimental results show that the framework-associated Al(O_h) can be only detected for samples with sufficiently low Si/Al ratio and that this critical Si/Al ratio depends on the zeolite topology[52, 137]. All attempts to localize a stable LAS(6), or any other octahedral Al structure, have failed for a CHA(Si/Al=11) model containing just one Al atom in the D6R (Figure 3.29a). Such structures spontaneously transformed to BAS(4) or LAS(4) species during the first few ps of an AIMD simulation (Figure 3.29b). Thus, BAS(4) and LAS(4) were the only kinetically stable structures found for CHA(Si/Al=11). A previous study by some of us showed that BAS(4) and LAS(4) in CHA(Si/Al=11) are separated by a moderate barrier of $\Delta A^{\neq} < 40$ kJ mol^{-1}, while the BAS(4) structure is about 20 kJ mol^{-1} more stable than the LAS(4) one[7], in contrast to CHA(Si/Al=3) where both structures are almost isoenergetic.

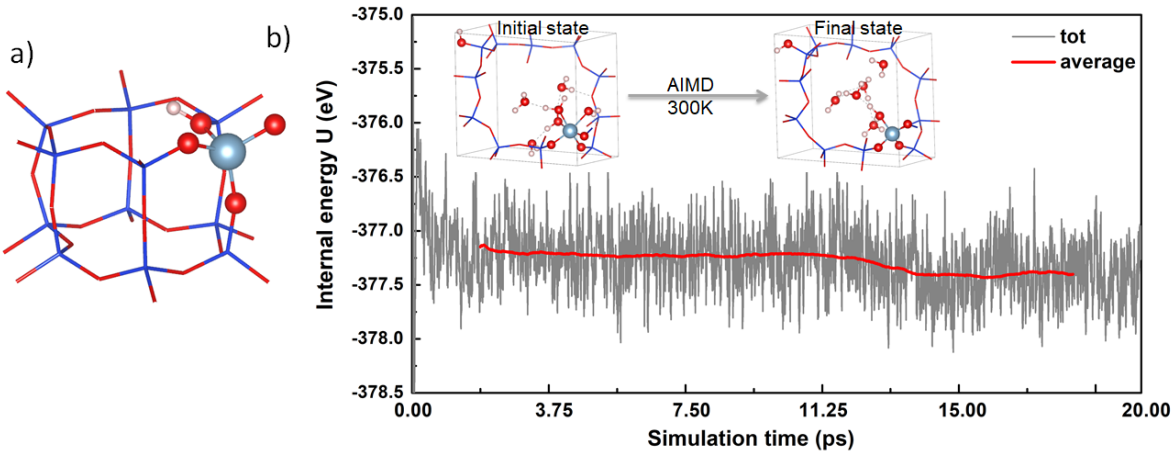

Figure 3.29: a) The CHA structure with Si/Al=11. b) The AIMD (at 300 K) trajectory with relative running averages for internal energy for the same model.

BAS concentration: Three protons are involved in the BAS(4) → LAS(6) transformation (see Figure 3.28b): two of them are firmly bound to Al(Oh)-O-Si bonds while the third one forms a silanol group. This third proton contributes to the LAS(6) stabilization via H-bonding between the hydroxyl hydrogen and an Al(Oh)-O-Si oxygen atom that is not binding a proton. We have attempted to determine how critical the presence of protons is on Al(Oh)-O-Si bridges (Figure 3.30): Moving one of the protons from LAS(6) to one of the BAS(4) oxygens within the same CHA cage does not lead to the destruction of LAS(6). However, AIMD shows that the process is connected with an increase of system energy (+56 kJ mol^{-1}). Moving both protons from LAS(6) to BAS(4) sites also leads to an increase of the system energy (+19 kJ mol^{-1}, as is already seen from Figure 3.27). However, this process involves a spontaneous transformation of LAS(6) back to BAS(4) and solvation of one of the protons, as shown in Figure 3.30a. Hence, the presence of at least one proton on an Al(Oh)-O-Si oxygen atom appears to be necessary for the stabilization of the octahedral Al moiety.

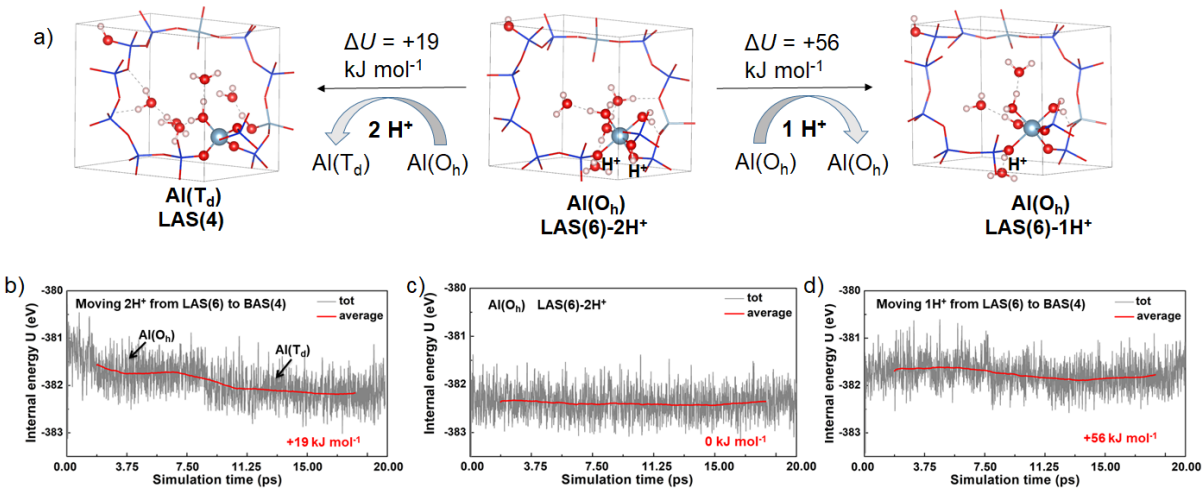

Figure 3.30: a) Structures and relative internal energies (at 300 K) of the CHA models with the framework Al with different number of protons on the framework oxygen atoms of the first coordination shell of Al; Al(Oh) with two protons is thermodynamically the most stable (middle). The structure with one proton remains octahedral but is the least stable (right). The structure with no protons collapses to tetrahedral LAS(4) with a single water molecule attached to an Al atom (left). b) AIMD trajectory for the three structures described above and their relative internal energies (the running average internal energy of the last 5000 snapshots in AIMD simulation).

Al-O-Si-O-Al pairing: One of the Al atoms of an Al-O-Si-O-Al pair transforms into LAS(6). A rather similar *fac*-$Al(O_f)_3(H_2O)_3$ complex was also found for the Al atom which is separated by at least two framework silicon from another framework aluminum and again, three protons were involved in the LAS(6) formation (see Figure 3.31a). However, this LAS(6) structure, formed by breaking of the Al-O bond at O4 oxygen (Figure 3.31a,d), is less stable than the reference BAS(4) structure (by +43 kJ mol^{-1}). Formation of other prospective LAS(6) species by breaking the bonds at other oxygens (O1, O3) leads to (dynamically) unstable LAS(6) species (see Figures 3.31a-c). Thus, the transformation from BAS(4) to LAS(6) is kinetically allowed even for Al atoms that are not involved in Al-O-Si-O-Al pairs. However, such species are thermodynamically less stable and unlikely to be observed experimentally.

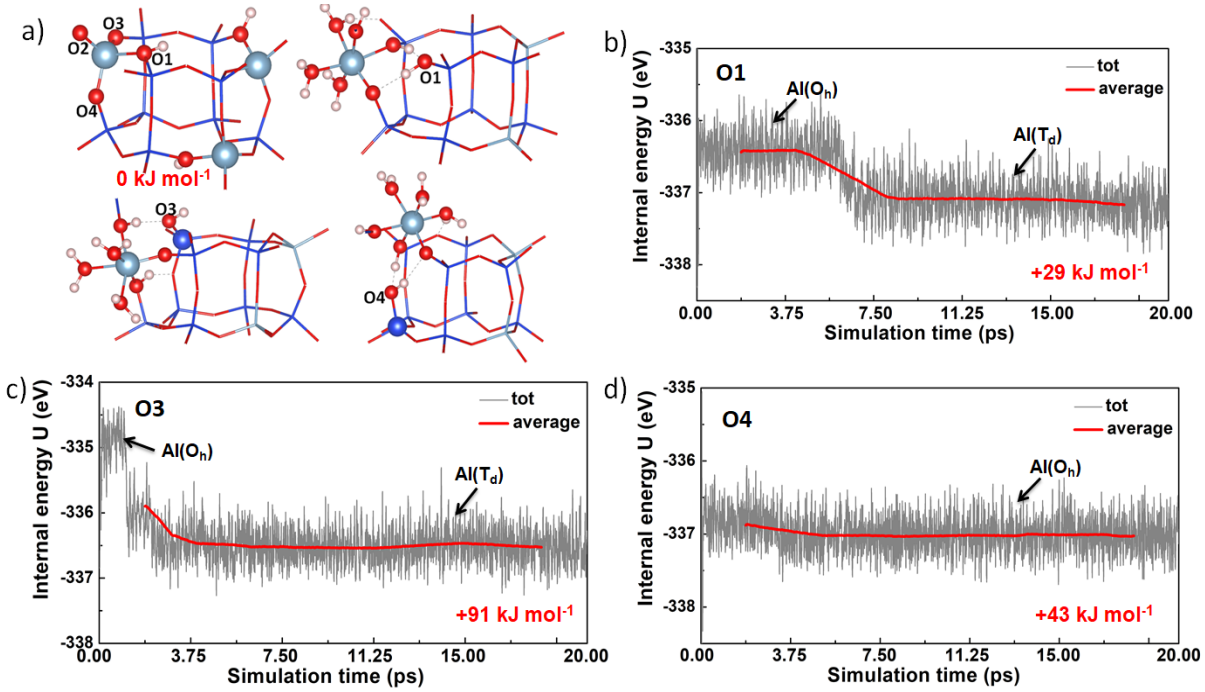

Figure 3.31: a) The structures of BAS(4) and LAS(6) on the 'isolated' Al differing in the choice of the hydrolyzed Al-O bond. b)-d) the AIMD trajectories corresponding to the hydrolysis of Al-O1, Al-O3 and Al-O4 bonds, respectively.

Table 3.5: Detachment energies of individual water molecules from the LAS(6) octahedral structure; 1st and 2nd coordination shell water molecules are numbered 1-3 and 4-6, respectively (see equation 2.18).

Removal of	6 water/unit cell	3 water/unit cell
	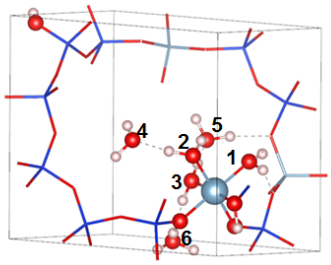	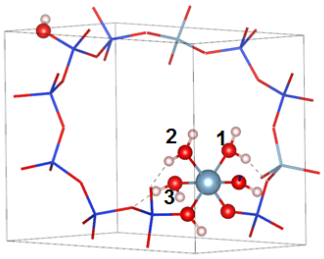
water no. 1	137	145
water no. 2	139	139
water no. 3	118	118
water no. 4	73	
water no. 5	94	
water no. 6	115	

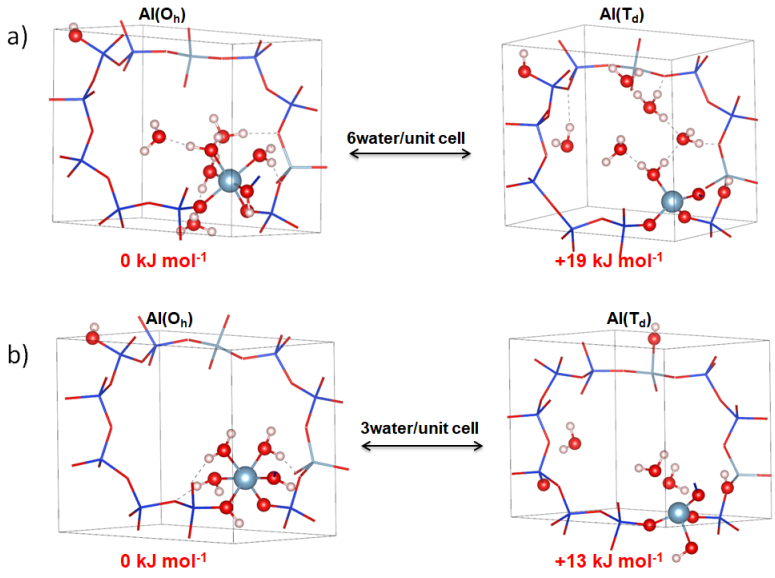

Figure 3.32: The structures and relative stability of Al(Oh) and Al(Td) species with a) 6 and b) 3 water in the unit cell obtained from AIMD simulations. The relative energies are calculated as the running average of internal energy from the last 5000 snapshots in the AIMD simulations.

Water concentration: Individual water molecules are firmly bound to Al(Oh) species. Interaction energies for water molecules in the first (denoted 1, 2 and 3 in Table 3.5) and second (denoted 4-6) coordination shell are either larger or smaller than -118 kJ mol^{-1}, respectively. The role of water quantity on the relative stability of LAS(6) and BAS(4) structures was investigated, by decreasing the number of water molecules in the CHA cage from 6 to 3 (removing all water from the second coordination shell). Very similar relative energies were obtained for LAS(6) and BAS(4) structures for both water concentrations, which was confirmed further by running 20 ps long AIMD simulation for both water concentrations (see Figure 3.32). Thus, the stability of LAS(6) structure is not compromised even when the water loading is reduced to half.

3.3.3 Summary

The structure and formation mechanisms of the framework-associated Al(Oh) species have been proposed for the first time. The computational investigations on a CHA zeolite model with Si/Al=3 confirm that the framework-associated Al(Oh) is thermodynamically stable and kinetically connected to BAS at the room temperature. The conditions for existence of framework-associated Al(Oh) include: (i) Three BAS sites must exist in close proximity to each other to allow transfer and fixation of protons around the to-be-formed octahedral aluminum. (ii) Octahedral Al is formed from one of the Al atoms of the Al-O-Si-O-Al pair, where Al atoms are separated by a single framework silicon atom. (iii) The presence of water molecules is required to create and stabilize the Al(Oh) species, and realistic dynamical description of water solvation is thus of great importance.

4. Discussion

4.1 Water loading

The water concentration has a significant effect on both the mechanisms and energies of the hydrolysis process. Increasing the loading of water molecules can introduce new more competitive hydrolysis mechanisms, *i.e.*, *axial*, *S2R* and the catalytic *M3* mechanisms. The cooperation between water molecules can create an environment conducive to hydrolysis and effectively reduce the barriers of the reactions. Hence, it is essential to consider the effects of liquid-like water molecules present in the zeolite pores even if they are not directly involved in framework scission (see *e.g.*, section 3.2.2).

Due to the diversity of the zeolite frameworks, it's crucial to think about which factors affect the water loading in the zeolite pores and by extension also the related hydrolysis mechanism. The effective accessible volume for water in the pores zeolites is limited and assuming the water density is comparable to the room temperature water density (1 g cm^{-3}) or lower, the water adsorption capacity of the zeolite unit cell is typically not very large. *e.g.*, the water adsorption capacity of zeolite CHA is approximately five water molecules per CHA cage[7, 138-139]. Several factors influence the actual water loading in the zeolite channels. The first factor is the heteroatom type (*e.g.*, heteroatoms with the oxidation number IV such as Ge, Sn, Ti, *etc*. or with the oxidation number III such as Al or B which is accompanied by the presence of charge compensating cations) and their concentration. For aluminosilicate zeolites, the strong interaction between water molecules and cationic sites such as Brønsted acid sites (BAS) will increase hydrophilicity significantly, and many zeolites have been studied to establish a clear positive correlation between water adsorption and the framework aluminum content[31, 140-144], showing, *e.g.*, for the MFI case that up to 7 water molecules can be accommodated by a single BAS site[144]. The presence of other heteroatoms (Ge, Sn, Ti, …) also increases the hydrophilicity of the zeolites, however, to a much lower degree than aluminum and most of the hydrophilicity increase commonly associated with the increase in Ge, Sn or Ti concentration appears to be rather related with the increase in the defects concentration[31]. Hence, the second factor influencing water loading is the defect concentration, since the majority of the defects are hydrophilic such as the silanol nests, and the isolated silanol, germanol or stannol groups. For example, in section 3.1.1 we showed how partial hydrolysis of pristine hydrophobic UTL zeolite leads to generation of silanol/germanol-containing defects that adsorb water molecules twice as strongly as the pristine germanium Lewis sites

with the water adsorption energy being almost as high as for the water bound to the BAS site. Seeing new low barrier hydrolysis mechanisms taking place at the high water loading, it comes as no surprise that the rate of hydrolysis has been shown experimentally to be significantly influenced by the defect concentration[38]. The third factor is the distance from the external surface to the pores since the hydrolysis rate may be limited by the kinetics of water diffusion and a gradient in the reactant/water concentration is probably established as a function of depth. Each of these factors affects the amount of water available to participate in the zeolite hydrolysis and by extension it influences the hydrolysis mechanism and the hydrolysis rate.

4.2 Ge content

The germanium content in the zeolite UTL framework not only affects the water loading but also the hydrolytic lability of the structure. The introduction of germanium greatly improves the ability to guide the synthesis of zeolite as well as convert them into new materials by post-synthesis modifciations[1-6]. Germanium has an important structure-directing effect, *i.e.*, it can induce the formation of the precursors of D4R units, promote the crystallization of D4Rs-containing zeolites, and stabilize the final structures[13, 145-146]. In addition, it is well documented in the literature[37, 81-83] that germanium in many zeolites such as UTL, UOV, IWW are expected to preferentially occupy the D4R units, and the occupation of S4R units parallel to the layer may enable delamination[37]. Our analysis of such a preferential clustering of Ge atoms in our computational models (see Section 3.1.4) clearly shows that increasing the Ge content in S4R (as a part of D4R unit) from two to four atoms not only lowers the reaction barriers to the first hydrolytic step but also significantly stabilizes (by approximately 60 kJ/mol) the resulting *S2R* products. As a result, the reaction becomes highly exothermic and may provide the necessary surplus energy for further reaction steps. Hence, we are able to relate the observed step-change in hydrolytic (in)stability of germanosilicate zeolites[1-6, 121], as a function of germanium concentration, to reaching a critical concentration of about 4 germaniums per D4R (or rather per S4R), which opens up new exergonic hydrolysis pathways with very low activation barriers.

4.3 Neutral *vs* alkaline conditions

Under the conditions of minimum water loading in neutral conditions, the effective barrier of the initial hydrolysis step, via the *M1* mechanism (section 3.2.1), is 194 kJ mol^{-1}. Such a high barriers make desilication at low water conditions unfeasible, at variance to the dealumination

with single water molecule[7, 60], which explains: i) the observed selectivity of zeolites towards selective dealumination under steam conditions, and ii) good thermal stability of the high silica-zeolites. Therefore, *M1* mechanism is unlikely to play an important role in the desilication of zeolites at moderate temperatures.

Under the anhydrous alkaline conditions, NaOH acts as reactant breaking the siloxane bonds via the *M2* mechanism. NaOH can drive the complete desilication from the pristine zeolite to the formation of orthosilicic acid. The energy barriers of each step are low (less than 60 kJ mol^{-1}) and reaction energies for all but the first step are exothermic. In other words, the presence of NaOH greatly accelerates the desilication of high-silica zeolites. These results are consistent with the previous findings of Zhai *et al.*[71] (see Figure 1.3d), who employed successive S_N2-like mechanism to hydrolyze the surface of ZSM-5 with NaOH. However, work of Zhai *et al.* did not consider the effects of solvent and the proposed mechanism resulted in large consumption of NaOH.

Hydrolysis under neutral, high water conditions, can proceed following the Grotthuss-type *axial* mechanism as shown previously by the work carried out in our group[7]. The initial $Q^4 \rightarrow Q^3$ hydrolysis step barrier for desilication (at 300 K) and degermanation (at 370 K) is only 65 kJ mol^{-1} and 37 kJ mol^{-1} (see section 3.1.3), respectively. Such low barriers allow the initial hydrolysis to be achieved under mild conditions. However, the preliminary calculations indicate that the subsequent $Q^3 \rightarrow Q^2$ hydrolysis step can be more difficult than the $Q^4 \rightarrow Q^3$ step[121], because the hydrophilic groups (silanols/germanols) formed by partial hydrolysis can interfere with the Grotthuss proton transfer, an essential step of the *axial* mechanism. Thus, it is predicted, at least for the desilication pathway, that the *axial* mechanism will rather lead to reversible partial hydrolysis of the framework than to the complete hydrolysis under ambient conditions, which was verified experimentally[7].

Hydrolysis under alkaline (NaOH) microsolvation conditions was found to initiate with a fast and exothermic $Q^4 \rightarrow Q^3$ step. This is due to a fact that the stabilization of the Na^+ cation and the formation of a hydrogen bonding network around the Q^3Si-OH moiety is energetically favorable when sufficient water molecules are present. The $Q^4 \rightarrow Q^3$ step provides energy for subsequent steps, which are expected to proceed by the novel catalytic mechanism (*M3*). This new mechanism accessible at microsolvation (two waters per reactive center) is feasible under mild conditions and it does not consume NaOH. Hence, it may to lead to substantial desilication, even with only small concentration of NaOH in the pores.

4.4 Generality of the mechanisms

Novel mechanisms (*axial, S2R, geminal, M2/M3*) discovered in this work are expected to be of general nature, extendable in part to other zeolites with different Lewis acid sites, such as tin- and titanium-zeolites. First, the *axial* mechanism has been observed previously by some of us for Si-O-Si hydrolysis in purely siliceous CHA model[7], confirming the general nature of such a mechanism. This expectation is corroborated by recent reports of the formation of a stable Q^3 axial products in Sn-BEA using static DFT calculations[78-79]. Although, these calculations were done in low water conditions, they at least confirm the stability of *axial* products also for tin-zeolites. Besides the *axial* mechanism, also the *geminal* and *S2R* mechanisms could be theoretically generalized also for tin- or titanium-zeolites, due to a propensity of these atoms to increase their coordination beyond four. However, since tin- and titanium-zeolites can be typically prepared only with very low heteroatom content, we expect that such mechanisms may not be applicable in selective hydrolysis of such zeolites.

In addition, we see no clear reason why the novel mechanisms should not be applicable to other zeolite topologies. In case of *axial* mechanism, we note that its favorability will be contingent on: i) the accessibility of the T sites, and ii) ability to form a stable Q^3Si/Q^3Ge *axial* product that would not be in strong steric repulsion with the framework (see Section 3.1.1). In particular, the T site needs to be well accessible to water both to allow water adsorption followed by the formation of penta-coordinated Si/Ge center and to allow proton attack to the framework oxygen in *axial* position. Taking UTL as an example (see Section 3.1.1), the D4R and adjacent T sites are well-accessible to *axial* attack, however, most of the T sites in the UTL layer are not. Hence, this provides further justification for the (observed) increased hydrolytic stability of UTL layers in comparison to the interlayer[121]. Importantly, the accessibility notion can be straightforwardly extended to other zeolites and used to gauge their propensity for selective hydrolysis, justifying, *e.g.*, the difficulties in selective delamination of zeolites with three-dimensional channel systems[132]. The alkaline hydrolysis (*M2/M3* mechanisms) is also expected to be influenced by the accessibility, as the hydrolysis products are also of an *axial* type with inverted Si tetrahedron and -ONa and -OH bonds in *axial* positions with respect to each other. Hence, the accessibility of this product state is topology-dependent and may become a hindrance for the scission of siloxane bonds, which are not exposed to the pore from both sides. Hydrolysis is thus more likely to take place at intersection T sites and sites in interlayer rings. Besides the *axial* mechanism, the *geminal* and *S2R* mechanisms should be also applicable to other topologies. However, our calculations

show the *S2R* mechanism requires germanium to be densely clustered, *e.g.*, in the S4R rings. Hence, we may expect that topologies that would disfavor such dense clustering of germanium might be hydrolytically stable even for rather high Si/Ge ratios while the contrary will be true for topologies favoring germanium clustering such as UTL.

The applicability of the *M2/M3* mechanisms to other topologies will likely depend on the pore confinement which determines the degree of solvation. For small pore zeolites, such as CHA, we assume that microsolvation conditions are realistic and thus we expect the catalytic *M3* mechanism to be of importance for this class of zeolites. Our preliminary calculations for FER zeolites confirm this assumption[133]. However, if bulkier species (countercations, co-solvents, reagents, *etc.*) are present in the system, which have larger excluded volume, the number of waters available for solvation/NaOH-dissociation may be limited and with it also the applicability of the *M2/M3* mechanisms. Conversely, for large pore zeolites such as FAU, water can completely solvate the Na^+ cation detaching it from the framework and thus changing the charge distribution at the reaction center[147-148]. In other words, full solvation conditions are expected to be more realistic than the microsolvation conditions considered herein (see section 3.2). This can affect the competitiveness of the *M3* mechanism in particular. Overall, the microsolvation regime is expected to be applicable for small pore and highly siliceous zeolites, for which the *M2* and *M3* mechanisms are anticipated to play a significant role in zeolite desilication under alkaline conditions.

5. Conclusion

In this dissertation, we performed the quantum chemistry calculations to systematically study the hydrolysis mechanism of zeolites under realistic conditions. The whole dissertation is of a purely computational nature, however, most of the research has been done in close collaboration with the experimentalists, and great attention has been paid to ensure comparability of computational models and experiments[120-121]. We produced simulation data that agree almost quantitatively with the experimental ones, including adsorption and NMR measurements. The dissertation focused on three self-contained but closely related topics with the following conclusions:

(1) In the first project, we investigated the hydrolysis mechanism of the germanosilicate UTL with different Si/Ge ratios and water loading and found that the water loading and Ge content play a very important role in the disassembly process of this prototypical ADORable zeolite. The increase of germanium content lowers the hydrolysis barriers in both the low and the high water loading condition, in the latter significantly so. Ge atoms are known to cluster in the UTL framework[37], and we show that especially the formation of Ge clusters in S4R units (embedded in D4R unit) can significantly destabilize the framework towards the water. In the high Ge models (and especially under high water loading conditions), the UTL framework easily interacts with water to form stable *S2R* products (involving Ge-(O_f)(O_w)-Ge species) via the *S2R* mechanism, releasing a lot of energy in the process, which can be used for further hydrolysis. In the low Ge models, loading the micropores of UTL with water opens up an energetically favorable *axial* mechanism, which leads to formation of stable *axial* product through the Grotthuss-type proton shuttling. Both of these mechanisms (*S2R* and *axial*) are of highly cooperative nature either with respect to cooperation of waters in the proton shuttle or with respect to increased local flexibility and reactivity of the D4R units filled with germanium. This study clearly fills the gap in the research on the hydrolysis of germanosilicate zeolites, describing the degermanation process for the first time at the molecular level. In addition, the calculation methods used in this work adopt reasonably realistic models of the germanosilicate zeolite under realistic conditions, with an explicit consideration of temperature and solvation, which increases the significance of our results. Lastly, this work has a potential to inform future attempts to synthesize new zeolites from germanosilicate precursors.

(2) In the second project, we used a realistic model of siliceous zeolite CHA to conduct detailed research of the hydrolysis mechanism in the pore interior under neutral/alkaline conditions and we proposed several mechanisms taking place at different reaction conditions. This water-induced desilication was calculated sequentially, from the first bond breaking step to the full removal of an $Si(OH)_4$ group from the framework. We found that the NaOH enhances the rate of zeolite hydrolysis in each step by a significant amount as compared to hydrolysis taking place in neutral conditions. We calculated the reaction pathway in which NaOH acts as a reactant (*M2* mechanism), easily breaking siloxane bonds already at the room temperature, however, this pathway leads to large NaOH overall consumption and it will be hindered by microsolvating water. We also identified a pathway in which NaOH acts as a catalyst that is regenerated *in situ* (*M3* mechanism), this catalytic mechanism requires very low concentration of NaOH present in the reaction mixture. Moreover, the presence of microsolvating water lowers the barriers for NaOH catalyst regeneration. Both mechanisms (*M2* and *M3*) are energetically feasible, and the preference of one over the other will be determined by the concentration of NaOH and water in the zeolite pores. This study provides systematic mechanistical understanding of the role of alkali molecules in the desilication process of zeolite hydrolysis, and it also shows that although high silica zeolites are hydrophobic, the hydrolysis proceeding from the pore interior is feasible under alkaline conditions.

(3) Lastly, we studied the reversible transformation between tetrahedral Al(Td) species and framework-associated Al(Oh) species in the zeolite CHA, obtaining the free energies profiles for the transformation all the way from Brønsted acid site (BAS) via tetrahedral Lewis acid sites (LAS) to the octahedral Al(Oh) species. We found that the framework-associated Al(Oh) is thermodynamically stable, it is kinetically connected to BAS at room temperature and it can be produced under the following conditions: (i) Three BAS sites must exist in close proximity to each other, to allow transfer and fixation of protons around the to-be-formed octahedral aluminum. (ii) Framework-associated Al(Oh) can be formed from one of the Al atoms of the Al-O-Si-O-Al pair, since the stability of Al(Oh) is greatly reduced for Al atoms separated by two framework silicon atoms from the other Al sites. (iii) The presence of water molecules is required (at least three waters in the CHA cage) for existence of Al(Oh). In summary, this study resolves the question about the nature and reversibility of framework-associated Al(Oh) species in CHA zeolite (applicable probably also for other topologies) and brings additional evidence that the framework of acidic zeolites becomes labile under wet conditions.

We have identified many intriguing hydrolysis mechanisms in zeolites covering a range of water loadings in the zeolites pores, range of conditions (neutral and alkaline) and also a range of zeolites types including purely silicieous (CHA), aluminosilicate (CHA) and even germanosilicate zeolites (UTL). Many of our findings can be straightforwardly extended to other zeolite frameworks and even contemplated to be applied to other heteroatom-exchanged zeolites such as tin- and titanium-exchanged zeolites. Our results will help to improve the understanding of the role of environmental factors in the behaviour of zeolites under the conditions in which they are actually utilized. The calculation methods used in zeolite hydrolysis will promote a new paradigm of modelling materials under realistic conditions. Ultimately, this study will open new avenues for the research in the future, by allowing us to develop a computational platform appropriate to a wider range of reactions, from adsorption in molecular sieves, to catalysis, and further towards assembly and disassembly of porous materials. This will eventually help experimentalists working to improve catalyst performance, decrease catalyst degradation and increase catalyst durability.

References

1. Eliášová, P.; Opanasenko, M.; Wheatley, P. S.; Shamzhy, M.; Mazur, M.; Nachtigall, P.; Roth, W. J.; Morris, R. E.; Čejka, J., The ADOR mechanism for the synthesis of new zeolites. *Chem. Soc. Rev.* **2015,** *44* (20), 7177-7206.
2. Verheyen, E.; Joos, L.; Van Havenbergh, K.; Breynaert, E.; Kasian, N.; Gobechiya, E.; Houthoofd, K.; Martineau, C.; Hinterstein, M.; Taulelle, F., Design of zeolite by inverse sigma transformation. *Nat. Mater.* **2012,** *11* (12), 1059-1064.
3. Mazur, M.; Wheatley, P. S.; Navarro, M.; Roth, W. J.; Položij, M.; Mayoral, A.; Eliášová, P.; Nachtigall, P.; Čejka, J.; Morris, R. E., Synthesis of 'unfeasible'zeolites. *Nat. Chem.* **2016,** *8* (1), 58-62.
4. Henkelis, S. E.; Morris, S. A.; Mazur, M.; Wheatley, P. S.; McHugh, L. N.; Morris, R. E., Monitoring the assembly–disassembly–organisation–reassembly process of germanosilicate UTL through in situ pair distribution function analysis. *J. Mater. Chem. A* **2018,** *6* (35), 17011-17018.
5. Roth, W. J.; Shvets, O. V.; Shamzhy, M.; Chlubná, P.; Kubů, M.; Nachtigall, P.; Čejka, J. i., Postsynthesis transformation of three-dimensional framework into a lamellar zeolite with modifiable architecture. *J. Am. Chem. Soc.* **2011,** *133* (16), 6130-6133.
6. Roth, W. J.; Nachtigall, P.; Morris, R. E.; Wheatley, P. S.; Seymour, V. R.; Ashbrook, S. E.; Chlubná, P.; Grajciar, L.; Položij, M.; Zukal, A., A family of zeolites with controlled pore size prepared using a top-down method. *Nat. Chem.* **2013,** *5* (7), 628-633.
7. Heard, C. J.; Grajciar, L.; Rice, C. M.; Pugh, S. M.; Nachtigall, P.; Ashbrook, S. E.; Morris, R. E., Fast room temperature lability of aluminosilicate zeolites. *Nat. Commun.* **2019,** *10* (1), 4690.
8. Čejka, J.; Morris, R. E.; Nachtigall, P., *Zeolites in Catalysis: Properties and Applications*. The Royal Society of Chemistry, 2017.
9. Čejka, J.; Bekkum, H. v.; Corma, A.; Schueth, F., *Introduction to Zeolite Molecular Sieves, volume 168,3rd Edition*. Elsevier Science, 2007.
10. Rani, P.; Srivastava, R., Comprehensive understanding of the eco-friendly synthesis of zeolites: needs of 21st century sustainable chemical industries. *Chem. Rec.* **2020,** *20* (9), 968-988.
11. Database of Zeolite Structures http://www.iza-structure.org/databases/
12. Meier, W. M.; Olson, D. H., *Atlas of Zeolite Structure Types*. Polycrystal Book Service, Pittsburgh, 1978.

13. Opanasenko, M.; Shamzhy, M.; Wang, Y.; Yan, W.; Nachtigall, P.; Čejka, J., Synthesis and post-synthesis transformation of germanosilicate zeolites. *Angew. Chem. Int. Ed.* **2020,** *59* (44), 19380-19389.
14. Blasco, T.; Camblor, M.; Corma, A.; Perez-Pariente, J., The state of Ti in titanoaluminosilicates isomorphous with zeolite. beta. *J. Am. Chem. Soc.* **1993,** *115* (25), 11806-11813.
15. Zhou, D.; Zhang, T.; Xia, Q.; Zhao, Y.; Lv, K.; Lu, X.; Nie, R., One-pot rota-crystallized hollownest-structured Ti–zeolite: a calcination-free and recyclable catalytic material. *Chem. Sci.* **2016,** *7* (8), 4966-4972.
16. Tong, W.; Yin, J.; Ding, L.; Xu, H.; Wu, P., Modified Ti-MWW zeolite as a highly efficient catalyst for the cyclopentene epoxidation reaction. *Front. Chem.* **2020,** *8*.
17. Millini, R.; Perego, G.; Bellussi, G., Synthesis and characterization of boron-containing molecular sieves. *Top. Catal.* **1999,** *9* (1), 13-34.
18. Marthala, V. R.; Hunger, M.; Kettner, F.; Krautscheid, H.; Chmelik, C.; Kärger, J. r.; Weitkamp, J., Solvothermal synthesis and characterization of large-crystal all-silica, aluminum-, and boron-containing ferrierite zeolites. *Chem. Mater.* **2011,** *23* (10), 2521-2528.
19. Altvater, N. R.; Dorn, R. W.; Cendejas, M. C.; McDermott, W. P.; Thomas, B.; Rossini, A. J.; Hermans, I., B-MWW zeolite: the case against single-site catalysis. *Angew. Chem.* **2020,** *132* (16), 6608-6612.
20. Védrine, J. C.; Auroux, A.; Dejaifve, P.; Ducarme, V.; Hoser, H.; Zhou, S., Catalytic and physical properties of phosphorus-modified ZSM-5 zeolite. *J. Catal.* **1982,** *73* (1), 147-160.
21. Flanigen, E. M.; Grose, R. W., Phosphorus Substitution in Zeolite Frameworks. ACS Publications: 1971.
22. Wolf, P.; Hammond, C.; Conrad, S.; Hermans, I., Post-synthetic preparation of Sn-, Ti- and Zr-beta: a facile route to water tolerant, highly active Lewis acidic zeolites. *Dalton Trans.* **2014,** *43* (11), 4514-4519.
23. Tang, B.; Li, S.; Song, W.-C.; Yang, E.-C.; Zhao, X.-J.; Guan, N.; Li, L., Fabrication of hierarchical Sn-Beta zeolite as efficient catalyst for conversion of cellulosic sugar to methyl lactate. *ACS Sustainable Chem. Eng.* **2020,** *8* (9), 3796-3808.
24. Li, Y.; Yu, J., New stories of zeolite structures: their descriptions, determinations, predictions, and evaluations. *Chem. Rev.* **2014,** *114* (14), 7268-7316.

25. Van Donk, S.; Janssen, A. H.; Bitter, J. H.; de Jong, K. P., Generation, characterization, and impact of mesopores in zeolite catalysts. *Catal. Rev.* **2003,** *45* (2), 297-319.
26. Pérez-Ramírez, J.; Christensen, C. H.; Egeblad, K.; Christensen, C. H.; Groen, J. C., Hierarchical zeolites: enhanced utilisation of microporous crystals in catalysis by advances in materials design. *Chem. Soc. Rev.* **2008,** *37* (11), 2530-2542.
27. Fechete, I.; Wang, Y.; Védrine, J. C., The past, present and future of heterogeneous catalysis. *Catal. Today* **2012,** *189* (1), 2-27.
28. Primo, A.; Garcia, H., Zeolites as catalysts in oil refining. *Chem. Soc. Rev.* **2014,** *43* (22), 7548-7561.
29. Cheng, W.-C.; Kim, G.; Peters, A.; Zhao, X.; Rajagopalan, K.; Ziebarth, M.; Pereira, C., Environmental fluid catalytic cracking technology. *Catal. Rev.* **1998,** *40* (1-2), 39-79.
30. Vogt, E. T. C.; Weckhuysen, B. M., Fluid catalytic cracking: recent developments on the grand old lady of zeolite catalysts. *Chem. Soc. Rev.* **2015,** *44*, 7342-7370.
31. Heard, C. J.; Grajciar, L.; Uhlík, F.; Shamzhy, M.; Opanasenko, M.; Čejka, J.; Nachtigall, P., Zeolite (in)stability under aqueous or steaming conditions. *Adv. Mater.* **2020,** *32* (44), 2003264.
32. Ennaert, T.; Van Aelst, J.; Dijkmans, J.; De Clercq, R.; Schutyser, W.; Dusselier, M.; Verboekend, D.; Sels, B. F., Potential and challenges of zeolite chemistry in the catalytic conversion of biomass. *Chem. Soc. Rev.* **2016,** *45* (3), 584-611.
33. Li, Y.; Li, L.; Yu, J., Applications of zeolites in sustainable chemistry. *Chem* **2017,** *3* (6), 928-949.
34. Groen, J. C.; Jansen, J. C.; Moulijn, J. A.; Pérez-Ramírez, J., Optimal aluminum-assisted mesoporosity development in MFI zeolites by desilication. *J. Phys. Chem. B* **2004,** *108* (35), 13062-13065.
35. Milina, M.; Mitchell, S.; Crivelli, P.; Cooke, D.; Pérez-Ramírez, J., Mesopore quality determines the lifetime of hierarchically structured zeolite catalysts. *Nat. Commun.* **2014,** *5* (1), 1-10.
36. Octaviani, S.; Krisnandi, Y. K.; Abdullah, I.; Sihombing, R., The effect of alkaline treatment to the structure of ZSM5 zeolites. *Makara J. Sci.* **2013**, 155-162.
37. Kasian, N.; Tuel, A.; Verheyen, E.; Kirschhock, C. E.; Taulelle, F.; Martens, J. A., NMR evidence for specific germanium siting in IM-12 zeolite. *Chem. Mater.* **2014,** *26* (19), 5556-5565.
38. Zhang, L.; Chen, K.; Chen, B.; White, J. L.; Resasco, D. E., Factors that determine zeolite stability in hot liquid water. *J. Am. Chem. Soc.* **2015,** *137* (36), 11810-11819.

39. Čižmek, A.; Komunjer, L.; Subotić, B.; Aiello, R.; Crea, F.; Nastro, A., Kinetics of zeolite dissolution: Part 4. Influence of the concentration of silicon in the liquid phase on the kinetics of ZSM-5 dissolution. *Zeolites* **1994,** *14* (3), 182-189.
40. Čižmek, A.; Subotić, B.; Aiello, R.; Crea, F.; Nastro, A.; Tuoto, C., Dissolution of high-silica zeolites in alkaline solutions I. Dissolution of silicalite-1 and ZSM-5 with different aluminum content. *Micropor. Mat.* **1995,** *4* (2-3), 159-168.
41. Ogura, M.; Shinomiya, S.-y.; Tateno, J.; Nara, Y.; Kikuchi, E.; Matsukata, M., Formation of uniform mesopores in ZSM-5 zeolite through treatment in alkaline solution. *Chem. Lett.* **2000,** *29* (8), 882-883.
42. Suzuki, T.; Okuhara, T., Change in pore structure of MFI zeolite by treatment with NaOH aqueous solution. *Micropor. Mesopor. Mat.* **2001,** *43* (1), 83-89.
43. Ong, L. H.; Dömök, M.; Olindo, R.; van Veen, A. C.; Lercher, J. A., Dealumination of HZSM-5 via steam-treatment. *Micropor. Mesopor. Mat.* **2012,** *164*, 9-20.
44. Xue, N.; Vjunov, A.; Schallmoser, S.; Fulton, J. L.; Sanchez-Sanchez, M.; Hu, J. Z.; Mei, D.; Lercher, J. A., Hydrolysis of zeolite framework aluminum and its impact on acid catalyzed alkane reactions. *J. Catal.* **2018,** *365*, 359-366.
45. Bourgeat-Lami, E.; Massiani, P.; Di Renzo, F.; Espiau, P.; Fajula, F.; Des Courières, T., Study of the state of aluminium in zeolite-β. *Appl. Catal.* **1991,** *72* (1), 139-152.
46. Ravi, M.; Sushkevich, V. L.; van Bokhoven, J. A., Lewis acidity inherent to the framework of zeolite mordenite. *J. Phys. Chem. C* **2019,** *123* (24), 15139-15144.
47. Wouters, B.; Chen, T.-H.; Grobet, P., Reversible tetrahedral−octahedral framework aluminum transformation in zeolite Y. *J. Am. Chem. Soc.* **1998,** *120* (44), 11419-11425.
48. Ravi, M.; Sushkevich, V. L.; van Bokhoven, J. A., Towards a better understanding of Lewis acidic aluminium in zeolites. *Nat. Mater.* **2020,** *19* (10), 1047-1056.
49. van Bokhoven, J. A.; Van der Eerden, A. M.; Koningsberger, D. C., Three-coordinate aluminum in zeolites observed with in situ X-ray absorption near-edge spectroscopy at the Al K-edge: flexibility of aluminum coordinations in zeolites. *J. Am. Chem. Soc.* **2003,** *125* (24), 7435-7442.
50. Omegna, A.; van Bokhoven, J. A.; Prins, R., Flexible aluminum coordination in alumino-silicates. Structure of zeolite H-USY and amorphous silica-alumina. *J. Phys. Chem. B* **2003,** *107* (34), 8854-8860.
51. van Bokhoven, J. A.; Sambe, H.; Ramaker, D.; Koningsberger, D., Al K-edge near-edge X-ray absorption fine structure (NEXAFS) study on the coordination structure of aluminum in minerals and Y zeolites. *J. Phys. Chem. B* **1999,** *103* (36), 7557-7564.

52. Abraham, A.; Lee, S.-H.; Shin, C.-H.; Hong, S. B.; Prins, R.; van Bokhoven, J. A., Influence of framework silicon to aluminium ratio on aluminium coordination and distribution in zeolite Beta investigated by 27Al MAS and 27Al MQ MAS NMR. *Phys. Chem. Chem. Phys* **2004,** *6* (11), 3031-3036.
53. Dapsens, P. Y.; Mondelli, C.; Pérez-Ramírez, J., Design of Lewis-acid centres in zeolitic matrices for the conversion of renewables. *Chem. Soc. Rev.* **2015,** *44* (20), 7025-7043.
54. Silaghi, M.-C.; Chizallet, C.; Raybaud, P., Challenges on molecular aspects of dealumination and desilication of zeolites. *Micropor. Mesopor. Mat.* **2014,** *191*, 82-96.
55. Ravenelle, R. M.; Schüβler, F.; D'Amico, A.; Danilina, N.; Van Bokhoven, J. A.; Lercher, J. A.; Jones, C. W.; Sievers, C., Stability of zeolites in hot liquid water. *J. Phys. Chem. C* **2010,** *114* (46), 19582-19595.
56. Agostini, G.; Lamberti, C.; Palin, L.; Milanesio, M.; Danilina, N.; Xu, B.; Janousch, M.; Van Bokhoven, J. A., In situ XAS and XRPD parametric rietveld refinement to understand dealumination of Y zeolite catalyst. *J. Am. Chem. Soc.* **2010,** *132* (2), 667-678.
57. Fjermestad, T.; Svelle, S.; Swang, O., Desilication of SAPO-34: reaction mechanisms from periodic DFT calculations. *J. Phys. Chem. C* **2015,** *119* (4), 2073-2085.
58. Pelmenschikov, A.; Leszczynski, J.; Pettersson, L. G., Mechanism of dissolution of neutral silica surfaces: Including effect of self-healing. *J. Phys. Chem. A* **2001,** *105* (41), 9528-9532.
59. Malola, S.; Svelle, S.; Bleken, F. L.; Swang, O., Detailed reaction paths for zeolite dealumination and desilication from density functional calculations. *Angew. Chem. Int. Ed.* **2012,** *51* (3), 652-655.
60. Silaghi, M.-C.; Chizallet, C.; Petracovschi, E.; Kerber, T.; Sauer, J.; Raybaud, P., Regioselectivity of Al–O bond hydrolysis during zeolites dealumination unified by brønsted–evans–polanyi relationship. *ACS Catal.* **2015,** *5* (1), 11-15.
61. Stanciakova, K.; Ensing, B.; Goltl, F.; Bulo, R. E.; Weckhuysen, B. M., Cooperative role of water molecules during the initial stage of water-induced zeolite dealumination. *ACS Catal.* **2019,** *9* (6), 5119-5135.
62. Nielsen, M.; Hafreager, A.; Brogaard, R. Y.; De Wispelaere, K.; Falsig, H.; Beato, P.; Van Speybroeck, V.; Svelle, S., Collective action of water molecules in zeolite dealumination. *Catal. Sci. Technol.* **2019,** *9* (14), 3721-3725.
63. Pelmenschikov, A.; Strandh, H.; Pettersson, L. G.; Leszczynski, J., Lattice resistance to hydrolysis of Si−O−Si bonds of silicate minerals: ab initio calculations of a single water

attack onto the (001) and (111) β-cristobalite surfaces. *J. Phys. Chem. B* **2000,** *104* (24), 5779-5783.

64. Silaghi, M.-C.; Chizallet, C.; Sauer, J.; Raybaud, P., Dealumination mechanisms of zeolites and extra-framework aluminum confinement. *J. Catal.* **2016,** *339*, 242-255.
65. Tamada, O.; Gibbs, G. V.; Boisen Jr, M. B.; Rimstidt, J. D., Silica dissolution catalyzed by NaOH: reaction kinetics and energy barriers simulated by quantum mechanical strategies. *J. Miner. Petrol. Sci.* **2012,** *107* (2), 87-98.
66. Cypryk, M.; Apeloig, Y., Mechanism of the acid-catalyzed Si-O bond cleavage in siloxanes and siloxanols. a theoretical study. *Organometallics* **2002,** *21* (11), 2165-2175.
67. Flyagina, I. S.; Malkin, A. I.; Dolin, S. P., Quantum-chemical simulation of the adsorption-induced reduction of strength of siloxane bonds. *J. Mol. Model.* **2019,** *25* (6), 1-8.
68. Hühn, C.; Erlebach, A.; Mey, D.; Wondraczek, L.; Sierka, M., Ab Initio energetics of Si-O bond cleavage. *J. Comput. Chem.* **2017,** *38* (27), 2349-2353.
69. Kubicki, J. D.; Xiao, Y.; Lasaga, A. C., Theoretical reaction pathways for the formation of [Si(OH)5]1− and the deprotonation of orthosilicic acid in basic solution. *Geochim. Cosmochim. Ac.* **1993,** *57* (16), 3847-3853.
70. Xiao, Y.; Lasaga, A. C., Ab initio quantum mechanical studies of the kinetics and mechanisms of silicate dissolution: H+(H3O+) catalysis. *Geochim. Cosmochim. Ac.* **1994,** *58* (24), 5379-5400.
71. Zhai, D.; Zhao, L.; Liu, Y.; Xu, J.; Shen, B.; Gao, J., Dissolution and absorption: a molecular mechanism of mesopore formation in alkaline treatment of zeolite. *Chem. Mater.* **2015,** *27* (1), 67-74.
72. Rempe, S. B.; Pratt, L. R., The hydration number of Na+ in liquid water. *Fluid Phase Equilibr.* **2001,** *183*, 121-132.
73. Olson, D. H., The crystal structure of dehydrated NaX. *Zeolites* **1995,** *15* (5), 439-443.
74. Takaishi, T., Ordered distribution of Na ions in dehydrated NaX zeolite. *Zeolites* **1996,** *4* (17), 389-392.
75. Nangia, S.; Garrison, B. J., Reaction rates and dissolution mechanisms of quartz as a function of pH. *J. Phys. Chem. A* **2008,** *112* (10), 2027-2033.
76. Holm, M. S.; Svelle, S.; Joensen, F.; Beato, P.; Christensen, C. H.; Bordiga, S.; Bjørgen, M., Assessing the acid properties of desilicated ZSM-5 by FTIR using CO and 2, 4, 6-trimethylpyridine (collidine) as molecular probes. *Appl. Catal. A-Gen.* **2009,** *356* (1), 23-30.

77. Montejo-Valencia, B. D.; Curet-Arana, M. C., DFT study of the Lewis acidities and relative hydrothermal stabilities of BEC and BEA zeolites substituted with Ti, Sn, and Ge. *J. Phys. Chem. C* **2015,** *119* (8), 4148-4157.
78. Bukowski, B. C.; Bates, J. S.; Gounder, R.; Greeley, J., First principles, microkinetic, and experimental analysis of Lewis acid site speciation during ethanol dehydration on Sn-Beta zeolites. *J. Catal.* **2018,** *365*, 261-276.
79. Josephson, T. R.; Jenness, G. R.; Vlachos, D. G.; Caratzoulas, S., Distribution of open sites in Sn-beta zeolite. *Micropor. Mesopor. Mat.* **2017,** *245*, 45-50.
80. To, J.; Sokol, A. A.; French, S. A.; Catlow, C. R. A., Formation of active sites in TS-1 by hydrolysis and inversion. *J. Phys. Chem. C* **2007,** *111* (40), 14720-14731.
81. Kamakoti, P.; Barckholtz, T. A., Role of germanium in the formation of double four rings in zeolites. *J. Phys. Chem. C* **2007,** *111* (9), 3575-3583.
82. Odoh, S. O.; Deem, M. W.; Gagliardi, L., Preferential location of germanium in the UTL and IPC-2a zeolites. *J. Phys. Chem. C* **2014,** *118* (46), 26939-26946.
83. Sastre, G.; Gale, J. D., Derivation of an interatomic potential for germanium-and silicon-containing zeolites and its application to the study of the structures of octadecasil, ASU-7, and ASU-9 materials. *Chem. Mater.* **2003,** *15* (9), 1788-1796.
84. Koch, W.; Holthausen, M. C., *A Chemist's Guide to Density Functional Theory: Part A*. John Wiley & Sons: 2015.
85. Jensen, F., *Introduction to Computational Chemistry:Third edition, Chapter 6*. John wiley & sons: 2017.
86. Hohenberg, P.; Kohn, W., Inhomogeneous electron gas. *Phys. Rev.* **1964,** *136* (3B), B864.
87. Woods, N., On the nature of self-consistency in density functional theory. *arXiv preprint arXiv:1803.01763* **2018**.
88. Fonseca Guerra, C.; Snijders, J. G.; Te Velde, G. t.; Baerends, E. J., Towards an order-N DFT method. *Theor. Chem. Acc.* **1998,** *99* (6), 391-403.
89. Kohn, W.; Sham, L. J., Self-consistent equations including exchange and correlation effects. *Phys. Rev.* **1965,** *140* (4A), A1133.
90. Perdew, J. P., Density-functional approximation for the correlation energy of the in homogeneous electron gas. *Phys. Rev. B* **1986,** *33* (12), 8822.
91. Zhao, G.; Bagayoko, D.; Williams, T., Local-density-approximation prediction of electronic properties of GaN, Si, C, and RuO2. *Phys. Rev. B* **1999,** *60* (3), 1563.
92.Perdew, J. P.; Burke, K.; Ernzerhof, M., Generalized gradient approximation made simple. *Phys. Rev. Lett.* **1996,** *77* (18), 3865.

93. Becke, A. D., Density-functional exchange-energy approximation with correct asymptotic behavior. *Phys. Rev. A* **1988,** *38* (6), 3098.
94. Perdew, J. P.; Chevary, J. A.; Vosko, S. H.; Jackson, K. A.; Pederson, M. R.; Singh, D. J.; Fiolhais, C., Atoms, molecules, solids, and surfaces: applications of the generalized gradient approximation for exchange and correlation. *Phys. Rev. B* **1993,** *48* (7), 4978.
95. Meijer, E. J.; Sprik, M., A density-functional study of the intermolecular interactions of benzene. *J. Chem. Phys.* **1996,** *105* (19), 8684-8689.
96. Cybulski, S. M.; Seversen, C. E., Critical examination of the supermolecule density functional theory calculations of intermolecular interactions. *J. Chem. Phys.* **2005,** *122* (1), 014117.
97. Grimme, S., Density functional theory with london dispersion corrections. *WIRES Comput. Mol. Sci.* **2011,** *1* (2), 211-228.
98. Hermann, J.; DiStasio Jr, R. A.; Tkatchenko, A., First-principles models for van der waals interactions in molecules and materials: concepts, theory, and applications. *Chem. Rev.* **2017,** *117* (6), 4714-4758.
99. Grimme, S.; Hansen, A.; Brandenburg, J. G.; Bannwarth, C., Dispersion-corrected mean-field electronic structure methods. *Chem. Rev.* **2016,** *116* (9), 5105-5154.
100. Grimme, S.; Antony, J.; Ehrlich, S.; Krieg, H., A consistent and accurate ab initio parametrization of density functional dispersion correction (DFT-D) for the 94 elements H-Pu. *J. Chem. Phys.* **2010,** *132* (15), 154104.
101. Grimme, S.; Ehrlich, S.; Goerigk, L., Effect of the damping function in dispersion corrected density functional theory. *J. Comput. Chem.* **2011,** *32* (7), 1456-1465.
102. Grajciar, L.; Heard, C. J.; Bondarenko, A. A.; Polynski, M. V.; Meeprasert, J.; Pidko, E. A.; Nachtigall, P., Towards operando computational modeling in heterogeneous catalysis. *Chem. Soc. Rev.* **2018,** *47* (22), 8307-8348.
103. Mills, G.; Jónsson, H., Quantum and thermal effects in H2 dissociative adsorption: evaluation of free energy barriers in multidimensional quantum systems. *Phys. Rev. lett.* **1994,** *72* (7), 1124.
104. Jónsson, H.; Mills, G.; Jacobsen, K. W., Nudged Elastic Band Method for Finding Minimum Energy Paths of Transitions: pp 385-404. *World Scientific* **1998**.
105. Henkelman, G.; Jónsson, H., Improved tangent estimate in the nudged elastic band method for finding minimum energy paths and saddle points. *J. Chem. Phys.* **2000,** *113* (22), 9978-9985.

106. Henkelman, G.; Uberuaga, B. P.; Jónsson, H., A climbing image nudged elastic band method for finding saddle points and minimum energy paths. *J. Chem. Phys.* **2000,** *113* (22), 9901-9904.
107. Cramer, C. J., *Essentials of Computational Chemistry: Theories and Models*. John Wiley & Sons: 2013.
108. Bucko, T., Ab initio calculations of free-energy reaction barriers. *J. Phys.: Condens. Matter* **2008,** *20* (6), 064211.
109. Glielmo, A.; Husic, B. E.; Rodriguez, A.; Clementi, C.; Noé, F.; Laio, A., Unsupervised learning methods for molecular simulation data. *Chem. Rev.* **2021,** *121* (16), 9722-9758.
110. Šípka, M.; Erlebach, A.; Grajciar, L., Understanding chemical reactions via variational autoencoder and atomic representations. *arXiv preprint arXiv:2203.08097* **2022**.
111. Kresse, G.; Furthmüller, J., Efficiency of ab-initio total energy calculations for metals and semiconductors using a plane-wave basis set. *Comp. Mater. Sci.* **1996,** *6* (1), 15-50.
112. Kresse, G.; Furthmüller, J., Efficient iterative schemes for ab initio total-energy calculations using a plane-wave basis set. *Phys. Rev. B* **1996,** *54* (16), 11169.
113. Kresse, G.; Hafner, J., Ab initio molecular dynamics for liquid metals. *Phys. Rev. B* **1993,** *47* (1), 558.
114. Kresse, G.; Hafner, J., Ab initio molecular-dynamics simulation of the liquid-metal-amorphous-semiconductor transition in germanium. *Phys. Rev B* **1994,** *49* (20), 14251.
115. Fischer, M.; Delgado, M. R.; Areán, C. O.; Duran, C. O., CO adsorption complexes in zeolites: How does the inclusion of dispersion interactions affect predictions made from DFT calculations? the case of Na-CHA. *Theor. Chem. Acc.* **2015,** *134* (7), 1-18.
116. Chiu, C.-c.; Vayssilov, G. N.; Genest, A.; Borgna, A.; Roesch, N., Predicting adsorption enthalpies on silicalite and HZSM-5: a benchmark study on DFT strategies addressing dispersion interactions. *J. Comput. Chem.* **2014,** *35* (10), 809-819.
117. Maintz, S.; Deringer, V. L.; Tchougréeff, A. L.; Dronskowski, R., LOBSTER: a tool to extract chemical bonding from plane-wave based DFT. *J. Comput. Chem.* **2016,** *37*, 1030-1035.
118. Braga, C.; Travis, K. P., A configurational temperature Nosé-Hoover thermostat. *J. Chem. Phys.* **2005,** *123* (13), 134101.
119. Pronk, S.; Páll, S.; Schulz, R.; Larsson, P.; Bjelkmar, P.; Apostolov, R.; Shirts, M. R.; Smith, J. C.; Kasson, P. M.; Van Der Spoel, D., GROMACS 4.5: a high-throughput and highly parallel open source molecular simulation toolkit. *Bioinformatics* **2013,** *29* (7), 845-854.

120. Private communication with Prof. J. van Bokhoven. **2021**.
121. Jin, M.; Veselý, O.; Heard, C.; Kubů, M.; Nachtigal, P.; Čejka, J.; Grajciar, L., The role of water loading and germanium content in germanosilicate hydrolysis. *J. Phys. Chem. C* **2021,** *125* (43), 23744-23757.
122. Yang, G.; Zhou, L., Active sites of M(IV)-incorporated zeolites (M=Sn,Ti,Ge,Zr). *Sci. Rep.* **2017,** *7* (1), 1-14.
123. Cypryk, M.; Apeloig, Y., Mechanism of the acid-catalyzed Si− O bond cleavage in siloxanes and siloxanols. A theoretical study. *Organometallics* **2002,** *21* (11), 2165-2175.
124. Smith, J. D.; Cappa, C. D.; Wilson, K. R.; Messer, B. M.; Cohen, R. C.; Saykally, R. J., Energetics of hydrogen bond network rearrangements in liquid water. *Science* **2004,** *306* (5697), 851-853.
125. Kuo, I.-F. W.; Mundy, C. J., An ab initio molecular dynamics study of the aqueous liquid-vapor interface. *Science* **2004,** *303* (5658), 658-660.
126. Krossner, M.; Sauer, J., Interaction of water with Brønsted acidic sites of zeolite catalysts. ab initio study of 1:1 and 2:1 surface complexes. *J. Phys. Chem.* **1996,** *100* (15), 6199-6211.
127. O'keeffe, M.; Yaghi, O., Germanate zeolites: contrasting the behavior of germanate and silicate structures built from cubic T8O20 units (T= Ge or Si). *Chem. Eur. J.* **1999,** *5* (10), 2796-2801.
128. Sastre, G.; Corma, A., Predicting structural feasibility of silica and germania zeolites. *J. Phys. Chem. C* **2010,** *114* (3), 1667-1673.
129. Caullet, P.; Paillaud, J.-L.; Simon-Masseron, A.; Soulard, M.; Patarin, J., The fluoride route: a strategy to crystalline porous materials. *CR. Chim.* **2005,** *8* (3-4), 245-266.
130. Villaescusa, L. A.; Lightfoot, P.; Morris, R. E., Synthesis and structure of fluoride-containing GeO2 analogues of zeolite double four-ring building units. *Chem. Commun.* **2002,** (19), 2220-2221.
131. Wragg, D. S.; Morris, R. E., Anionic gallium phosphate double four-ring units containing occluded oxygen. *J. Am. Chem. Soc.* **2000,** *122* (45), 11246-11247.
132. Morris, R. E.; Čejka, J., Exploiting chemically selective weakness in solids as a route to new porous materials. *Nat. Chem.* **2015,** *7* (5), 381-388.
133. Jin, M.; Liu, M.; Nachtigall, P.; Grajciar, L.; Heard, C. J., Mechanism of zeolite hydrolysis under basic conditions. *Chem. Mater.* **2021,** *33* (23), 9202-9212.

134. Sokol, A.; Catlow, C.; Garcés, J.; Kuperman, A., Transformation of hydroxyl nests in microporous aluminosilicates upon annealing. *J. Phys.: Condens. Matter* **2004,** *16* (27), S2781.
135. Wang, C.; Leng, S.; Guo, H.; Cao, L.; Huang, J., Acid and alkali treatments for regulation of hydrophilicity/hydrophobicity of natural zeolite. *Appl. Surf. Sci.* **2019,** *478*, 319-326.
136. Hellström, M.; Behler, J. r., Concentration-dependent proton transfer mechanisms in aqueous NaOH solutions: from acceptor-driven to donor-driven and back. *J. Phys. Chem. Lett.* **2016,** *7* (17), 3302-3306.
137. Abraham, A.; Hong, S. B.; Prins, R.; vanBokhoven, J. A., *Studies in Surface Science and Catalysis, Vol. 158, pp. 679-686. (Eds.: J. Čejka, N. Žilková, P. Nachtigall)*. Elsevier 2005.
138. Tatlier, M.; Munz, G.; Henninger, S. K., Relation of water adsorption capacities of zeolites with their structural properties. *Micropor. Mesopor. Mat.* **2018,** *264*, 70-75.
139. Heard, C. J.; Grajciar, L.; Nachtigall, P., The effect of water on the validity of Löwenstein's rule. *Chem. Sci.* **2019,** *10* (22), 5705-5711.
140. Olson, D.; Haag, W.; Lago, R., Chemical and physical properties of the ZSM-5 substitutional series. *J. Catal.* **1980,** *61* (2), 390-396.
141. Chen, N., Hydrophobic properties of zeolites. *J. Phys. Chem.* **1976,** *80* (1), 60-64.
142. Sano, T.; Kasuno, T.; Takeda, K.; Arazaki, S.; Kawakami, Y., Sorption of water vapor on HZSM-5 type zeolites. In *Studies in Surface Science and Catalysis*, Elsevier: 1997; Vol. 105, pp 1771-1778.
143. Jentys, A.; Warecka, G.; Derewinski, M.; Lercher, J. A., Adsorption of water on ZSM5 zeolites. *J. Phys. Chem.* **1989,** *93* (12), 4837-4843.
144. Olson, D.; Haag, W.; Borghard, W., Use of water as a probe of zeolitic properties: interaction of water with HZSM-5. *Micropor. Mesopor. Mat.* **2000,** *35*, 435-446.
145. Jiang, J.; Jorda, J. L.; Diaz-Cabanas, M. J.; Yu, J.; Corma, A., The synthesis of an extra-large-pore zeolite with double three-ring building units and a low framework density. *Angew. Chem.* **2010,** *122* (29), 5106-5108.
146. Corma, A.; Navarro, M. T.; Rey, F.; Rius, J.; Valencia, S., Pure polymorph C of zeolite beta synthesized by using framework isomorphous substitution as a structure-directing mechanism. *Angew. Chem. Int. Ed.* **2001,** *113* (12), 2337-2340.

147. Bellat, J.-P.; Paulin, C.; Jeffroy, M.; Boutin, A.; Paillaud, J.-L.; Patarin, J.; Di Lella, A.; Fuchs, A., Unusual hysteresis loop in the adsorption-desorption of water in NaY zeolite at very low pressure. *J. Phys. Chem. C* **2009,** *113* (19), 8287-8295.
148. Beauvais, C.; Boutin, A.; Fuchs, A. H., Adsorption of water in zeolite sodium-faujasite: a molecular simulation study. *CR. Chim.* **2005,** *8* (3-4), 485-490.

List of Publications

This dissertation was based on following publications:

Attachment 1:

Mengting Jin, Ondřej Veselý, Christopher James Heard, Martin Kubů, Petr Nachtigall, Jiří Čejka* and Lukáš Grajciar*, The role of water loading and germanium content in germanosilicate hydrolysis, *J. Phys. Chem. C,* 2021,125, 43, 23744–23757. (IF=4.126)

To download this article, please use: https://doi.org/10.1021/acs.jpcc.1c06873

Attachment 2:

Mengting Jin, Mingxiu Liu, Petr Nachtigall, Lukáš Grajciar, and Christopher James Heard*, Mechanism of zeolite hydrolysis under basic conditions, *Chem. Mater.*, 2021, 33, 9202–9212. (IF=9.811)

To download this article, please use: https://doi.org/10.1021/acs.chemmater.1c02799

Further publications:

Mengting Jin, Yuheng Guo, Baihai Li, Xiaobin Niu, Yanning Zhang*, Magnetic and electronic properties of a-U_2N_3 and its role in preventing uranium from oxidation: First-principles studies, *J. Nucl. Mater.*, 512, 2018, 72-78. (IF=2.936)

To download this article, please use: https://doi.org/10.1016/j.jnucmat.2018.09.053